EXPLOITATION OF PLASMONIC NANOPARTICLES FOR OPTICAL ENHANCEMENTS IN COMPOSITE MATERIALS

A Dissertation
Presented to
The Academic Faculty

by

Lucas R. Johnstone

In Partial Fulfillment
of the Requirements for the Degree
Doctorate of Philosophy in the
School of Chemistry and Biochemistry

Georgia Institute of Technology
December 2018

EXPLOITATION OF PLASMONIC NANOPARTICLES FOR OPTICAL ENHANCEMENTS IN COMPOSITE MATERIALS

Approved by:

Dr. Joseph W. Perry, Advisor
School of Chemistry and Biochemistry
Georgia Institute of Technology

Dr. Carlos Silva, Co-Advisor
School of Chemistry and Biochemistry
School of Physics
Georgia Institute of Technology

Dr. Seth Marder
School of Chemistry and Biochemistry
Georgia Institute of Technology

Dr. Jean-Luc Bredas
School of Chemistry and Biochemistry
Georgia Institute of Technology

Dr. Thomas Orlando
School of Chemistry and Biochemistry
Georgia Institute of Technology

Dr. Bernard Kippelen
School of Electrical and Computer Engineering
Georgia Institute of Technology

Date Approved: November 07, 2018

ACKNOWLEDGEMENTS

I would like to thank my advisor Prof. Joseph Perry for giving me the opportunity to work in his lab and to take the next step in my scientific career. I would also like to thank my co-advisor Prof. Carlos Silva for his guidance and stepping up when I needed him the most, along with the rest of my thesis committee members, Prof. Seth Marder, Prof. Jean-Luc Bredas, Prof. Thomas Orlando, and Prof. Bernard Kippelen, for their helpful support and critiques of my research experience at Georgia Tech.

I was lucky to have an excellent network of mentors to guide me through my time at Georgia Tech, for which I am eternally grateful. I would like to give a special acknowledgement to Dr. Mohanalingam Kathaperumal. I would not have completed this program without your support, guidance, and friendship. Thank you to Dr. Vincent Chen, Dr. San-Hui Chi, and Dr. Joel Hales, for your leadership and technical expertise throughout our time together. I would be remiss if I did not thank Dr. Carrie Shepler for helping me grow as a teacher, communicator, and person. A special thanks goes out to Dr. John Tillotson, and Dr. Taylor Allen, for being great teammates, grinding it out and having each other's backs. I would also like to thanks Perry group members past and present Yohan Park, Dr. Hyeongu "Anselmo" Kim, Dr. Younsang Kim, Dr. Ariel Marshall, for your support and guidance along the way.

Most importantly the ladies of my life. I would like to thank my mom for her support and encouragement throughout my life. You have continued to be a role model of hard work and have always inspired me to be the best person I can be. Jess, you're simply the best, thank you for putting up with me throughout this process. I love you both.

TABLE OF CONTENTS

LIST OF TABLES

LIST OF FIGURES

LIST OF SYMBOLS AND ABBREVIATIONS

Ag	Silver
Au	Gold
NP	Nanoparticle
DCB	Dichlorobenzene
AgNP	Silver nanoparticle
$AgSiO_2$ NP	Silica coated nanoparticle
J_{SC}	Short circuit current
V_{OC}	Open circuit voltage
FF	Fill factor
PCE	Power conversion efficiency
PSCs	Polymer solar cells
OPV	Organics photovoltaics`
EtOH	Ethanol
λ	Wavelength
χ	Size parameter
ε	Dielectric constant
DMA	Dimethylamine
TEM	Transmission electron microscopy
SEM	Scanning electron microscopy
TEOS	Tetraethylorthosilicate
RW	Rageweed pollen
LSPR	Localized surface plasmon resonance

d	Diameter
$\Delta\lambda$	Change in wavelength
E_o	Incident field strength
SERS	Surface enhanced Raman scattering
FRET	Forster resonate energy transfer
ITO	Indium tin oxide
PEIE	Polyethylenimine ethoxalated
DSSC	Dye sensitized solar cell
PIA	Photo-induced absorption
TAS	Transient absorption spectroscopy
BDT	Benzenedithiol
E_o	Incident Field Strength
I_{sers}	Intensity of SERS signal
P_{sers}	Laser power for SERS measurement
N_{surf}	Number of molecules SERS substrate surface
I_{rs}	Intensity of Raman signal
P_{rs}	Laser power for Raman measurement
N_{vol}	Number of molecules in Raman sample volume
A_m	Surface area of nanostructure
μ_s	Surface density of molecules on nanostructure surface
μ_m	Number of nanostructure in sampling area

SUMMARY

This dissertation explores the optical properties of plasmonic metal nanoparticles and their application in composite materials. Plasmonic metal nanoparticles can be used to concentrate and manipulate light. Due to the oscillations in the conduction electrons these particles exhibit extremely intense electric fields near their surface. Chapter 2 presents a novel method for the nanoscale coating of individual spherical silver nanoparticles with a thin layer of silica shell. The silica shell is used to mitigate the well-known negative quenching effects that occur at the surface of metal nanoparticles, and can be readily functionalized.

Chapter 3 the metal nanoparticles are utilized to build a multifunctional SERS substrate with a unique geometry. A simple solution processed layer-by-layer approach was used to immobilize metal nanoparticles (NP) on the surface of ragweed pollen exine. Nanoparticle agglomeration on the pollen gives rise to broadband (400-1064 nm) plasmonic activity, and strong SERS signals from benzenedithiol deposited on NP-pollen composite particles were observed. In addition to SERS activity, the Ag NP coating provides a two-fold increase of the adhesive properties of the RW pollen exine on a silicon substrate. The result is a robust, adhesive, broadband SERS micro-particle sensor, which also exhibit two-photon excited fluorescence.

Chapters 4 & 5 document the investigation of plasmonic nanoparticle doping in P3HT:PCBM photovoltaic devices. Current voltage characteristics were measured to determine the effect of plasmonic nanoparticle doping on the power conversion efficiency. Differential scanning calorimetry was used to investigate the effects of nanoparticle doping

on the microstructure of the OPV devices. Various functional silanes were used to modify the surface of silica coated silver nanoparticles to determine whether surface functionalization impacts the device morphology.

CHAPTER 1. INTRODUCTION

1.1 Nanomaterials and Plasmonics

1.1.1 Introduction to Metal Nanoparticles

People have found application for metal nanoparticles for over 1600 years. For example, the red or green walls of the Lycurgus Cup (Figure 1.1) are the result of gold and silver nanoparticle doped glass.[1] It is doubtful the Romans knew metal nanoparticles were the source of the color, it is possible they knew the cup contained gold and silver in some form. This glass staining method using gold, coined "Purple of Cassius," was reported by Cassius in 1685, it has been documented as far back as 1600.[2] However, it wasn't until 1857, that Michael Faraday postulated this red color was due to the presence of metal nanoparticles.[3] In 1908 Gustav Mie was the first to theoretically explain the nanoparticle phenomena with a full solution to Maxwell's equations for a spherical particle, which is still used today.[4] In 1951 Turkevich et al. present experimental studies on the growth and nucleation of gold colloids, known as the Turkevich method, and nanoparticle research as we know it had begun.[5] Nanoparticle research has exploded over the past two decades and metal nanoparticles have found applications in biomedical,[6-13] catalysis,[14-17] and molecular detection.[18-20] These research efforts have resulted in metal nanoparticles incorporated in consumer products such as antimicrobial bandages and clothing, lateral flow assays (home pregnancy tests) and cosmetics.[21-23]

Figure 1.1 The Lycurgus Cup, a Roman chalice circa 400 AD. Dichroic glass appears green when reflecting light (left). Appears red when light transmits though the glass (right). Adapted with permission from ref [1]. (Copyright 2000 Springer Nature)

1.1.2 Optical Properties on Metal Nanoparticles

Bulk gold and silver display bulk metallic behavior, such as high electrical and thermal conductivity and high reflectivity, shrinking the size class of metal particles to dimensions below the wavelength of light creates a whole host of new and interesting physical properties due to quantum confinement. The reddish color of the Lycurgus Cup and "Purple of Cassius" originate from the absorption by the metal nanoparticles (NP) and the corresponding localized surface plasmon resonance (LSPR). A purely classical view of plasmon resonances can be obtained by considering the situation where the dimensions of the particle are sufficiently small, in which case the incident electric field from the electromagnetic wave appears uniform over the size of the particle, and exerts a uniform force on the conduction band free electron cloud, shown in Figure 1.2A. At a particular material dependent frequency, a resonance occurs resulting in strong oscillations of the surface electrons, known as LSPR. Quantum confinement in two dimensions, such as in a

wire, results in a scenario in which the surface plasmons can propagate across the structure, as shown in Figure 1.2B. The oscillations associated with the LSPR give rise to extremely high field intensities near the particle surface (Figure 1.2, right). These field enhancements are the heart of plasmonics research and will be discussed throughout this work. In addition to colloidal metal nanoparticles, a wide variety of complex lithographic techniques have been developed to generate and tailor plasmonic nanostructures.[24-27] These techniques along with PSP structures are outside the scope of this work, and herein we will focus on colloidal metal nanoparticles.

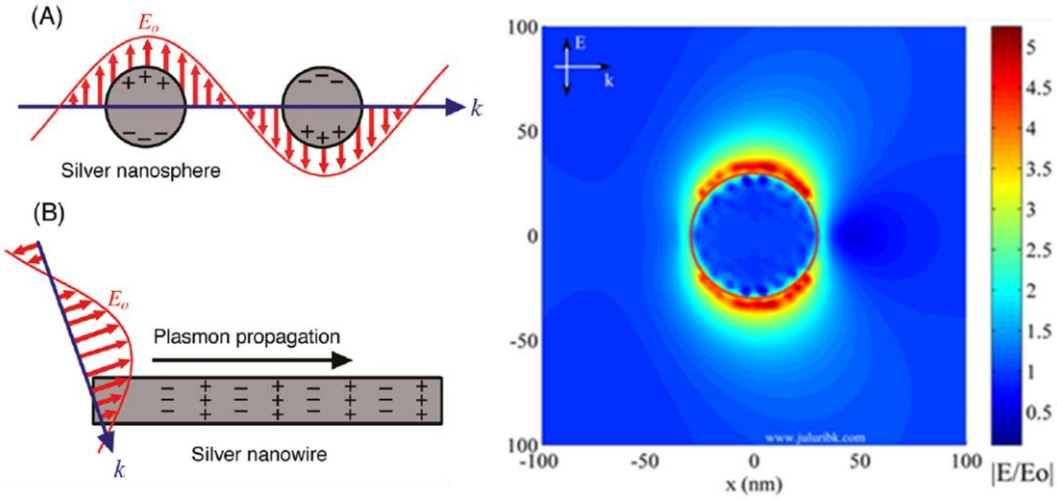

Figure 1.2 Schematic representation of A.) Localized Surface Plasmon Resonance (LSPR) of a spherical nanoparticle. B) Propagating Surface Plasmon (PSP) along the long axis of silver nanowire (left). Simulation of the field enhancement around a 60nm gold sphere (right). Adapted with permission from ref [29]. Copyright 2010 American Chemical Society.

1.1.2.1 Materials Selection

Silver and gold are by far the most prevalent in the literature, copper[28-29] and aluminum[30-31] have exhibited plasmonic properties. Excitation wavelength and application needs must be considered when choosing an appropriate nanomaterial. Mie theory is the

simplest approximation to predict the material cross section (absorption + scattering) of a spherical nanoparticle: [32]

$$C_{ext} = \frac{24\pi^2 R^3 \varepsilon_m^{\frac{3}{2}}}{\lambda}\left[\frac{\varepsilon_i}{(\varepsilon_r + 2\varepsilon_m)^2 + {\varepsilon_i}^2}\right] \quad (1)$$

where C_{ext} is the extinction cross section, R is the particle radius, ε_m is the dielectric constant of the surrounding medium, ε_r and ε_i are the real and imaginary portions of the material's dielectric function at optical frequencies. Thus, to maximize the cross section at a given wavelength the ε_r needs to be as close to -2ε_m, with ε_i near zero, these conditions can only be satisfied by a few metals.[33] Another factor to consider is the strength of the plasmon resonance, which is referred to as the *Q* factor, which is also inversely proportional to ε_i. A factor of $Q \approx 10$ is considered to be necessary for plasmonic application. A low *Q* value will result in a weak plasmon that will decay quickly. *Q* values for common metals are plotted in Figure 1.3. It is clear that silver is the material of choice in terms of plasmonic strength and broadband coverage. One drawback to silver nanomaterials is the release of silver ions, known to be toxic,[34-35] which is why the biologically benign gold is used for biomedical applications.[6-7] Only single materials particles have been discussed here, but it's worth noting that a wide variety of bi-metallic and alloy nanoparticles have been realized as a method for tuning nanoparticle properties.[36-40] One such technique uses silver nano-cubes subject to galvanic replacement with gold, creating alloy nano-cubes with various compositions, whose spectra can be tuned well into the NIR, shown in Figure 1.4.

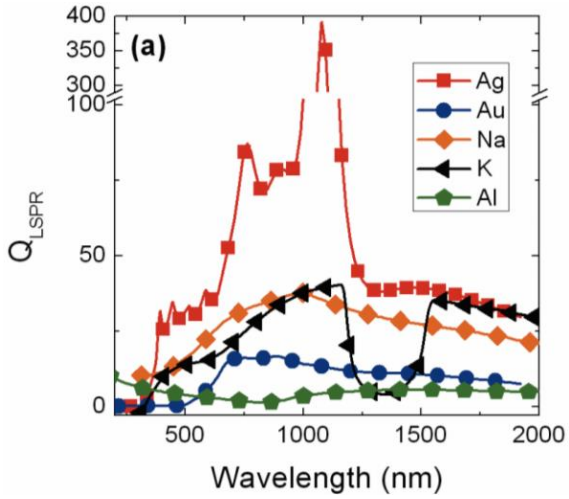

Figure 1.3 Wavelength dependence of the LSPR *Q* -factor for various metals. Adapted with permission from ref [34]. (Copyright © 2010, John Wiley and Sons)

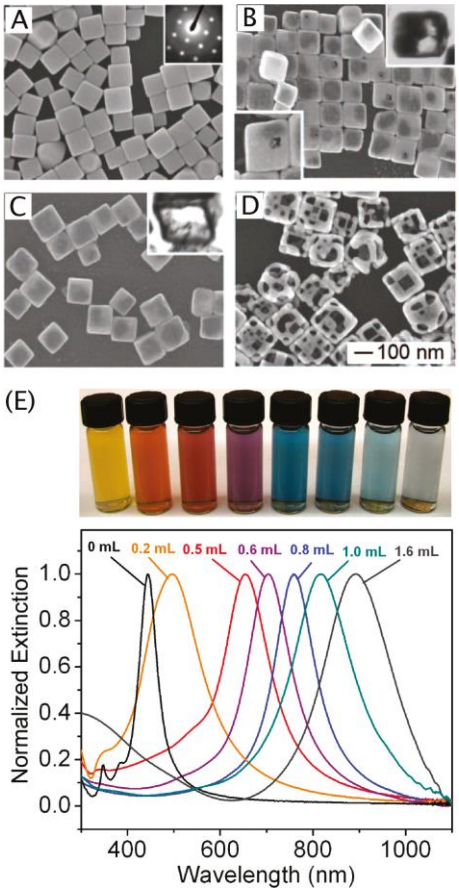

Figure 1.4 (A) SEM image of the sacrificial templates, Ag nanocubes, and (B−D) SEM images of the Ag−Au nanoboxes and nanocages obtained from sequential stages of a galvanic replacement reaction. Insets of (B) and (C) are microtomed TEM samples

showing the hollow interior, and the inset of (A) is an electron diffraction pattern. The 100 nm scale bar applies to all SEM images. (E, top panel) Vials containing Au nanoboxes and nanocages prepared by reacting 5 mL of a 0.2 nM Ag nanocube (edge length ≈ 40 nm) suspension with different volumes of a 0.1 mM HAuCl4 solution. (E, lower panel). Corresponding UV−VIS spectra of Ag nanocubes and Au−Ag nanoboxes/nanocages. Reproduced with permission from ref [40] (Copyright 2011 American Chemical Society).

1.1.2.2 Size Effects in Metal Nanoparticles

The extinction cross-section is a sum of the absorption and scattering cross-sections (Figure 1.5). The absorption and scattering cross sections follow a 3rd and 6th power law respectively, with respect to particle size. This dependence leads to absorption as the dominant mechanism at small sizes and scatter dominates at larger diameters as seen in Figure 1.5.[41] Extrinsic size effects are caused by the plasmon interaction with multipolar modes in larger particles and are dominate when the size parameter $\chi \approx 1$(Eq. 2);

$$\chi = \frac{\pi d}{\lambda} \tag{2}$$

where, d is the particle diameter, and λ is the wavelength of light in vacuum. Extrinsic effects result in a broadening and redshift in the plasmon resonance, and size alone can be used to tune the LSPR by more than 60 nm. When $\chi << 1$, the nanoparticle is governed by intrinsic size effects. When the mean free path of the conduction electrons is similar or larger than the particle size, the free electron relaxation rates cause a dampening of the LSPR.[42] These intrinsic size effects cause a reduction in the intensity of the LSPR when the particle size increases beyond a threshold size.

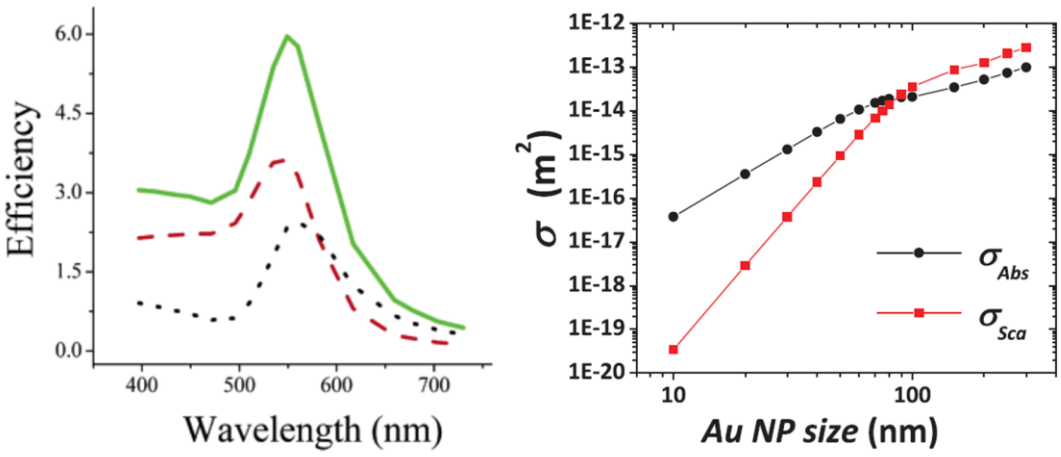

Figure 1.5 Calculated extinction (green), absorption (red), scattering (black) spectra of an 80 nm gold sphere (left). Comparison of absorption and scattering cross-section as a function of nanoparticle diameter (right). Adapted with permission from ref [39] (Copyright © 2006 American Chemical Society).

1.1.2.3 Shape Effects

In late 1990's, wet-chemical seeded growth techniques were developed to create gold nano-rods, which demonstrated NIR plasmon resonances.[43] In the decades following advances in synthesis and characterization have led to number of new shapes such as cubes, stars, wires, ellipses, triangles, and prisms just to name a few. Each unique geometry lends to a unique plasmonic absorption as seen in the summary in Figure 1.6.

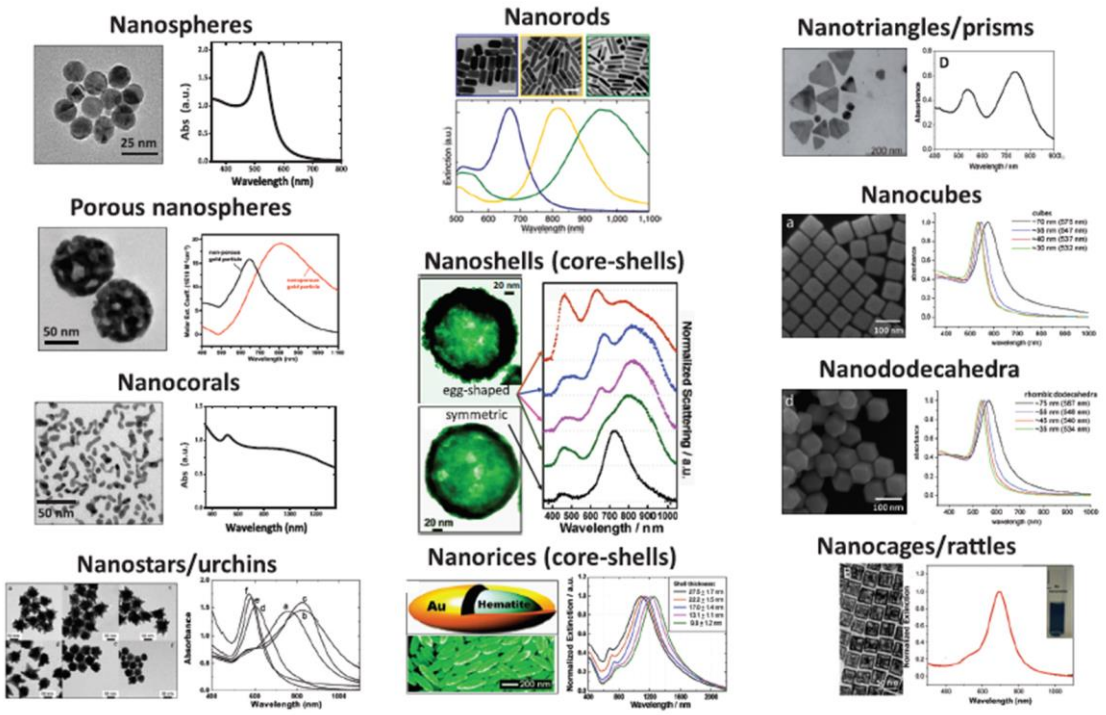

Figure 1.6 Au NP with different shapes and corresponding optical extinction (transmission) or scattering (dark-field) spectra. Adapted with permission from ref [42] (Copyright IOP Science).

Controlling the shape of the metal nanoparticle determines the width, position, and number of plasmon resonances. Another factor to consider is the strength and distribution of the enhanced field. In a sphere, the field enhancement is radial and fairly uniform, whereas, in cubes or triangles the field has been shown to concentrate near the edges or points of the structure, giving rise to greater field enhancements.[44-45] These development demonstrate the importance NP shape can play in the field of plasmonics.

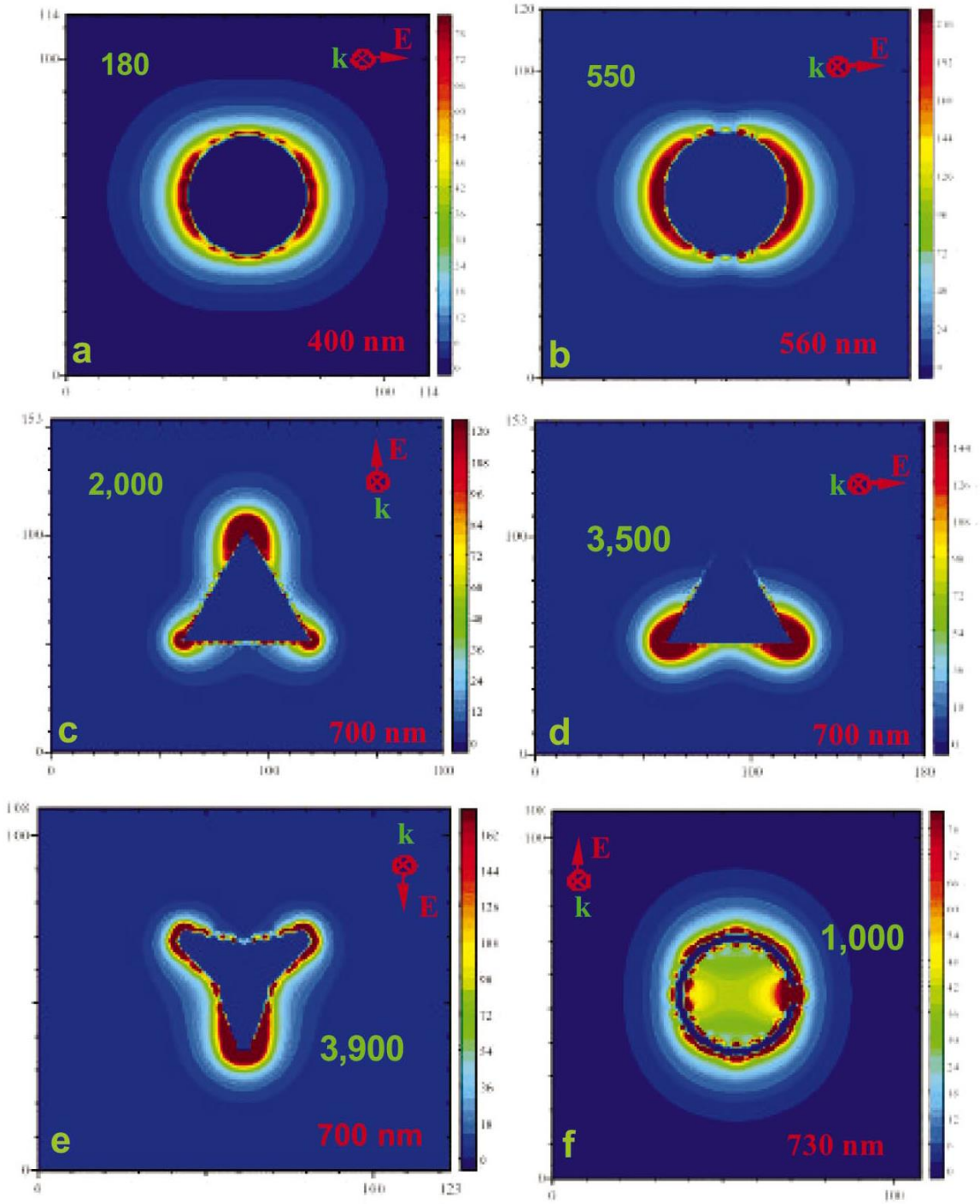

Figure 1.7 E-field enhancement contours of a) Ag sphere (r = 19nm), b) Ag nanodisk (d = 40nm thickness = 9 nm), c,d) Triangular prism, (edge 60 nm, thickness 12 nm) e) three-tipped Au nanocrystal (tip-tip = 48 nm thickness 14 nm), f) Au nanoshell (r = 18 nm, shell thickness = 3 nm). Peak enhancement is shown in green at given wavelength in red). Adapted with permission from ref [45]. (Copyright © 2004 Springer Science + Business Media).

1.1.2.4 Nanoparticle Coupling Interactions

Significant advancements in sensing capabilities have been achieved utilizing closely spaced metal nanoparticles. The first demonstration of single molecule detection was achieved using clusters of aggregated silver nanoparticles.[46] It has been widely demonstrated that coupling between two nanoparticles leads to a redshift in the extinction resonance.[47-48] This shift in the LSPR can be approximated with the "Plasmon Ruler Equation" (Eq. 3),

$$\frac{\Delta\lambda}{\lambda_o} = Ae^{\left(\frac{-\frac{s}{D}}{\tau}\right)} \tag{3}$$

where, $\Delta\lambda$ is the change in wavelength due to aggregation effects, λ_o is the single particle wavelength, s is the separation between particles, and *D* is the diameter of the particle. The pre-exponential, A, and the decay constant, τ, are related to coupling strength and decay length.[49] More advantageous than the shift in the plasmon resonance, this coupling also leads to extremely high field enhancements between interacting particles.[50] Figure 1.8 show the simulated E-field between two nanoprisms arranged tip-to-tip, the peak enhancement between the tips is 5300 x E_o, compared to the 3500 x E_o, at the tip of an individual particle. These coupling phenomena have been used to design nanostructures that show broadband resonances, due to a high degree of particles coupling, such as the nanocoral shown in Figure 1.6.[51-52] These high field areas between particles have transformed the molecular sensing field, which colloquially refers to them as "hotspots". The design of new SERS platforms often focuses on the creation and manipulation of these hotspots to improve detection capabilities.[53-55]

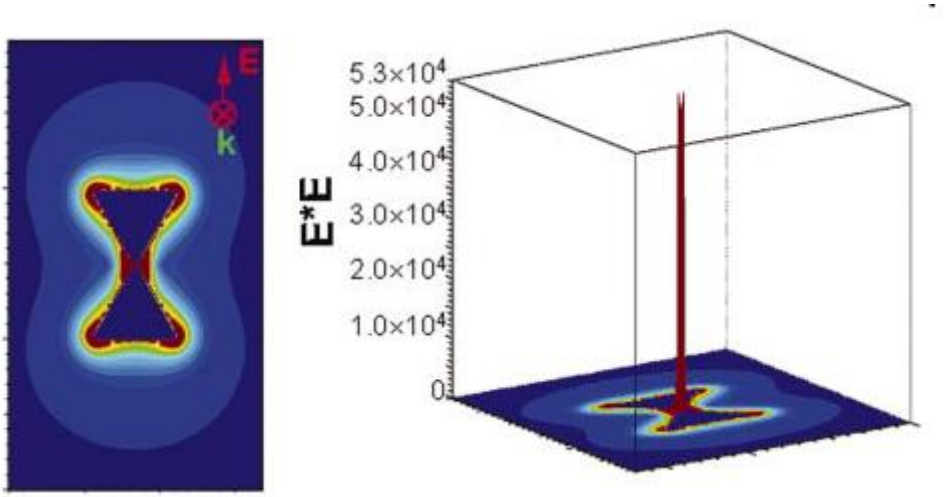

Figure 1.8 E-Field enhancement contour of a tip-to-tip prism dimer, showing a peak enhancement of 5.3 x 10^4 x E_0 between the tips, when excited at 932 nm. Adapter with permission from ref [50]. (Copyright AIP Publishing).

1.1.2.5 Silica Coated Noble Metal Core-Shell Nanoparticles

Noble metal nanoparticles supporting LSPR have found numerous applications in nearly all scientific disciplines. Well-defined nanostructures such as spheres, rods, stars, triangles, and others have been engineered, and can readily be synthesized. Practical application of these materials often requires harsh conditions which may induce aggregation, cause etching or distort their structure. One of the most common methods to overcome these challenges is to passivate the surface with a sturdy inert shell such as silica.

The most common route to coating with a silica shell is a modified version of the Stober method.[56] These methods rely on base catalyzed hydrolysis and condensation of tetraethylorthosilicate (TEOS) in the presence of the metal nanoparticle.[57-58] These methods offer control of shell thickness and monodispersed metal cores, but they often require surface priming, 16+ hour reaction times, and silica overgrowth. Another technique commonly used is a reverse micro-emulsion procedure, where TEOS is suspended in the

oil portion, while the metal core in the aqueous phase in the presence of a surfactant.[59] This method can effectively be done sequentially in a one pot synthesis and is also effective with other metals such as platinum and iron oxide.[60-61] Other advanced techniques such as ultrasound,[62] flame aerosol,[63] and microwave assisted,[64] have been developed.

Figure 1.9 shows a variety of practical applications of silica coated metal nanoparticles in which the silica shell plays numerous different roles.[65] Colloidal stabilization is often seen as the primary role. Changes in pH, ionic strength, chemical environment and temperature can cause irreversible aggregation, etching, or shape distortions which can compromise the plasmonic properties of the nanostructure. Silica sols are remarkable stable compared to the noble metal counterparts. The highly negative surface charge of the hydroxyl rich surface leads to electrostatic repulsion, and at short separation distances the low Hamaker constant of silica results in low van der Waals attractions.[66]

It is well known that metal nanoparticles can quench the fluorescence of excited chromophores through Forster resonant energy transfer (FRET).[67] FRET occurs when the fluorophore is within a few nanometers of the particle surface, within the Foerster radius- the radius in which the FRET rate competes with all other deactivation rates. With careful control of the separation distance between metal surface and chromophore, large plasmonic enhancement of the fluorescence have be realized (Figure 1.9d).[68] With proper separation and manipulation of plasmonic hotspots enhancement factors of 10^6 for one photon excitation,[69] and 10^5 for 2-photon excitation have been achieved.[70] Silica coated metal nanoparticles have been extensively utilized to control the separation distance in metal enhanced fluorescence applications. Additionally, fluorescent or Raman-active dyes can

be encapsulated within the shell to maintain optimal separation distance and protect from external elements. Although not discussed in detail here, it is worth noting that mesoporous silica shells have been used to template growth of nanoparticles with interesting geometries, and have proven valuable in theranostics and drug delivery.

The development of a novel method for silica coated silver nanoparticles is presented in this thesis. The plasmonic properties of these particles are then exploited in composite sensing and photovoltaic materials. The silica shell will passivate the NP surface, facilitate phase transfer, prevent FRET quenching, and provide electrical insulation to mitigate charge carrier quenching.

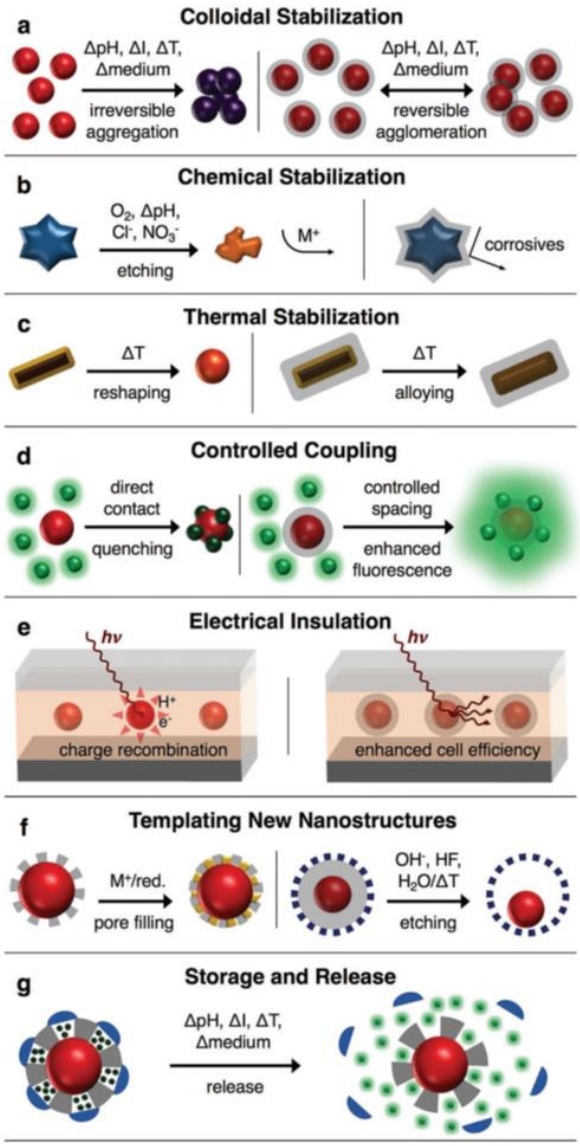

Figure 1.9 Schematic representation depicting various functions of the silica shell in composite systems containing core-shell NP structures. Adapted with permission from ref [65]. (Copyright © 2018, John Wiley and Sons).

1.2 Plasmon Sensing

The demand for highly sensitive, and ideally cost effective detection devices for biological markers, drug or explosive residues, and hazardous chemicals has led to significant research in sensor development. Some applications require a simple yes or no

sensing response (e.g. pregnancy tests), others require quantitative determination. Metal nanoparticles have become a staple in sensor technologies due to the sensitivity of their LSPR frequency to changes in dielectric environment, shape, or particle coupling. Lin et al. developed a LSPR sensor for glucose detection,[71] where glucose etches the gold nanorods leading to a shift in the LSRP frequency. The glucose concentration can be determined from the shift in LSPR.

Calorimetric sensing assays are based on the color change when nanoparticle solution transforms from individual particles to an aggregated state due to the presence of the analyte.[72] The high extinction cross section of noble metal nanoparticles in the visible regime make them ideal candidates for colorimetric assays, and can often be visualized with the naked eye. These assays are simple, sensitive, selective, and portable method for the detection of target analyte, as shown in Figure 1.10. DNA functionalized nanoparticles area aggregated in the presences of the complementary target where the color of the solution turns from red to blue (Figure 1.10a). With careful selection of the nanoparticle ligand system, calorimetric sensors can be designed for ion, molecular, or drug analysis (Figure 1.10 b-d). These methods demonstrate the creativity of nano-engineering, often they are analyte specific and are not applicable for high throughput or analyte independent sensing.

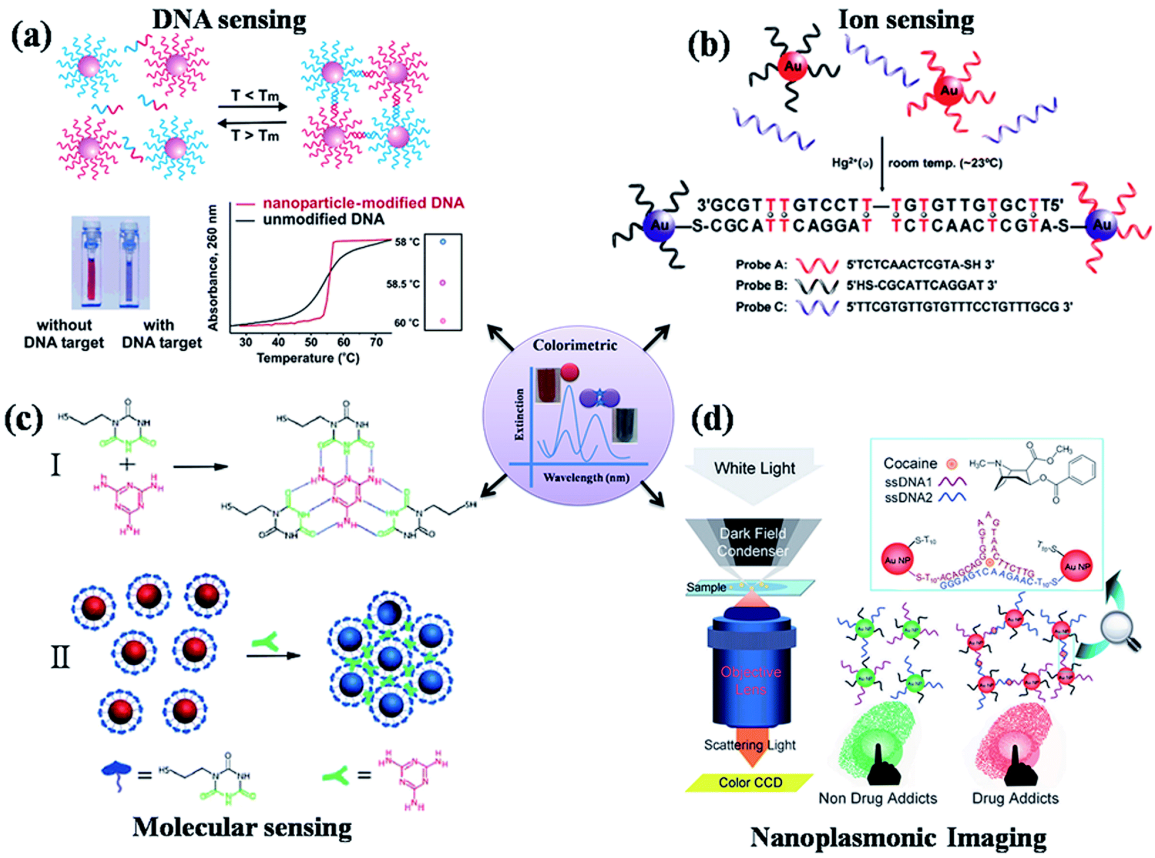

Figure 1.10 Colorimetric sensing: (a) schematic representation of a strategy for colorimetric DNA detection using DNA conjugated Au NPs. The addition of a complementary target to DNA oligonucleotide-functionalized gold nanoparticles leads to aggregation, resulting in a change of solution color from red to blue. (b) Colorimetric sensing of Hg^{2+} using T-DNA conjugated Au NPs through T–Hg^{2+}–T complexation. (c) Visual detection of melamine using MTT-stabilized gold nanoparticles. (d) Here, cocaine acts as a molecular linker to aggregate the DNA conjugated Au NPs probes. Adapted with permission from ref [72] (copyright the Royal Society of Chemistry 2014).

1.2.1 Surface Enhanced Raman Scattering (SERS)

SERS sensors are the most prevalent type of molecular sensors, often designed to be high throughput and analyte indiscriminate. Raman scattering is the inelastic counterpart to Rayleigh scattering, as shown in Figure 1.11. When photons interact with a molecule or particle they either scatter elastically known as Rayleigh scattering, or in-elastically known

as Raman scattering. Light interacts with a molecule and forms an unstable virtual state, and is coherently reemitted. During Rayleigh scattering an electron is excited to the virtual state and decays back to the original state, where the emitted photon has the same energy of the incident light. During the Raman scattering process the election either goes from the ground state back to a vibrational state, or from a vibrational state back to the ground state. These processes result in an emitted photon at a different energy from the incident light. The Stokes process is defined as the lower energy transition, and Anti-Stokes is the higher energy transition, as shown in Figure 1.11. At room temperature a larger portion of the molecules are in the ground state, thus the Stokes shift is often monitored in Raman spectroscopy. Raman spectroscopy is a very precise technique for molecular identification through their unique vibrational fingerprint. Unfortunately, only one in 10^6-10^8 photons undergo Raman scattering rendering their detection difficult if not impossible. Typical Raman cross-sections are on the order of 10^{-27} cm^2/sr, they also scale with the fourth power of the incident electric field.[73] With plasmonic field enhancements on the order of 10^4, Raman scattering enhancements of up to 10^{16} compared to traditional Raman signals have been realized. These type of SERS sensors have demonstrated the ability to detect down to the single molecule level.[46, 74-75]

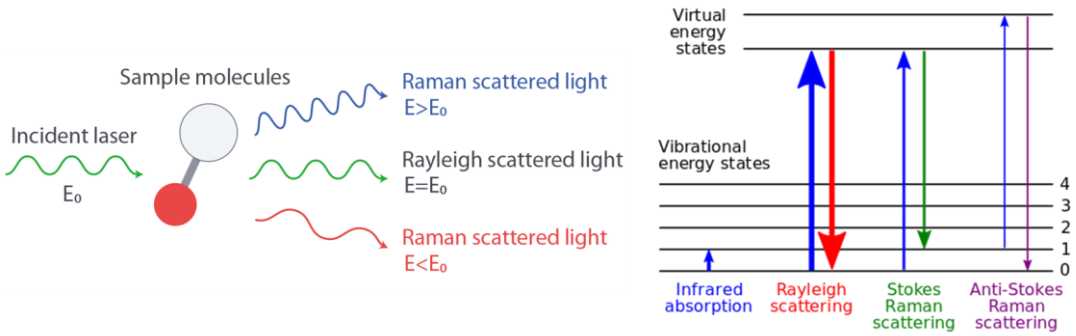

Figure 1.11 Schematic representation of light scattering processes and corresponding energy level diagram.

SERS was introduced in the mid 70's,[76] where it was utilized by a small community of electrochemists and spectroscopists. The discovery of single-molecule detection capabilities in the late 90's,[46] along with the rapid development of nanofabrication, have led to the incorporation of SERS technology to nearly every corner of chemistry, physics, and material and life sciences. SERS has been widely studied, yet the exact mechanism of enhancement is still not fully elucidated. There are generally two accepted mechanism which contribute to enhancement, the electromagnetic mechanism and the chemical enhancement (CE) mechanism.[73] The electromagnetic (EM) mechanism results from the interaction of molecules in close proximity to the metal surface and the LSPR of the nanostructure. The EM component is accepted as the dominant enhancement mode in SERS spectroscopy. The CE mechanism relates to the electronic properties of the analyte absorbed on the metal surface and its interaction with the induced dipole of the plasmon resonance. Charge transfer between the electronic ground state and the metal can change the polarizability of the molecule, resulting in a change in the Raman scattering cross-section. Additionally, the energy levels of the analyte may be different in the bound and free states, which may induce electronic absorption to states that were previously

inaccessible, to the excitation frequency.[73] These chemical enhancement effects are typically one to three orders of magnitude, while the deconvolution from the EM effects are often difficult or not possible.

SERS has become such a widely used technique that an attempt to review its applications or the development of SERS substrates is a fruitless effort. As such, the following section will explore the application of micro-particle SERS substrates, which are relevant to the work contained in this thesis.

1.2.2 Micro-particle SERS Sensors

Nanoparticle based SERS sensors have found numerous applications in solution based chemical sensing with sensitivities reaching the single molecule level.[46] One challenge in solution based SERS sensing applications is the inherently small size of plasmonic NP, where even aggregated clusters of nanoparticles are too small to be viewed by traditional optical microscopic techniques. This can make it difficult to determine the NP morphology, or the analyte and NP concentrations in the sampling volume. In order to overcome these challenges, substrate based nanoparticle assemblies have been extensively studied for their application as SERS sensors. These assemblies can be tailored to create a high density of Raman hotspots necessary for sensitive detection. These methods are less amenable to solution based applications. Additionally, it is advantageous to build three dimensional sensors to increase the surface area to volume ratio. One method to address these challenges is the design of 3D micro-particle structures. Benefit of this sensor geometry include: compatibility with in-solution or on-substrate applications; a high surface area to volume ratio; and the ability to effectively transfer plasmonic nanoparticle

properties into the micro-meter size domain, which typically cannot support plasmon resonances. Meanwhile, the properties of the underlying particle support can impart additional functionality. Yamaguchi *et al.* reported a high-sensitivity SERS sensor based on gold-decorated polystyrene micro-particles. Here detection is enabled by dielectrophoresis, which is used to manipulate the polystyrene core through laser path.[77] Stetciura *et al.*,[78] demonstrated the SERS activity of silver nanoparticle coated calcium carbonate micro-particles. The carbonate particles were doped with astralen, before the in situ deposition of AgNP, where the astralen is used as an internal Raman marker for particle tracking. The Raman signals of externally applied polymers were also detected with SERS spectroscopy.

The development of a novel micro-particle SERS sensor platform is presented in this thesis. Ragweed pollen particles are coated with pre-synthesized Ag and $AgSiO_2$ NPs to create a 3D micro-particle sensor. The underlying pollen particle is naturally adhesive, 2-photon fluorescent, and has a very high surface area to volume ratio. The NP surface coating create a high degree of Raman hotspots giving rise to strong SERS signals from externally applied marker molecules.

1.3 Photovoltaics

The worlds primary energy consumption is expected to increase by 28% by 2040 and major greenhouse gas production are predicted to increase by 33% from 2015 to 2100.[79] By the turn of the century, the average global surface temperature is expected to be 2.6 – 3.5ºC higher than pre-industrial (1860-1880) levels.[79] As a result, ocean levels are rising and becoming more acidic. The entire world agrees climate change and fossil fuel

consumption is a major concern, leading to the Paris Agreement, an attempt to mitigate greenhouse gas emissions. The demand for renewable energy sources has never been greater. Solar power was the only technology to witness an investment increase in 2017, with new investments up 18% relative to 2016.[80] The work presented here is focused on organic photovoltaics a few comments of other relevant technologies is presented below.

1.3.1 Commercialized Photovoltaics (1st and 2nd Generation)

The first instance of turning light into electrical energy was reported by Becquerel, while using an electrolytic cell with metal electrodes in an electrolyte solution.[81] In 1954 a silicon p-n junction device with an efficiency of 6% was discovered by Chaplin *et al.*[82] Since this initial discover, a variety of solar cell technologies have been discovered utilizing various charge generating materials. Figure 1.12 show the record performance for various photovoltaic as a function of time. Advancements in silicon processing and efficiency increases have led to significant commercialization. The total global capacity has increased from 8 GW to 402 GW over the last decade.[80] Silicon still accounts for 95% of the PV market.

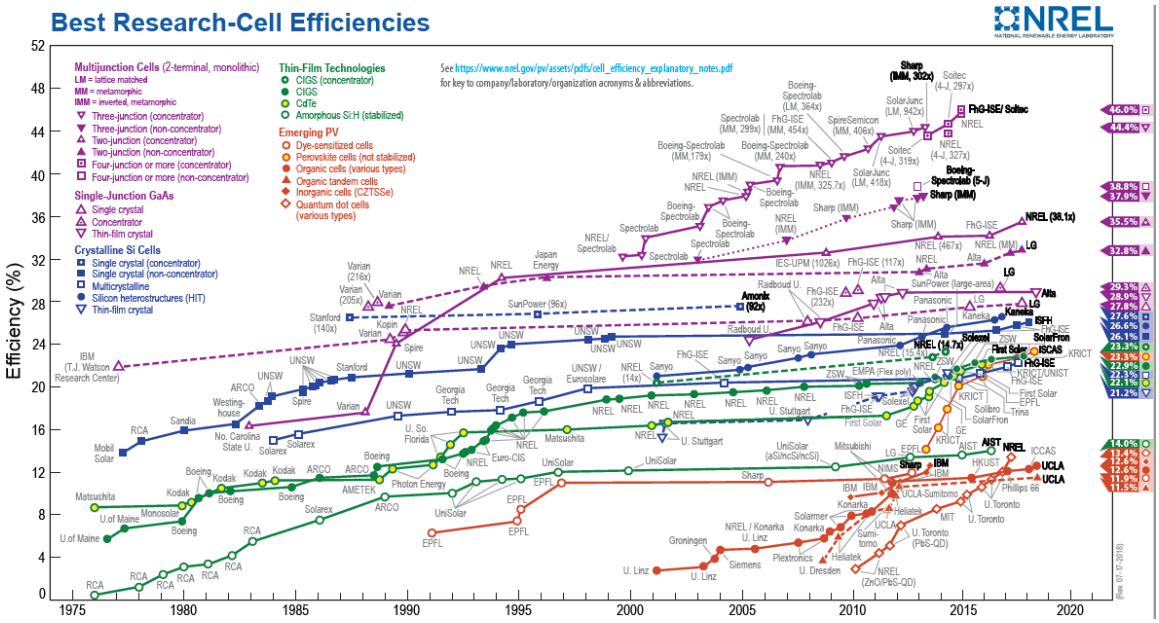

Figure 1.12 Highest recorded power conversion efficiencies of various PV technologies (NREL 07-17-2018).[83]

1.3.1.1 Silicon Solar Cells

Silicon solar cells currently dominate the market. These devices are cut from large single crystal which are energy inefficient to grow hard to process and do not absorb light efficiently since silicon is an indirect bandgap semiconductor. Multi-crystalline silicon is grown from a similar molten silicon state without the care to grow a single crystal, resulting in an increased defect content which decreases their efficiency but also the cost. Recently efficiencies of single crystal and multi crystalline silicon solar cells have reached 26.1%, and 22.3%, respectively. The cost of the silicon is 50% of the whole module,[84] which is why researchers have been looking to replace it since its inception.

1.3.1.2 Thin-Film Photovoltaics

These 2nd generation thin film devices are from lower grade amorphous or nano-crystalline silicon, or other semiconductor material. They have higher absorption and thus can be made thinner, processed at lower temperature and require less material. These advancements lead to lower production costs, these device make up the remainder of the commercially produced devices. The viability of these device due to rare toxic materials is a concern. Record efficiencies of 23.3% for CIGS (copper-indium-gallium-selenide) semiconductor devices, and 14.0% for amorphous silicon devices have been demonstrated.[85]

1.3.2 3rd Generation Photovoltaics

These technologies are still mainly in the research and development stage. These device are constructed of organic semiconductors (OPV) or organic/inorganic hybrid materials (DSSCs, Perovskites). These devices are of particular interest due to low cost, versatile low temperature processing, and tunable optical and electronic properties.

1.3.2.1 Dye Sensitized Solar Cells (DSSCs)

Dye-sensitized solar cells (DSSCs) were discovered in 1991 by Gratzel and O'Regan.[86] Since this discovery there has been a considerable amount of research devoted to this area due to their low cost, simple fabrication and relatively high conversion efficiencies. To date the highest recorded efficiencies have exceeded 11.9%, which is approaching other thin film technologies such as amorphous silicon.[85] The device consists of a glass substrate coated with a transparent conductive oxide (TCO), often fluorine tin oxide (FTO). This substrate is then coated with a dense layer of TiO_2, followed by a porous TiO_2 layer constructed of interconnected nanoparticles. This working electrode is coated

with a dye sensitizer through chemisorption from a dye solution. The electrode is typically separated from the platinum coated FTO counter electrode by a I^-/I_3^- electrolyte. The physical contact of these components is important and energy-level matching of the various components is required to ensure unidirectional electron flow. Absorption of incident light by the dye sensitizer molecules starts the operation, followed by fast injection of excited electrons into the conduction band of the TiO_2. These electrons diffuse through the TiO_2 network to the TCO electrode and through the external circuit to provide a current. These electrons travel through the counter electrode where transfer to the redox electrolyte is followed by catalysis by the platinum coating on the electrode[87]. The electrolyte transports these electrons back to the oxidized dye molecules and the process repeats. One of the main challenges of commercializing DSSCs is their long term stability. The redox electrolyte is contained in a volatile organic solvent, which leads to leakage, evaporation, platinum degradation, as well as dye degradation.[88]

1.3.2.2 Perovskite Solar Cells

Perovskite solar cells spun out of DSSC research when Kojima *et al.* attempted to use perovskites as a sensitizer.[89] The perovskite layer has been shown to act as both a sensitizer and effective electron and hole transport material.[90] In less than a decade efficiencies rose from 3.8% to a record of 23.3%.[85]

1.3.2.3 Organic Solar Cells

Organic photovoltaics (OPVs) and polymer solar cells (PSCs) will often be used interchangeably during this work. An OPV device contains electron-donating and electron-accepting materials sandwiched between the anode and cathode. Upon the absorption of

photons a molecular exciton, is generated (Figure 1.13a). Excitons then diffuse to the donor-acceptor (D-A) interface (Figure 1.13b). The exciton then enters a charge transfer state still bound to the hole, the electron is on the acceptor and the hole is on the donor (Figure 1.13c). Finally, the charge separated state where free carriers are generated (Figure 1.13d).

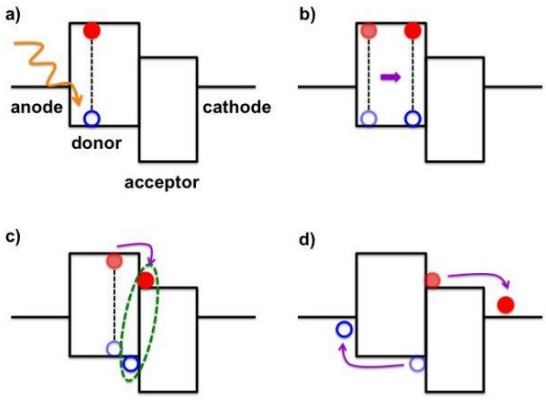

Figure 1.13 Schematic representation of processes in an OPV device, a) exciton formation, b) exciton diffusion, c) bound charge transfer state, where electron on acceptor and hole on donor, d) charge separated state

Tang first demonstrated this with a bilayer device base on copper pthalocyanine donor and a perylene derivative as the electron acceptor achieving a device efficiency of 1%.[91] The low exciton diffusion lengths in organic molecules limits the potential of bilayer devices. These diffusion lengths are on the order of 10 nm, thus any exciton further away from the interface are essentially wasted. In the early 90's, Yu *et al.* developed the bulk heterojunction (Figure 1.14), where an intercalated network of donor and acceptor with domain sizes on the order of exciton diffusion lengths were formed.[92-95] The efficiency of these devices was not impressive, but they demonstrated diode rectification behavior. This result set off decades of research on the optimization of the bulk heterojunction structure

and the synthesis of semiconducting polymers. OPVs have achieved efficiencies of 13.5% for single junction,[96] and 17.3% for tandem geometry,[97] which is still low compared to other device geometries. Although, OPVs are low cost and provide processing advantages such as roll-to-roll capabilities, inkjet and flexible substrate applications.

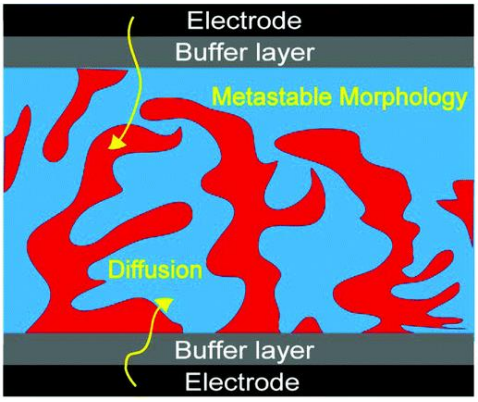

Figure 1.14 A bulk heterojunction, deigned to minimize the distance between the donor acceptor interface and photo-generated excitons. Adapted with permission from ref [93]. (Copyright 2016 Royal Society of Chemistry).

1.4 Plasmonic Organic Photovoltaics

The intense field enhancements near the surface of noble metal nanoparticles have been used to enhance the performance of OPV devices. Initial attempts to incorporate various metal nanoparticles into the active layer of the device were of mixed results, where several groups reported photo-current enhancements,[98-100] while multiple groups reported no plasmonic enhancement and often deterioration of device performance.[101-103] The next evolution of plasmonic OPVs research was isolating the nanoparticles in the charge transport layers. It is worth noting that a huge increase in the number of reports of this method, compared to directly incorporating into the active layer, which lends the question if some portion of these reports did not have success with NP in the active layer and moved

on to this approach. Again several reports have emerged attributing increased current to plasmonic induced optical enhancements, often relying on current increase, fluorescence data, and internal quantum efficiency measurements.[104-106] Several other groups witnessed very similar enhancements but systematically demonstrated these effects to be due to electrical effects such as extraction efficiency,[107-108] and charge accumulation effects.[109] It is clear that these plasmonic nanoparticles can improve performance of photovoltaic devices, but increases in current cannot directly be contributed to optical plasmonic enhancements without evidence, and rigorous characterization is needed to understand these interactions. Individually coating the nanoparticle and doping them in the active layer represents the third generation of these devices. Here, the metal quenching variations from the 1st generation as well as the increased electrical collection efficiency of the 2nd generation should be minimized. These 3rd generation devices seem to be much more in agreement about their plasmonic optical enhancements.[110-112]

In this work transient absorption spectroscopy is utilized to investigate the interaction between these core-shell nanoparticles and the exciton and charge-carrier populations in devices consisting of polymer donors and fullerene acceptors. The instantaneous exciton population can be compared to the reference devices to determine directly if indeed plasmonic absorption effects are behind the improved performance, or other effects such as changes in microstructure upon nanoparticle blending are also relevant. Additionally, the morphology of these devices are notoriously fickle, and the nanoparticle effects on microstructure have been criminally ignored. By systematically varying the surface composition of the NP dopant the microstructural changes are investigated and correlated to the resultant electrical and photo-physics experiments.

1.5 OPV Characterization

1.5.1 J-V Characterization

To normalize J-V measurements taken in different parts of the world, the standard solar spectrum (Figure 1.15b) is determined at AM 1.5 G (Figure 1.15a). The photo-generated current and voltage produced from a solar cell under illumination, and the corresponding power-voltage relationship are plotted in Figure 1.15c. The negative power curve is indicative of power generation. The work herein focuses on the four main device parameters: open circuit voltage (V_{OC}), short-circuit current density (J_{SC}), fill factor (*FF*), and power conversion efficiency (*PCE*). These parameters will be monitored to determine what impact plasmonic NP doping has on device performance.

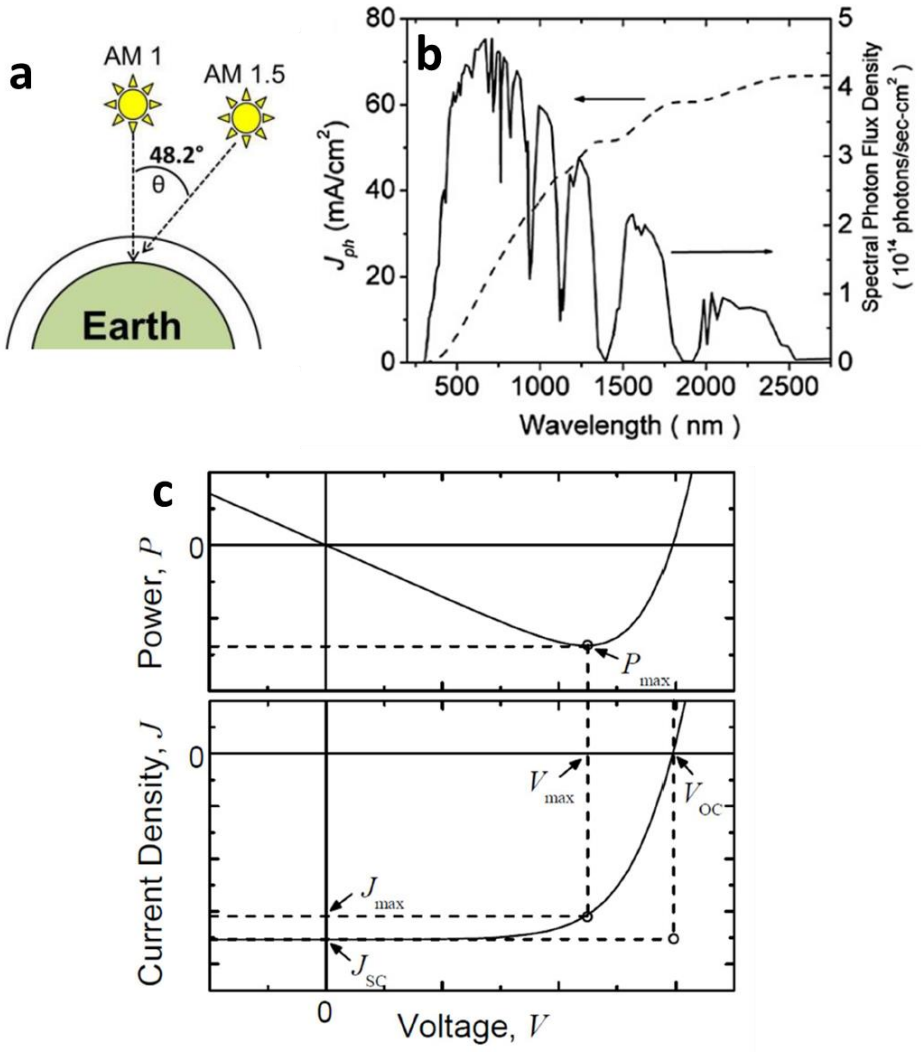

Figure 1.15 a) the schematic representation of AM 1.5G b) the spectral irradiance of the AM 1.5 G solar spectrum. c) J-V and P-V of an OPV device under illumination of 1 sun 100 mW/cm2. Adapted with permission from ref [109]. (Copyright 2009 RCS publishing).

1.5.1.1 Open Circuit Voltage (V_{OC})

V_{OC} is defined is the voltage across the solar cell under open circuit condition, where no current is flowing through the cell. It is extracted from the point where the J-V curve crosses the x-axis. The difference in the donor ionization potential and the acceptors electron affinity is the theoretical upper limit of V_{OC}.[113]

1.5.1.2 Short-circuit Current Density (J_{SC})

J_{SC} is the maximum current density drawn from the cell when short-circuited for a given illumination, typically 100 mw/cm^2 with an AM 1.5G spectrum. The value is extracted from the point where the J-V curve crosses the y-axis

1.5.1.3 Fill Factor (*FF*)

The *FF* is the ratio of the maximum power, P_{MAX}, to the product of J_{SC} and V_{OC}. A large *FF* is desirable, but it will be reduced by recombination losses and parasitic resistances.

$$FF = \frac{P_{MAX}}{J_{SC} * V_{OC}} = \frac{J_{MAX} * V_{MAX}}{J_{SC} * V_{OC}} \tag{4}$$

1.5.1.4 Power Conversion Efficiency (*PCE*)

PCE is the ratio of the power generated by the device to the power incident on the device. Where the industry standard is to measure *PCE* values at 1 sun, which equals 100 mw/cm^2, with an AM 1.5 G spectrum.

$$PCE = \frac{P_{MAX}}{P_{INC}} = \frac{V_{OC} * J_{SC} * FF}{P_{INC}} \tag{5}$$

1.5.2 Transient Absorption Spectroscopy (TAS)

TAS is a pump-probe spectroscopic technique where the pump excites the material, and the low power probe monitors the absorption of the excited species. By varying the delay between the pump and the probe using a delay stage the temporal evolution of the

transient absorption spectrum is measured and the decay of the excited species can be extracted. P3HT:PCBM systems have been extensively study with TAS, and the exciton, polaron, and ground state bleach (GSB) absorption frequencies are well known.[114-115]

Differential Transmission spectroscopy measurements were performed using an ultrafast laser system (Pharos Model PH1-20-0200-02-10, Light Conversion) emitting 1030 nm pulses at 100 KHz, with an output power of 20 W and pulse duration of∼220 fs. Experiments were carried out in an integrated transient absorption/time-resolved photoluminescence commercial setup (Light Conversion Hera). Pump wavelengths in the spectral range 360–2600 nm were generated by feeding 10 W from the laser output to a commercial optical parametric amplifier (Orpheus, Light Conversion, Lithuania), while 2 W are focused onto a sapphire crystal to obtain a single-filament white-light continuum covering the spectral range ∼490−1050 nm for the probe beam. When higher energy probe light was required, a blue white-light continuum was similarly obtained by using the second harmonic of the laser output instead. The probe beam transmitted through the sample is detected by an imaging spectrograph (Shamrock 193i, Andor Technology Ltd., UK) in combination with a multichannel detector (256 pixels, 200–1100 nm wavelength sensitivity range). Maximum pump fluences were 2 μJ/cm^2, with atypical spot diameter of 1.9 mm estimated at the 1/e^2 plane).

1.6 REFERENCES

1. Wagner, F. E.; Haslbeck, S.; Stievano, L.; Calogero, S.; Pankhurst, Q. A.; Martinek, K. P., Before striking gold in gold-ruby glass. *Nature* **2000,** *407,* 691.

2. Hunt, L. B., The true story of Purple of Cassius. *Gold Bulletin* **1976,** *9* (4), 134-139.

3. Thompson, D., Michael Faraday's recognition of ruby gold: the birth of modern nanotechnology. *Gold Bulletin* **2007,** *40* (4), 267-269.

4. Mie, G., Beiträge zur Optik trüber Medien, speziell kolloidaler Metallösungen. *Annalen der Physik* **1908,** *330* (3), 377-445.

5. Turkevich, J.; Stevenson, P. C.; Hillier, J., A study of the nucleation and growth processes in the synthesis of colloidal gold. *Discussions of the Faraday Society* **1951,** *11* (0), 55-75.

6. Biswas, A.; Wang, T.; Biris, A. S., Single metal nanoparticle spectroscopy: optical characterization of individual nanosystems for biomedical applications. *Nanoscale* **2010,** *2* (9), 1560-1572.

7. Dykman, L.; Khlebtsov, N., Gold nanoparticles in biomedical applications: recent advances and perspectives. *Chemical Society Reviews* **2012,** *41* (6), 2256-2282.

8. Priyadarshini, S.; Gopinath, V.; Meera Priyadharsshini, N.; MubarakAli, D.; Velusamy, P., Synthesis of anisotropic silver nanoparticles using novel strain, Bacillus flexus and its biomedical application. *Colloids and Surfaces B: Biointerfaces* **2013,** *102*, 232-237.

9. Li, X.; Wei, J.; Aifantis, K. E.; Fan, Y.; Feng, Q.; Cui, F.-Z.; Watari, F., Current investigations into magnetic nanoparticles for biomedical applications. *Journal of Biomedical Materials Research Part A* **2016,** *104* (5), 1285-1296.

10. Conde, J.; Doria, G.; Baptista, P., Noble Metal Nanoparticles Applications in Cancer. *Journal of Drug Delivery* **2012,** *2012*, 12.

11. Bansal, A.; Zhang, Y., Photocontrolled Nanoparticle Delivery Systems for Biomedical Applications. *Accounts of Chemical Research* **2014,** *47* (10), 3052-3060.

12. Arvizo, R. R.; Bhattacharyya, S.; Kudgus, R. A.; Giri, K.; Bhattacharya, R.; Mukherjee, P., Intrinsic therapeutic applications of noble metal nanoparticles: past, present and future. *Chemical Society Reviews* **2012,** *41* (7), 2943-2970.

13. Daraee, H.; Eatemadi, A.; Abbasi, E.; Fekri Aval, S.; Kouhi, M.; Akbarzadeh, A., Application of gold nanoparticles in biomedical and drug delivery. *Artificial Cells, Nanomedicine, and Biotechnology* **2016,** *44* (1), 410-422.

14. Cui, C.-H.; Yu, S.-H., Engineering Interface and Surface of Noble Metal Nanoparticle Nanotubes toward Enhanced Catalytic Activity for Fuel Cell Applications. *Accounts of Chemical Research* **2013,** *46* (7), 1427-1437.

15. Li, G.; Tang, Z., Noble metal nanoparticle@metal oxide core/yolk–shell nanostructures as catalysts: recent progress and perspective. *Nanoscale* **2014,** *6* (8), 3995-4011.

16. Jeong, Y. S.; Park, J.-B.; Jung, H.-G.; Kim, J.; Luo, X.; Lu, J.; Curtiss, L.; Amine, K.; Sun, Y.-K.; Scrosati, B.; Lee, Y. J., Study on the Catalytic Activity of Noble Metal Nanoparticles on Reduced Graphene Oxide for Oxygen Evolution Reactions in Lithium–Air Batteries. *Nano Letters* **2015,** *15* (7), 4261-4268.

17. Navalon, S.; Dhakshinamoorthy, A.; Alvaro, M.; Garcia, H., Metal nanoparticles supported on two-dimensional graphenes as heterogeneous catalysts. *Coordination Chemistry Reviews* **2016,** *312*, 99-148.

18. Priyadarshini, E.; Pradhan, N., Gold nanoparticles as efficient sensors in colorimetric detection of toxic metal ions: A review. *Sensors and Actuators B: Chemical* **2017,** *238*, 888-902.

19. Ding, S.-Y.; Yi, J.; Li, J.-F.; Ren, B.; Wu, D.-Y.; Panneerselvam, R.; Tian, Z.-Q., Nanostructure-based plasmon-enhanced Raman spectroscopy for surface analysis of materials. *Nature Reviews Materials* **2016,** *1*, 16021.

20. Chen, H.-Y.; Lin, M.-H.; Wang, C.-Y.; Chang, Y.-M.; Gwo, S., Large-Scale Hot Spot Engineering for Quantitative SERS at the Single-Molecule Scale. *Journal of the American Chemical Society* **2015,** *137* (42), 13698-13705.

21. Niska, K.; Zielinska, E.; Radomski, M. W.; Inkielewicz-Stepniak, I., Metal nanoparticles in dermatology and cosmetology: Interactions with human skin cells. *Chemico-Biological Interactions* **2017**.

22. Vance, M. E.; Kuiken, T.; Vejerano, E. P.; McGinnis, S. P.; Hochella, M. F., Jr.; Rejeski, D.; Hull, M. S., Nanotechnology in the real world: Redeveloping the nanomaterial consumer products inventory. *Beilstein Journal of Nanotechnology* **2015,** *6*, 1769-1780.

23. Posthuma-Trumpie, G. A.; Korf, J.; van Amerongen, A., Lateral flow (immuno)assay: its strengths, weaknesses, opportunities and threats. A literature survey. *Analytical and Bioanalytical Chemistry* **2009,** *393* (2), 569-582.

24. Shkondin, E.; Takayama, O.; Panah, M. E. A.; Liu, P.; Larsen, P. V.; Mar, M. D.; Jensen, F.; Lavrinenko, A. V. In *Highly ordered transparent conductive oxide nanopillar metamaterials for mid-infrared plasmonics*, 2017 Conference on Lasers and Electro-Optics Europe & European Quantum Electronics Conference (CLEO/Europe-EQEC), 25-29 June 2017; 2017; pp 1-1.

25. Bagheri, S.; Zgrabik, C. M.; Gissibl, T.; Tittl, A.; Sterl, F.; Walter, R.; De Zuani, S.; Berrier, A.; Stauden, T.; Richter, G.; Hu, E. L.; Giessen, H., Large-area fabrication of TiN nanoantenna arrays for refractory plasmonics in the mid-infrared by femtosecond direct laser writing and interference lithography [Invited]. *Opt. Mater. Express* **2015,** *5* (11), 2625-2633.

26. Luo, J.; Zeng, B.; Wang, C.; Gao, P.; Liu, K.; Pu, M.; Jin, J.; Zhao, Z.; Li, X.; Yu, H.; Luo, X., Fabrication of anisotropically arrayed nano-slots metasurfaces using reflective plasmonic lithography. *Nanoscale* **2015,** *7* (44), 18805-18812.

27. Kuchmizhak, A.; Gurbatov, S.; Vitrik, O.; Kulchin, Y.; Milichko, V.; Makarov, S.; Kudryashov, S., Ion-beam assisted laser fabrication of sensing plasmonic nanostructures. *Scientific Reports* **2016,** *6*, 19410.

28. Chan, G. H.; Zhao, J.; Hicks, E. M.; Schatz, G. C.; Van Duyne, R. P., Plasmonic Properties of Copper Nanoparticles Fabricated by Nanosphere Lithography. *Nano Letters* **2007,** *7* (7), 1947-1952.

29. Sun, Q.-C.; Ding, Y.; Goodman, S. M.; H. Funke, H.; Nagpal, P., Copper plasmonics and catalysis: role of electron–phonon interactions in dephasing localized surface plasmons. *Nanoscale* **2014,** *6* (21), 12450-12457.

30. Knight, M. W.; King, N. S.; Liu, L.; Everitt, H. O.; Nordlander, P.; Halas, N. J., Aluminum for Plasmonics. *ACS Nano* **2014,** *8* (1), 834-840.

31. Ekinci, Y.; Solak, H. H.; Löffler, J. F., Plasmon resonances of aluminum nanoparticles and nanorods. *Journal of Applied Physics* **2008,** *104* (8), 083107.

32. Mulvaney, P., Surface Plasmon Spectroscopy of Nanosized Metal Particles. *Langmuir* **1996,** *12* (3), 788-800.

33. Kelly, K. L.; Coronado, E.; Zhao, L. L.; Schatz, G. C., The Optical Properties of Metal Nanoparticles: The Influence of Size, Shape, and Dielectric Environment. *The Journal of Physical Chemistry B* **2003,** *107* (3), 668-677.

34. West, P. R.; Ishii, S.; Naik, G. V.; Emani, N. K.; Shalaev, V. M.; Boltasseva, A., Searching for better plasmonic materials. *Laser & Photonics Reviews* **2010,** *4* (6), 795-808.

35. Choi, Y.; Kim, H.-A.; Kim, K.-W.; Lee, B.-T., Comparative toxicity of silver nanoparticles and silver ions to Escherichia coli. *Journal of Environmental Sciences* **2018,** *66*, 50-60.

36. Kang, Q.; Wang, T.; Li, P.; Liu, L.; Chang, K.; Li, M.; Ye, J., Photocatalytic Reduction of Carbon Dioxide by Hydrous Hydrazine over Au–Cu Alloy Nanoparticles Supported on SrTiO3/TiO2 Coaxial Nanotube Arrays. *Angewandte Chemie* **2014,** *127* (3), 855-859.

37. Tegeder, P.; Freitag, M.; Chepiga, K.; Muratsugu, S.; Möller, N.; Lamping, S.; Tada, M.; Glorius, F.; Ravoo, B. J., N-Heterocyclic Carbene-Modified AuPd Alloy Nanoparticles and their Application as Biomimetic and Heterogeneous Catalysts. *Chemistry – A European Journal* **2018,** *0* (ja).

38. Luo, L.; Duan, Z.; Li, H.; Kim, J.; Henkelman, G.; Crooks, R. M., Tunability of the Adsorbate Binding on Bimetallic Alloy Nanoparticles for the Optimization of Catalytic Hydrogenation. *Journal of the American Chemical Society* **2017,** *139* (15), 5538-5546.

39. Tiedemann, D.; Taylor, U.; Rehbock, C.; Jakobi, J.; Klein, S.; Kues, W. A.; Barcikowski, S.; Rath, D., Reprotoxicity of gold, silver, and gold–silver alloy nanoparticles on mammalian gametes. *Analyst* **2014,** *139* (5), 931-942.

40. Rycenga, M.; Cobley, C. M.; Zeng, J.; Li, W.; Moran, C. H.; Zhang, Q.; Qin, D.; Xia, Y., Controlling the Synthesis and Assembly of Silver Nanostructures for Plasmonic Applications. *Chemical Reviews* **2011,** *111* (6), 3669-3712.

41. Jain, P. K.; Lee, K. S.; El-Sayed, I. H.; El-Sayed, M. A., Calculated Absorption and Scattering Properties of Gold Nanoparticles of Different Size, Shape, and Composition: Applications in Biological Imaging and Biomedicine. *The Journal of Physical Chemistry B* **2006,** *110* (14), 7238-7248.

42. Vincenzo, A.; Roberto, P.; Marco, F.; Onofrio, M. M.; Maria Antonia, I., Surface plasmon resonance in gold nanoparticles: a review. *Journal of Physics: Condensed Matter* **2017,** *29* (20), 203002.

43. C. Hulteen, J.; Martin, C. R., A general template-based method for the preparation of nanomaterials. *Journal of Materials Chemistry* **1997,** *7* (7), 1075-1087.

44. Agrawal, A.; Kriegel, I.; Milliron, D. J., Shape-Dependent Field Enhancement and Plasmon Resonance of Oxide Nanocrystals. *The Journal of Physical Chemistry C* **2015,** *119* (11), 6227-6238.

45. Hao, E.; Schatz, G. C.; Hupp, J. T., Synthesis and Optical Properties of Anisotropic Metal Nanoparticles. *Journal of Fluorescence* **2004,** *14* (4), 331-341.

46. Kneipp, K.; Wang, Y.; Kneipp, H.; Perelman, L. T.; Itzkan, I.; Dasari, R. R.; Feld, M. S., Single Molecule Detection Using Surface-Enhanced Raman Scattering (SERS). *Physical Review Letters* **1997,** *78* (9), 1667-1670.

47. Muskens, O. L.; Giannini, V.; Sánchez-Gil, J. A.; Gómez Rivas, J., Optical scattering resonances of single and coupled dimer plasmonic nanoantennas. *Opt. Express* **2007,** *15* (26), 17736-17746.

48. Funston, A. M.; Novo, C.; Davis, T. J.; Mulvaney, P., Plasmon Coupling of Gold Nanorods at Short Distances and in Different Geometries. *Nano Letters* **2009,** *9* (4), 1651-1658.

49. Tabor, C.; Murali, R.; Mahmoud, M.; El-Sayed, M. A., On the Use of Plasmonic Nanoparticle Pairs As a Plasmon Ruler: The Dependence of the Near-Field Dipole Plasmon Coupling on Nanoparticle Size and Shape. *The Journal of Physical Chemistry A* **2009,** *113* (10), 1946-1953.

50. Hao, E.; Schatz, G. C., Electromagnetic fields around silver nanoparticles and dimers. *The Journal of Chemical Physics* **2003,** *120* (1), 357-366.

51. Teulle, A.; Bosman, M.; Girard, C.; Gurunatha, K. L.; Li, M.; Mann, S.; Dujardin, E., Multimodal plasmonics in fused colloidal networks. *Nature Materials* **2014,** *14*, 87.

52. Poletti, A.; Fracasso, G.; Conti, G.; Pilot, R.; Amendola, V., Laser generated gold nanocorals with broadband plasmon absorption for photothermal applications. *Nanoscale* **2015,** *7* (32), 13702-13714.

53. Yu, M.; Huang, Z.; Liu, Z.; Chen, J.; Liu, Y.; Tang, L.; Liu, G., Annealed gold nanoshells with highly-dense hotspots for large-area efficient Raman scattering substrates. *Sensors and Actuators B: Chemical* **2018,** *262*, 845-851.

54. Li, S.; Li, D.; Zhang, Q.-Y.; Tang, X., Surface enhanced Raman scattering substrate with high-density hotspots fabricated by depositing Ag film on TiO2-catalyzed Ag nanoparticles. *Journal of Alloys and Compounds* **2016,** *689*, 439-445.

55. Wei, X.; Fan, Q.; Liu, H.; Bai, Y.; Zhang, L.; Zheng, H.; Yin, Y.; Gao, C., Holey Au–Ag alloy nanoplates with built-in hotspots for surface-enhanced Raman scattering. *Nanoscale* **2016,** *8* (34), 15689-15695.

56. Stöber, W.; Fink, A.; Bohn, E., Controlled growth of monodisperse silica spheres in the micron size range. *Journal of Colloid and Interface Science* **1968,** *26* (1), 62-69.

57. Kobayashi, Y.; Katakami, H.; Mine, E.; Nagao, D.; Konno, M.; Liz-Marzán, L. M., Silica coating of silver nanoparticles using a modified Stöber method. *Journal of Colloid and Interface Science* **2005,** *283* (2), 392-396.

58. Liz-Marzán, L. M.; Giersig, M.; Mulvaney, P., Homogeneous silica coating of vitreophobic colloids. *Chemical Communications* **1996,** (6), 731-732.

59. Han, Y.; Jiang, J.; Lee, S. S.; Ying, J. Y., Reverse Microemulsion-Mediated Synthesis of Silica-Coated Gold and Silver Nanoparticles. *Langmuir* **2008,** *24* (11), 5842-5848.

60. Kunio, H.; Hideki, M.; Sakae, T.; Masahiro, K., Preparation of silica-coated Pt metal nanoparticles using microemulsion and their catalytic performance. *Science and Technology of Advanced Materials* **2006,** *7* (7), 678.

61. Santra, S.; Tapec, R.; Theodoropoulou, N.; Dobson, J.; Hebard, A.; Tan, W., Synthesis and Characterization of Silica-Coated Iron Oxide Nanoparticles in Microemulsion: The Effect of Nonionic Surfactants. *Langmuir* **2001,** *17* (10), 2900-2906.

62. Montaño-Priede, J. L.; Peña-Rodríguez, O.; Pal, U., Near-Electric-Field Tuned Plasmonic Au@SiO2 and Ag@SiO2 Nanoparticles for Efficient Utilization in Luminescence Enhancement and Surface-Enhanced Spectroscopy. *The Journal of Physical Chemistry C* **2017,** *121* (41), 23062-23071.

63. Sotiriou, G. A.; Sannomiya, T.; Teleki, A.; Krumeich, F.; Vörös, J.; Pratsinis, S. E., Non-Toxic Dry-Coated Nanosilver for Plasmonic Biosensors. *Advanced Functional Materials* **2010,** *20* (24), 4250-4257.

64. Bahadur, N. M.; Furusawa, T.; Sato, M.; Kurayama, F.; Siddiquey, I. A.; Suzuki, N., Fast and facile synthesis of silica coated silver nanoparticles by microwave irradiation. *Journal of Colloid and Interface Science* **2011,** *355* (2), 312-320.

65. Hanske, C.; Sanz-Ortiz, M. N.; Liz-Marzán, L. M., Silica-Coated Plasmonic Metal Nanoparticles in Action. *Advanced Materials* **2018,** *30* (27), 1707003.

66. Guerrero-Martínez, A.; Pérez-Juste, J.; Liz-Marzán, L. M., Recent Progress on Silica Coating of Nanoparticles and Related Nanomaterials. *Advanced Materials* **2010,** *22* (11), 1182-1195.

67. Kang, K. A.; Wang, J.; Jasinski, J. B.; Achilefu, S., Fluorescence Manipulation by Gold Nanoparticles: From Complete Quenching to Extensive Enhancement. *Journal of Nanobiotechnology* **2011,** *9* (1), 16.

68. Li, J.-F.; Li, C.-Y.; Aroca, R. F., Plasmon-enhanced fluorescence spectroscopy. *Chemical Society Reviews* **2017,** *46* (13), 3962-3979.

69. Zhou, L.; Ding, F.; Chen, H.; Ding, W.; Zhang, W.; Chou, S. Y., Enhancement of Immunoassay's Fluorescence and Detection Sensitivity Using Three-Dimensional Plasmonic Nano-Antenna-Dots Array. *Analytical Chemistry* **2012,** *84* (10), 4489-4495.

70. Wenseleers, W.; Stellacci, F.; Meyer-Friedrichsen, T.; Mangel, T.; Bauer, C. A.; Pond, S. J. K.; Marder, S. R.; Perry, J. W., Five Orders-of-Magnitude Enhancement of Two-Photon Absorption for Dyes on Silver Nanoparticle Fractal Clusters. *The Journal of Physical Chemistry B* **2002,** *106* (27), 6853-6863.

71. Lin, Y.; Zhao, M.; Guo, Y.; Ma, X.; Luo, F.; Guo, L.; Qiu, B.; Chen, G.; Lin, Z., Multicolor Colormetric Biosensor for the Determination of Glucose based on the Etching of Gold Nanorods. *Scientific Reports* **2016,** *6*, 37879.

72. Polavarapu, L.; Pérez-Juste, J.; Xu, Q.-H.; Liz-Marzán, L. M., Optical sensing of biological, chemical and ionic species through aggregation of plasmonic nanoparticles. *Journal of Materials Chemistry C* **2014,** *2* (36), 7460-7476.

73. Schlücker, S., Surface-Enhanced Raman Spectroscopy: Concepts and Chemical Applications. *Angewandte Chemie International Edition* **2014,** *53* (19), 4756-4795.

74. Liu, H.; Zhang, L.; Lang, X.; Yamaguchi, Y.; Iwasaki, H.; Inouye, Y.; Xue, Q.; Chen, M., Single molecule detection from a large-scale SERS-active Au79Ag21 substrate. *Scientific Reports* **2011,** *1*, 112.

75. Ru, E. C. L.; Etchegoin, P. G., Single-Molecule Surface-Enhanced Raman Spectroscopy. *Annual Review of Physical Chemistry* **2012,** *63* (1), 65-87.

76. Fleischmann, M.; Hendra, P. J.; McQuillan, A. J., Raman spectra of pyridine adsorbed at a silver electrode. *Chemical Physics Letters* **1974,** *26* (2), 163-166.

77. Yamaguchi, A.; Fukuoka, T.; Takahashi, R.; Hara, R.; Utsumi, Y., Dielectrophoresis-enabled surface enhanced Raman scattering on gold-decorated polystyrene microparticle in micro-optofluidic devices for high-sensitive detection. *Sensors and Actuators B: Chemical* **2016,** *230*, 94-100.

78. Stetciura, I. Y.; Markin, A. V.; Ponomarev, A. N.; Yakimansky, A. V.; Demina, T. S.; Grandfils, C.; Volodkin, D. V.; Gorin, D. A., New Surface-Enhanced Raman Scattering Platforms: Composite Calcium Carbonate Microspheres Coated with Astralen and Silver Nanoparticles. *Langmuir* **2013,** *29* (12), 4140-4147.

79. Change, M. J. P. o. t. S. a. P. o. G., 2018 Food, Water, Energy and Climate Outlook.

80. *REN21, < 2018> < Renewables 2018 Global Status REport > Paris, REN21 Secretariat*

81. Becquerel, A., Mémoire sur les effets électriques produits sous l'influence des rayons solaires. *Comptes rendus de l, Académie des Sciences* **1839,** *9*, 561-567.

82. Chapin, D. M.; Fuller, C. S.; Pearson, G. L., A New Silicon p-n Junction Photocell for Converting Solar Radiation into Electrical Power. *Journal of Applied Physics* **1954,** *25* (5), 676-677.

83. NREL https://www.nrel.gov/ (accessed 10-15-2018).

84. Green, M. A., Thin-film solar cells: review of materials, technologies and commercial status. *Journal of Materials Science: Materials in Electronics* **2007,** *18* (1), 15-19.

85. NREL National Center for Photovoltaics. http://www.nrel.gov/ncpv/ (accessed 10-28-18).

86. B. O'regan, M. G., *Nature* **1991,** *353* (737).

87. Kwon, S.-W. R. a. W., *Korean Journal Chemical Engineering* **2011,** *28* (7), 1481-1494.

88. Gratzel, M., Recent Advances in Sensitized Mesoscopic Solar Cells. *Accounts Chem. Res.* **2009,** *42* (11), 1788-1798.

89. Kojima, A.; Teshima, K.; Shirai, Y.; Miyasaka, T., Organometal Halide Perovskites as Visible-Light Sensitizers for Photovoltaic Cells. *Journal of the American Chemical Society* **2009,** *131* (17), 6050-6051.

90. Lee, M. M.; Teuscher, J.; Miyasaka, T.; Murakami, T. N.; Snaith, H. J., Efficient Hybrid Solar Cells Based on Meso-Superstructured Organometal Halide Perovskites. *Science* **2012,** *338* (6107), 643-647.

91. Tang, C. W., Two-layer organic photovoltaic cell. *Applied Physics Letters* **1986,** *48* (2), 183-185.

92. Yu, G.; Heeger, A. J., Charge separation and photovoltaic conversion in polymer composites with internal donor/acceptor heterojunctions. *Journal of Applied Physics* **1995,** *78* (7), 4510-4515.

93. Cheng, P.; Zhan, X., Stability of organic solar cells: challenges and strategies. *Chemical Society Reviews* **2016,** *45* (9), 2544-2582.

94. Lee, C. H.; Yu, G.; Moses, D.; Pakbaz, K.; Zhang, C.; Sariciftci, N. S.; Heeger, A. J.; Wudl, F., Sensitization of the photoconductivity of conducting polymers by ${\mathrm{C}}_{60}$: Photoinduced electron transfer. *Physical Review B* **1993,** *48* (20), 15425-15433.

95. Yu, G.; Pakbaz, K.; Heeger, A. J., Semiconducting polymer diodes: Large size, low cost photodetectors with excellent visible-ultraviolet sensitivity. *Applied Physics Letters* **1994,** *64* (25), 3422-3424.

96. Nian, L.; Kan, Y.; Wang, H.; Gao, K.; Xu, B.; Rong, Q.; Wang, R.; Wang, J.; Liu, F.; Chen, J.; Zhou, G.; Russell, T. P.; Jen, A. K. Y., Ternary non-fullerene polymer solar cells with 13.51% efficiency and a record-high fill factor of 78.13%. *Energy & Environmental Science* **2018**.

97. Meng, L.; Zhang, Y.; Wan, X.; Li, C.; Zhang, X.; Wang, Y.; Ke, X.; Xiao, Z.; Ding, L.; Xia, R.; Yip, H.-L.; Cao, Y.; Chen, Y., Organic and solution-processed tandem solar cells with 17.3% efficiency. *Science* **2018**.

98. Wang, D. H.; Kim, D. Y.; Choi, K. W.; Seo, J. H.; Im, S. H.; Park, J. H.; Park, O. O.; Heeger, A. J., Enhancement of Donor–Acceptor Polymer Bulk Heterojunction Solar Cell Power Conversion Efficiencies by Addition of Au Nanoparticles. *Angewandte Chemie International Edition* **2011,** *50* (24), 5519-5523.

99. Kirkeminde, A.; Retsch, M.; Wang, Q.; Xu, G.; Hui, R.; Wu, J.; Ren, S., Surface-passivated plasmonic nano-pyramids for bulk heterojunction solar cell photocurrent enhancement. *Nanoscale* **2012,** *4* (15), 4421-4425.

100. Spyropoulos, G. D.; Stylianakis, M. M.; Stratakis, E.; Kymakis, E., Organic bulk heterojunction photovoltaic devices with surfactant-free Au nanoparticles embedded in the active layer. *Applied Physics Letters* **2012,** *100* (21), 213904.

101. Topp, K.; Borchert, H.; Johnen, F.; Tunc, A. V.; Knipper, M.; von Hauff, E.; Parisi, J.; Al-Shamery, K., Impact of the Incorporation of Au Nanoparticles into

Polymer/Fullerene Solar Cells. *The Journal of Physical Chemistry A* **2010,** *114* (11), 3981-3989.

102. Xue, M.; Li, L.; Tremolet de Villers, B. J.; Shen, H.; Zhu, J.; Yu, Z.; Stieg, A. Z.; Pei, Q.; Schwartz, B. J.; Wang, K. L., Charge-carrier dynamics in hybrid plasmonic organic solar cells with Ag nanoparticles. *Applied Physics Letters* **2011,** *98* (25), 253302.

103. Wu, B.; Wu, X.; Guan, C.; Fai Tai, K.; Yeow, E. K. L.; Jin Fan, H.; Mathews, N.; Sum, T. C., Uncovering loss mechanisms in silver nanoparticle-blended plasmonic organic solar cells. *Nature Communications* **2013,** *4*, 2004.

104. Wu, J.-L.; Chen, F.-C.; Hsiao, Y.-S.; Chien, F.-C.; Chen, P.; Kuo, C.-H.; Huang, M. H.; Hsu, C.-S., Surface Plasmonic Effects of Metallic Nanoparticles on the Performance of Polymer Bulk Heterojunction Solar Cells. *ACS Nano* **2011,** *5* (2), 959-967.

105. Tan, K.-S.; Chuang, M.-K.; Chen, F.-C.; Hsu, C.-S., Solution-Processed Nanocomposites Containing Molybdenum Oxide and Gold Nanoparticles as Anode Buffer Layers in Plasmonic-Enhanced Organic Photovoltaic Devices. *ACS Applied Materials & Interfaces* **2013,** *5* (23), 12419-12424.

106. Kao, C.-S.; Chen, F.-C.; Liao, C.-W.; Huang, M. H.; Hsu, C.-S., Plasmonic-enhanced performance for polymer solar cells prepared with inverted structures. *Applied Physics Letters* **2012,** *101* (19), 193902.

107. Woo, S.; Jeong, J. H.; Lyu, H. K.; Han, Y. S.; Kim, Y., In situ-prepared composite materials of PEDOT: PSS buffer layer-metal nanoparticles and their application to organic solar cells. *Nanoscale Research Letters* **2012,** *7* (1), 641.

108. Li, X.; Deng, Z.; Yin, Y.; Zhu, L.; Xu, D.; Wang, Y.; Teng, F., Efficiency enhancement of polymer solar cells with Ag nanoparticles incorporated into PEDOT:PSS layer. *Journal of Materials Science: Materials in Electronics* **2014,** *25* (1), 140-145.

109. Xie, F.-x.; Choy, W. C. H.; Sha, W. E. I.; Zhang, D.; Zhang, S.; Li, X.; Leung, C.-w.; Hou, J., Enhanced charge extraction in organic solar cells through electron accumulation effects induced by metal nanoparticles. *Energy & Environmental Science* **2013,** *6* (11), 3372-3379.

110. Xu, X.; Kyaw, A. K. K.; Peng, B.; Zhao, D.; Wong, T. K. S.; Xiong, Q.; Sun, X. W.; Heeger, A. J., A plasmonically enhanced polymer solar cell with gold–silica core–shell nanorods. *Organic Electronics* **2013,** *14* (9), 2360-2368.

111. Shen, W.; Tang, J.; Yang, R.; Cong, H.; Bao, X.; Wang, Y.; Wang, X.; Huang, Z.; Liu, J.; Huang, L.; Jiao, J.; Xu, Q.; Chen, W.; Belfiore, L. A., Enhanced efficiency of polymer solar cells by incorporated Ag–SiO2 core–shell nanoparticles in the active layer. *RSC Advances* **2014,** *4* (9), 4379-4386.

112. Janković, V.; Yang, Y.; You, J.; Dou, L.; Liu, Y.; Cheung, P.; Chang, J. P.; Yang, Y., Active Layer-Incorporated, Spectrally Tuned Au/SiO2 Core/Shell Nanorod-Based Light Trapping for Organic Photovoltaics. *ACS Nano* **2013,** *7* (5), 3815-3822.

113. Kippelen, B.; Brédas, J.-L., Organic photovoltaics. *Energy & Environmental Science* **2009,** *2* (3), 251-261.

114. Lee, S.; Lee, M.; An, J.; Ahme, H.; Im, C., Exciton Dynamics of P3HT:PCBM Blend Films with Different Polymer Regioregularities Using Transient Absorption Spectroscopy. *Molecular Crystals and Liquid Crystals* **2013,** *578* (1), 68-72.

115. Ohkita, H.; Ito, S., Transient absorption spectroscopy of polymer-based thin-film solar cells. *Polymer* **2011,** *52* (20), 4397-4417.

CHAPTER 2. DEVELOPMENT OF NOVEL SILICA COATING PROCEDURE FOR THE SYNTHESIS OF AG@SiO_2 CORE-SHELL NANOPARTICLES

2.1 Introduction

Core shell nanoparticles are multi-component materials consisting of an inner material (core) and outer layer/layers (shell). These materials have been realized in a wide range of combinations of organic and inorganic materials. Often the choice of material and geometry of core-shell particles is dictated by the desired properties required for the end use application.[1-4].

One particularly important class of these materials is plasmonic noble metal nanoparticles coated with metal oxides.[1, 5] Plasmonic properties of metal nanoparticle can be tailored through material selection, composition, size, or shape,[6-9] and are summarized in section 1.1.2. Metal NPs have a variety of useful properties the harsh environments required for application can induce aggregation, etching or dissolution, which can be detrimental to their plasmonic properties. The prominent approach to overcome these challenges is a thin coating of a chemically inert material such as silica. Silica is a particularly advantageous coating material as it is low cost, biocompatible, easily functionalized, and remarkably stable. These nanoscale coatings can provide colloidal stability, chemical stabilization, thermal stability, or electrical insulation. Silica coated

plasmonic core-shell particles have been exploited in a variety of biomedical,[10-11] photonic,[12] catalytic,[13-14] photovoltaics[15-16] and sensing applications.[17-20]

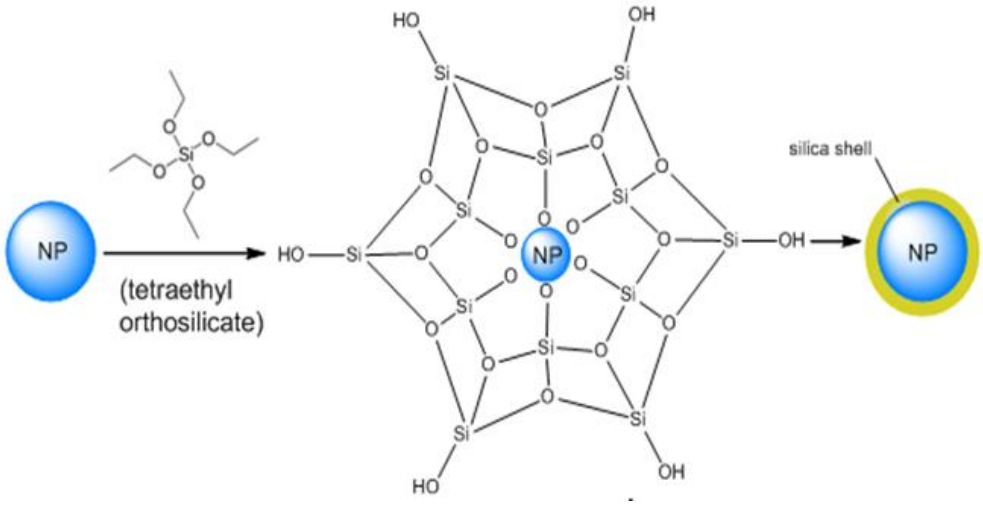

Figure 2.1. Schematic representation of silica coating process.

A wide range of silica coating methods are summarized in section 1.1.2.5. The Stober method,[21] is by far the most common route to coat preformed metal nanoparticles with a dense layer of silica shown in Figure 2.1. In this seeded growth method, the metal NPs act as a nucleation center for the condensation of silicic acids produced through the hydrolysis and condensation of TEOS in and alkaline ethanol/water solution. The reaction mechanism for this two-step process is shown in Figure 2.2. This method is effective for coating a variety of metals, with control over the shell thickness by tuning the TEOS/NP ratio. However, the stober method also suffers from several drawback such as elevated temperature, long reaction times,[22] slow reagent addition,[23] and need for surface priming/functionalization before shell coating.[24-25] The work reported in this chapter presents a novel method for overcoming these challenges to produce Ag@SiO_2 core-shell

NP in a one-pot reaction at room temperature, that requires no pretreatment and a two hour reaction time.

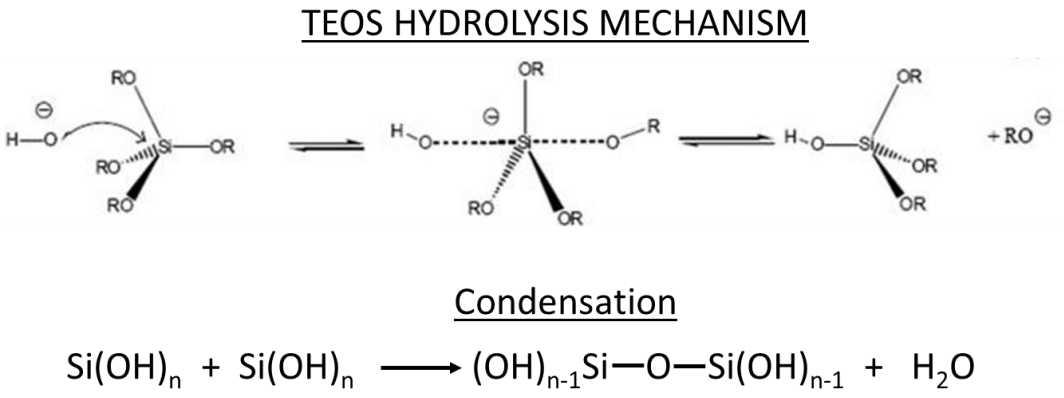

Figure 2.2. Reaction mechanism for base catalyzed hydrolysis and condensation of TEOS.

2.2 Results and Discussion

2.2.1 Silver Nanoparticle Synthesis and Characterization

The silver nanoparticles used in this study were synthesized as previously reported.[26] Silver nanoparticles are produced via the reduction of silver ions by ascorbic acid and stabilized with tri-sodium citrate capping agent. This method provides tunability of the nanoparticle size by simply adjusting the pH of the reaction medium. The pH of the reaction media dictates the reactivity of ascorbic and mediates the reduction rate of silver ions and the nucleation of silver nanoparticles. Ag NP synthesized at pH 10.5, 9.0 and 6.0 are shown in Figure 2.3, have an average particle size of 23.2 ± 3.6 nm, 49.2 ± 4.6 nm, and 69.2 ± 5.5 nm (100 particles average from TEM imaging), respectively.

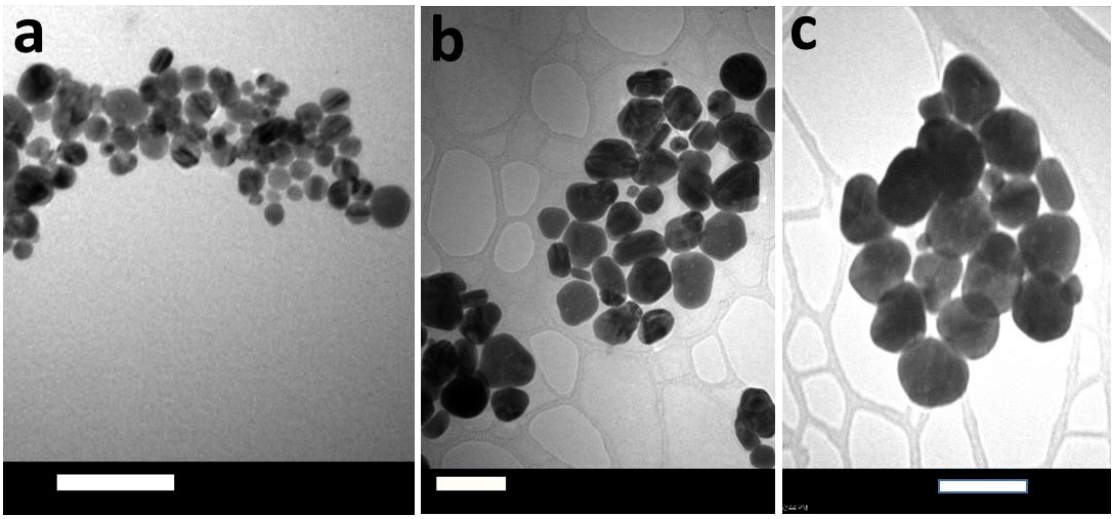

Figure 2.3 TEM images of Ag NPs synthesized at various pH values. a) pH = 10.5 b) pH = 9.0 c) pH = 6.0. Scale bars 100 nm.

The as synthesized quasi-spherical particles are subjected to incubation in a 100 C^{o} hot bath without stirring for 30 min to promote intra-particle ripening. This ripening results in more spherical particles with a narrow size distribution. This effect can be observed in Figure 2.4, where the peak of the LSPR shifts from 415 nm (pH 10.5), 424 nm (pH 9.0), and 428 nm (pH 6.0), to 403 nm, 420 nm, and 417 nm respectively. Longer ripening time resulted in Ostwald ripening leading to long wavelength absorption from aggregation. This fast and facile method is ideal for this study to reproducibly produce large quantities of silver nanoparticles, with simple control of the nanoparticle size.

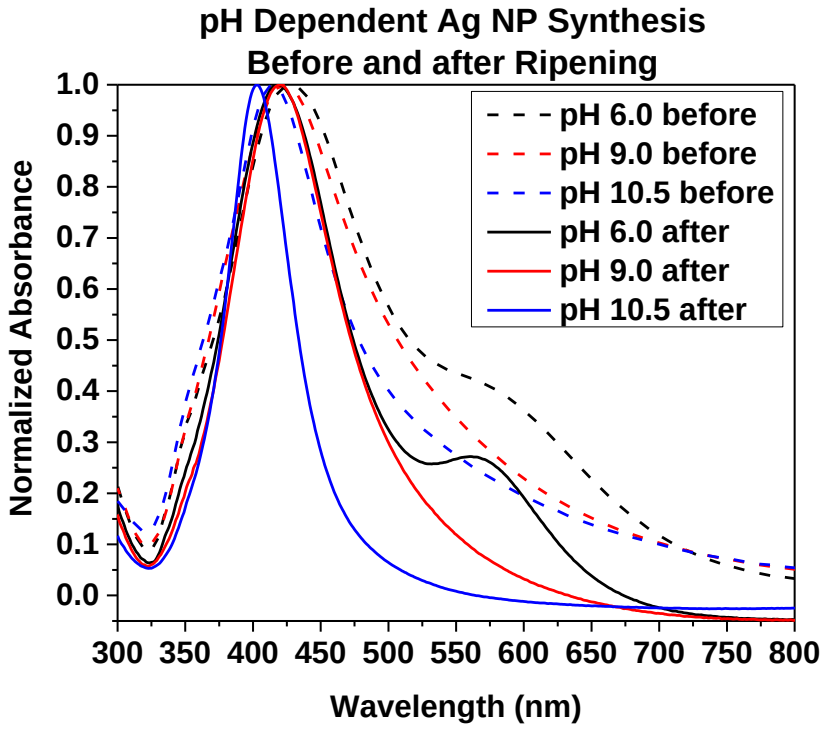

Figure 2.4 UV/Vis spectra of AgNP's plasmon resonance before and after ripening process, synthesized under various pH conditions.

2.2.2 Optimization of Silica Shell Coating

As discussed in Section 2.1, the effectiveness of the silica shell formation is affected by a number of factors such as nanoparticle concentration, capping ligand, NP size or concentration. For these reasons literature methods often need to be tailored to meet each laboratory's individual needs. Additionally, previously reported methods suffer from long reaction times, tedious synthetic procedures, and often overlook very thin shell formation, these challenges are addressed herein. For this thesis, single core particles with a thin (≈ 5nm) silica shell are required. Utilizing the Stober method,[21] the reaction variables are systematically optimized resulting in a novel silica coating procedure. All reactions in this study were conducted utilizing a 20 ml (95/5% EtOH/H_2O) solvent system.

2.2.2.1 Dependence of TEOS Concentration on Silica Shell Thickness

In an ideal procedure, the silica shell thickness could be controlled systematically by the adjustment of the silica precursor tetraethylorthosilicate (TEOS) concentration. To evaluate the role TEOS concentration plays in the silica coating process a series of reactions with varying concentrations of TEOS were conducted. The reaction parameters and corresponding shell thicknesses are shown in Table 1.

Table 1. Summary of reaction parameters for the investigation of TEOS concentration dependence on the silica coating process.

Constant Parameters	TEOS Volume (µl) (10 mM EtOH, 150 µl/30min)	Shell Thickness (nm) (100 NP average)
5.0 ml AgNPs	600	7.3 ± 2.4
650 µl ammonia (30 wt%)	750	12.3 ± 2.1
	900	19.3 ± 1.9
30 ºC 24 hrs-	1050	29.4 ± 3.2
After TEOS addition	1200	35.2 ± 3.8

It is evident from the TEM images shown in Figure 2.5, that the TEOS concentration directly correlates to shell thickness, where the shell thickness decreases from 35.2 ± 3.8 nm (1200 µl TEOS) down to 7.3 ± 2.4 nm (600 µL TEOS) sample. Although the shell thickness correlates to the TEOS concentration, the TEM results also show multiple cores within the shell structure. This effect can also be visualized by the growing long wavelength absorption in the LSPR of the core-shell particles shown in Figure 2.6. Interparticle coupling of the aggregated particles leads to this long wavelength absorption,[27] and can be used to monitor the degree of aggregation during the coating

process. Manipulating the concentration of TEOS in the reaction mixture controls the silica shell thickness, it has less of an effect on the degree of aggregation. There is a slight increase in aggregation at lower TEOS concentrations possibly due to NP aggregation before sufficient TEOS condensation.

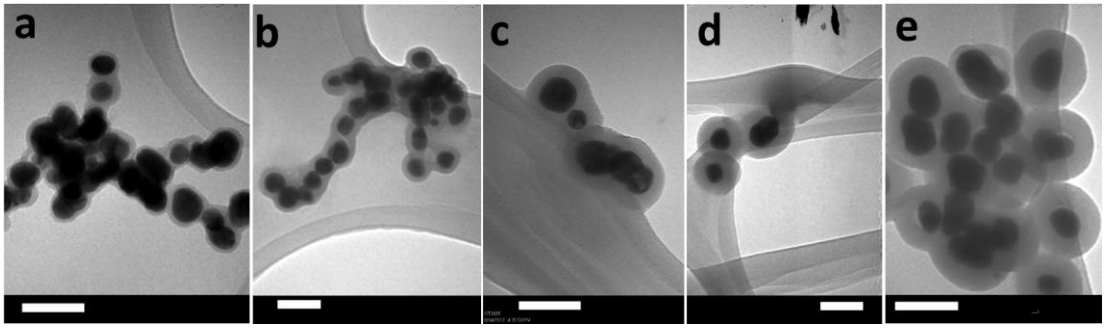

Figure 2.5 TEM images of $AgSiO_2$ NP synthesized with various amounts of TEOS. a) 600 µl, b) 750 µl, c) 900 µl, d) 1050 µl, e) 1200 µl. Scale bars 100 nm.

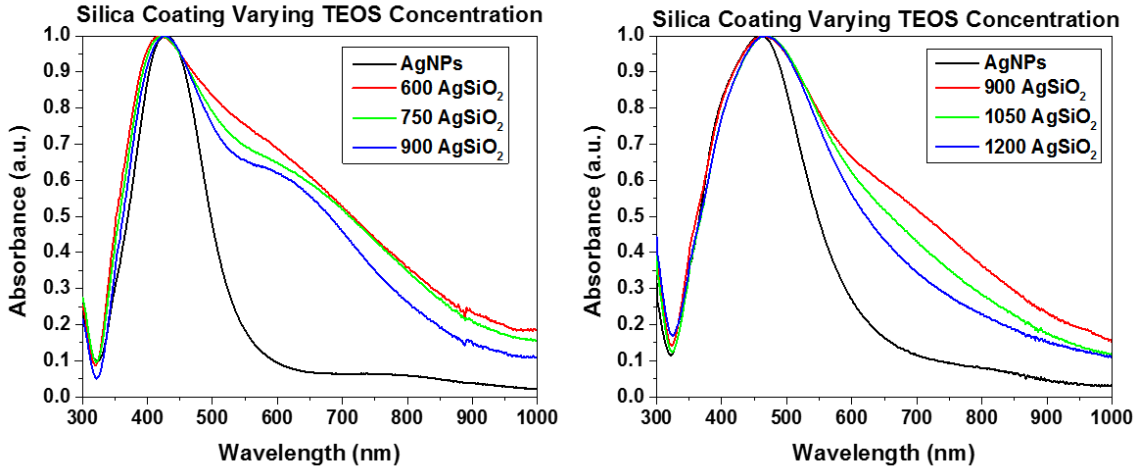

Figure 2.6 UV/Vis spectra comparing the LSPR of $AgSiO_2$ NP synthesized with varying concentration of TEOS precursor.

Aliquots of the previous reactions were taken at various times throughout the reaction to monitor the shell coating process, where 2 hr and 4 hr samples were taken before

heating commenced. The sample taken at 2 hrs from the 600 µl TEOS sample, along with 4 hr and 16 hr samples from the 1200 µl TEOS sample are shown in Figure 2.7. Silica shell formation is already apparent at 2hrs for the 600 µl TEOS sample without any heating needed, and appear to have a uniform coating with a thickness under 5 nm. The large scattering background seen in Figure 2.7, for the 2 hr sample, is thought to be from uncoated aggregates from the washing process. The 1200 µl sample shows complete coating of all nanoparticles at the 4hr mark and by 16 hrs excessive shell growth and increased aggregation is observed. These results show the 24 hr reaction period at an elevated temperature is excessive and may increase agglomeration.

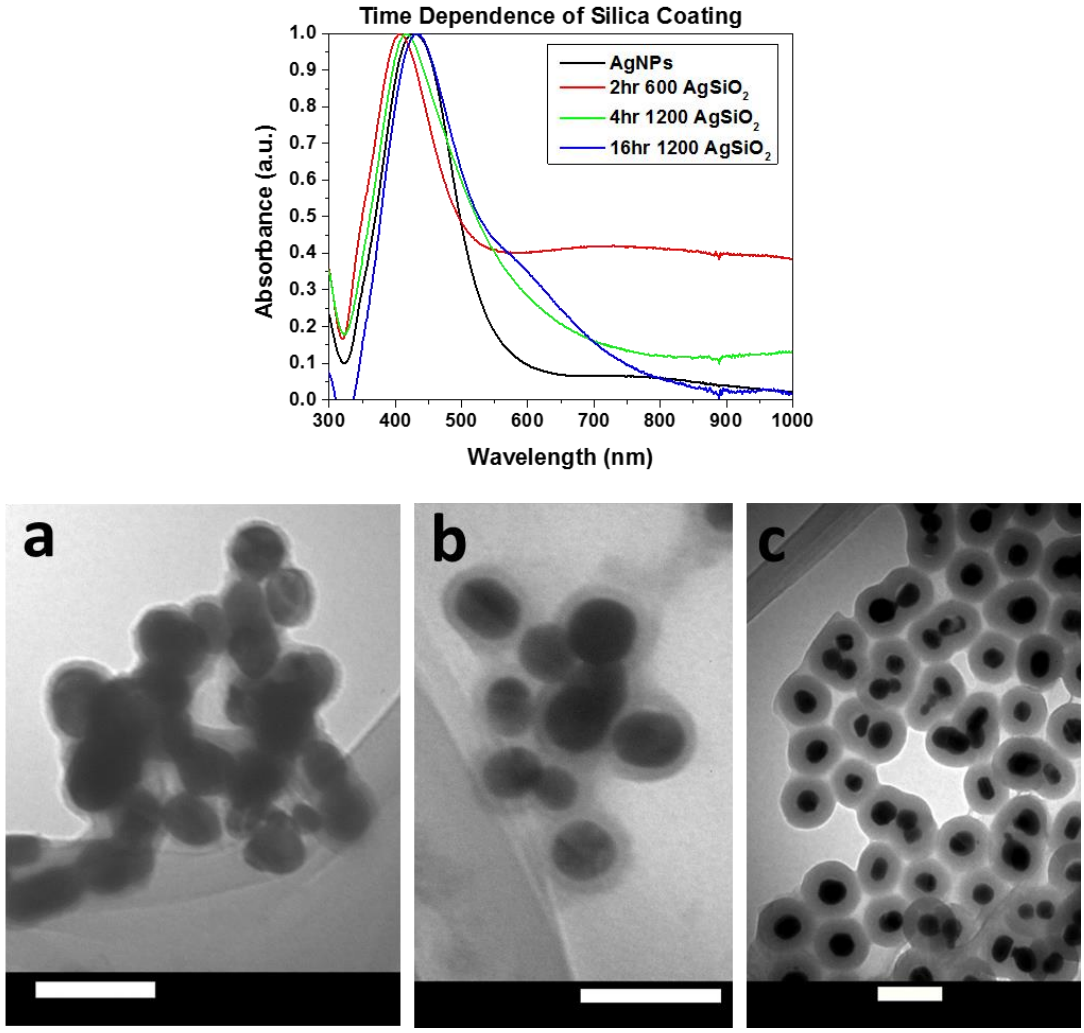

Figure 2.7 UV/Vis of the LSPR of $AgSiO_2$ taken at various time during reaction (top). TEM images monitoring the silica shell thickness taken during the silica coating reaction (bottom). a) 2 hrs 6oo µl (< 5 nm), b) 4 hrs 1200 µl (10.6 ± 2.3 nm), c) 16 hrs 1200 µl (21.9 ± 2.6). Shell thickness (average 100 particles) in parenthesis. Scale bars 100 nm.

2.2.2.2 Nanoparticle Concentration and Aggregation

Although, relatively thin shells were produced for the lowest TEOS concentration used in Figure 2.5, a significant degree of aggregation was observed. To further understand the factors that affect the degree of aggregation with in the silica shell reactions varying the NP concentration (3 ml, 5 ml, 8 ml), while maintaining constant TEOS and base

concentration, were conducted. Figure 2.8 shows there is a clear correlation between nanoparticle concentration and the degree of aggregation. The LSPR absorbance spectra and the associated TEM images indicate a critical threshold that exists between the ratio of NP to TEOS concentration, above which multi-core silica masses form and below this threshold single core-shell particles are obtained.

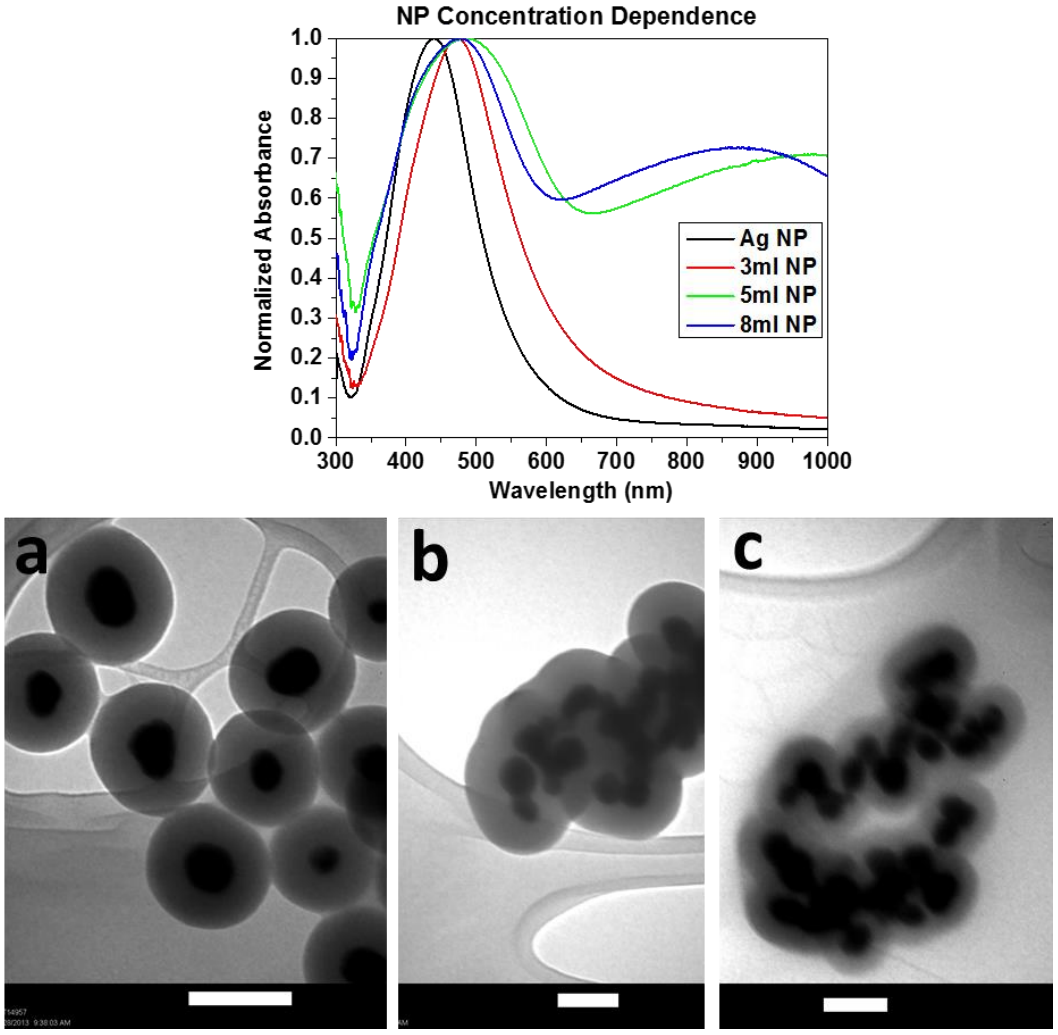

Figure 2.8 UV/Vis spectra of $AgSiO_2$ NP synthesized with varying NP concentration (top). TEM images if NP concentration investigation (bottom). a) 3.0 ml AgNP. b) 5.0 ml AgNP, c) 8.0 ml AgNP. Scale bars 100 nm.

2.2.2.3 Effects of Catalytic Base Selection and Concentration

Kobayashi *et al.*, demonstrated that aqueous ammonia can dissolve the silver nanoparticles to form a soluble silver complex and induce aggregation during the coating process.[28] It was concluded that dimethylamine (DMA) is more suitable for silica shell formation.

Table 2. Reaction parameters used to determine the effect of base selection and TEOS addition rate on the formation of core-shell particles.

Constant Parameters	TEOS (10 mM EtOH) Addition Rate
5.0 ml AgNPs 650 µl (NH_3 or DMA) 8 TEOS additions Shaken 5 hrs No Heat	150 µl/30 min 300 µl/30 min 500 µl/30 min

The reaction parameters shown in Table 2 were used to determine the optimal catalytic base for core-shell synthesis, while simultaneously investigating the rate of TEOS addition. Eight TEOS addition were used for all samples, resulting in total TEOS addition of 1.2 ml, 2.4 ml, and 4 ml, all reactions were stopped one hour after the final TEOS addition. A clear reduction in long wavelength LSPR absorption for the DMA synthesis as compared to ammonia is seen in Figure 2.9. The substitution of ammonia with DMA drastically reduces the aggregation during silica shell formation. Increasing the TEOS addition rate and total TEOS concentration not only increases the shell thickness, but also clearly increases agglomeration within the shell structure as seen in Figure 2.9C. This result

is attributed to the increased rate of hydrolysis and condensation at high TEOS concentrations. This data clearly shows that DMA is the preferred base for reducing aggregation during shell formation.

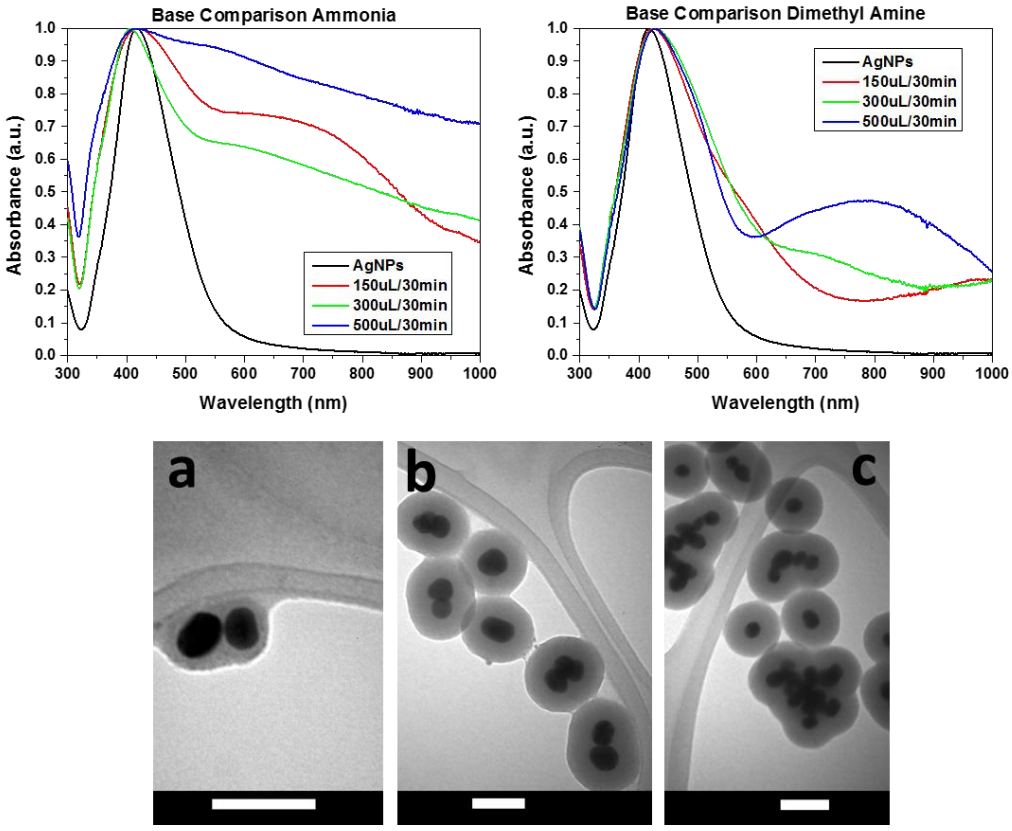

Figure 2.9 UV/Vis LSPR spectra comparing the synthesis of $AgSiO_2$ NP using ammonia (top left), and DMA (top right). TEM images of DMA synthesis (bottom). a) 150 µl/30 min, b) 300 µl/30 min, c) 500 µl/30 min. Scale bars 100 nm.

It is clear that DMA is the preferred base for reducing aggregation, the optimal concentration of DMA appears relevant to achieve the goal of single core thin shell particles. The set of nanoparticle spectra in Figure 2.10 were synthesized with constant NP concentration (5ml). The first set was synthesized with constant TEOS addition rates (150 µl/ 30 min, 1200 µl total) and with DMA concentrations of 250 µl, 450 µl, and 650 µl.

These samples were reacted for 5 hrs, one hour after the TEOS addition was completed. The samples with a single initial TEOS addition were reacted for 2 hrs, which was demonstrated, in Section 2.2.2.1, to be sufficient for shell formation.

Particles synthesized with the slow TEOS addition showed incomplete shell formation, but the LSPR spectra shown in Figure 2.10 demonstrate that the degree of aggregation decreases at lower base concentration. More consequently, the 1000 µl single TEOS addition sample shows significantly less aggregation than the 1200 µl slow addition counterpart. The 2000 µl single addition sample shows no signs of long wavelength absorption, and the single core particles can be seen in Figure 2.10. A slight red shift of the LSPR spectra due to the change in dielectric environment around the particles is observed, as expected.[27] These results demonstrate that the slow addition of TEOS is detrimental to the formation of single core particles, likely due to aggregation of NPs before the requisite amount of hydrolyzed TEOS is available for condensation.

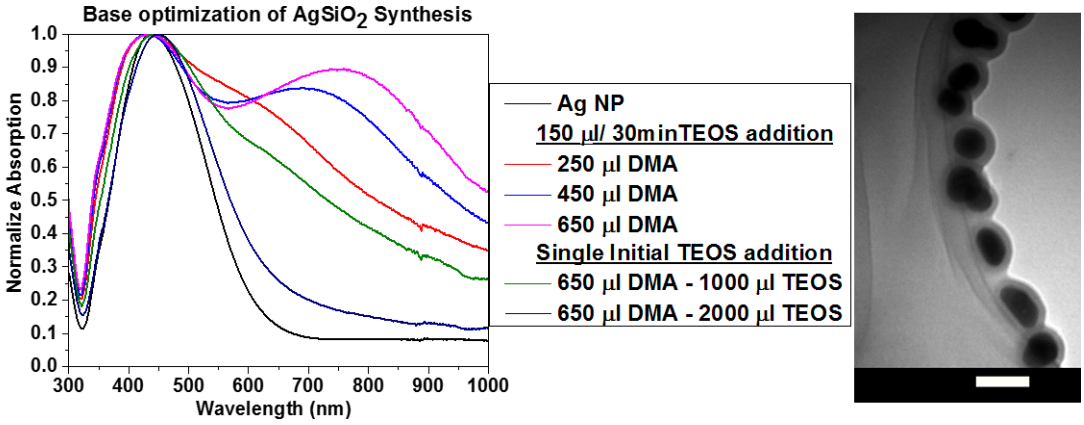

Figure 2.10 Comparison of the UV/Vis absorption of the LSPR of the $AgSiO_2$ synthesized with 1) Various amounts of DMA and constant TEOS concentration or 2) Constant DMA concentration and various TEOS concentrations added in single aliquot (left). TEM image of 650 µl DMA and 2000 µl TEOS. Scale bar 100 nm.

To fully understand the effect of DMA concentration has on the silica shell formation, several reactions were conducted with various DMA (50 µl, 200 µl, 400 µl, 650 µl) concentrations and constant NP concentration (5 ml), a single initial TEOS (10 mM in EtOH) addition of 1.7 ml, and a 2 hr reaction time. Figure 2.11 shows there is no change to the LSPR absorption as the DMA concentration is reduce from 650 µl to 200 µl, whereas, 50 µl DMA appears quite aggregated and no silica formation is seen. Analysis of TEM images, Figure 2.11, show single core particles are obtained, which implies the rate of hydrolysis is relatively unaffected by the reduction in DMA concentration. Analogously, the rate of condensation also appears unchanged, as only a small reduction in shell thickness from 21.5 ± 1.8 nm (650 µl DMA) to 16.7 ± 2.3 nm (200 µl DMA). The optimal DMA concentration was found to be 200 µl for the reaction conditions studied here and will be used from this point forward.

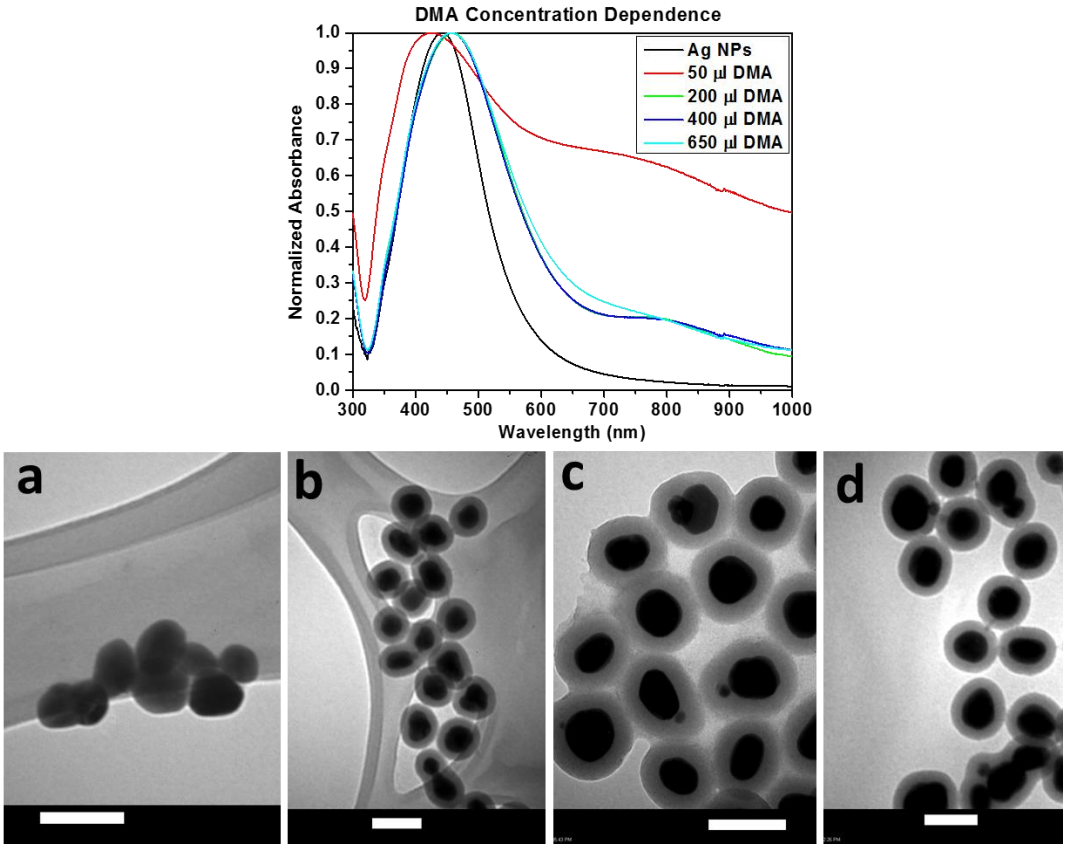

Figure 2.11 UV/Vis spectra of the LSPR of $AgSiO_2$ NPs synthesized with various amounts of DMA, with all the TEOS was added at beginning of the reaction (top). TEM images $AgSiO_2$ NPs synthesized with a) 50 µl DMA, b) 200 µl DMA, c) 400 µl DMA, d) 650 µl DMA (bottom). Scale bars 100 nm.

2.3 Conclusion: Novel Silica Coating Procedure for $AgSiO_2$ NP

In summary, maintaining a solvent system of 20 ml (95/5% $EtOH/H_2O$), it was demonstrated that DMA is preferable over NH_3. The optimal DMA (200 µl) concentration minimized aggregation and maintained the individual core-shell structure. At high NP concentrations multi-core particles were formed, whereas at concentrations of 3.0 ml and below, a clear transition to single-core particles was seen. Time dependent trials showed shell formation was complete within two hours and, where no heating was required. Longer reaction times resulted in an increase in shell thickness and induced aggregation at very

high TEOS concentrations. Slow addition of TEOS over extended periods of time has been reported to reduce aggregation and result in ideal core-shell geometry. A single initial TEOS addition is preferential for the short reaction times used in this study. Slow addition does not provide enough hydrolyzed TEOS for shell formation on the two hour time scale, resulting in increased aggregation. Ideal core-shell nanoparticles were synthesized using 3 ml AgNP, 200 µl DMA, and 600-1500 µl. Simply by adjusting the TEOS concentration the silica shell thickness can be tuned from ≈ 4 nm to > 50 nm, as shown in Figure 2.12. The LSPR, Figure 2.13, shows a slight redshift due to the change in refractive index surrounding the particle, as expected. The shape of the LSPR remains relatively unchanged, which is indicative of ideal core-shell particles, free of aggregation.

This novel method for the synthesis $AgSiO_2$ NP presented here has several advantages over traditional literature methods. This simple one-pot reaction eliminates the need for surface priming or tedious slow TEOS addition, reduces the reaction times 6-12 fold, and requires no heating. Removing the heat component allows the reaction to be agitated on a vortex mixer, where up to 16 batches can be synthesized concurrently in two hours. This method should quickly become the state-of-the-art for the production of $AgSiO_2$.

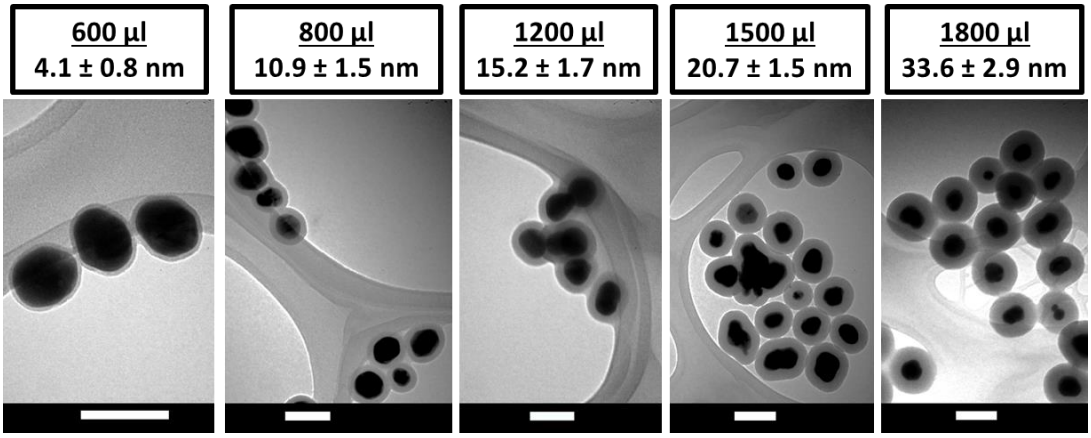

Figure 2.12. TEM images of $AgSiO_2$ NP synthesized w/ various amounts of TEOS utilizing the optimized novel method. Scale bars 100 nm.

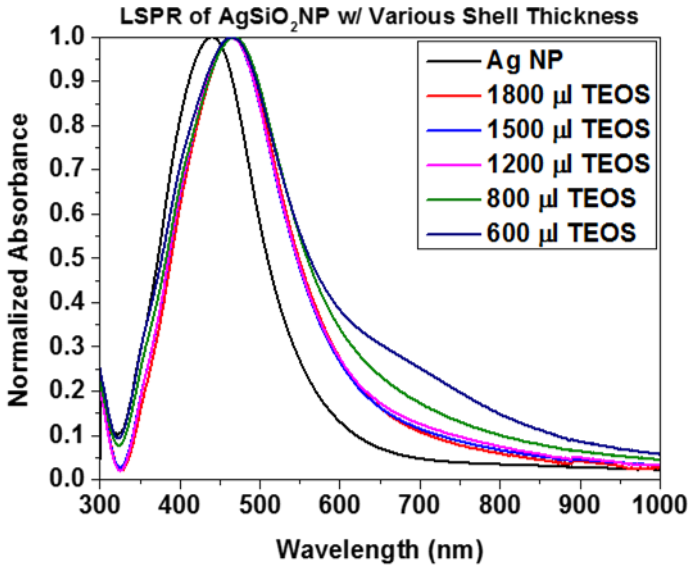

Figure 2.13. UV/Vis spectra of LSPR from $AgSiO_2$ NP synthesized w/ various amounts of TEOS utilizing the optimized novel method.

2.4 Experimental Methods:

2.4.1 Ag Nanoparticle Synthesis

Quasi-spherical silver nanoparticles were synthesized via a previously reported method.[26] In short, 12.5 mL ascorbic acid (4.8 mM), 8.825 mL sodium citrate (1 w/w %), were added to 80 mL DIW. The reaction mixture is adjusted to pH 9.5 with 0.1 M citric acid and 0.1 M NaOH. The solution was placed in 30 °C hot bath, and 1 mL aqueous solution of $AgNO_3$ (0.1 M) was injected into the reaction mixture and stirred at 1200 RPM for 15 min. The contents of the reaction flask were then transferred to an oil bath at 100 °C for 30 min without stirring and then placed in ice bath to quench the reaction.

2.4.2 Ag@SiO_2 Nanoparticle Synthesis

The silica coating of Ag nanoparticles was performed using a modified procedure from previous reports.[28,22] 2.0 mL of AgNP, filtered through 0.8 µm Nylon filter to remove large or aggregated nanoparticles, were added to 20 mL of 95/5% ethanol water mixture in a 50 mL centrifuge tube. 600-1200 µL TEOS (10.0 mM in EtOH) were added and then followed by the addition of 200 µL DMA. The reaction mixture was then shaken with vortex mixer for 2 hrs. Ag@SiO_2 NPs were collected using a centrifuge operating at 8000 RPM for 15 minutes. The resultant Ag@SiO_2 NP were washed 3 times each with ethanol and water, and then dispersed in 3.0 mL of ethanol.

2.4.3 Nanoparticle Characterization

AgNP and Ag@SiO_2 NP were drop-casted on carbon coated copper TEM grids (Electron Microscopy Science). TEM images were collected on a JEOL 100CX II TEM with a 100 keV accelerating voltage. Ag and $AgSiO_2$ LSPR absorption measurements were collected with a Shimadzu UV/Vis/NIR spectrometer, referenced to water and EtOH respectively.

2.5 REFERENCES

1. Ghosh Chaudhuri, R.; Paria, S., Core/Shell Nanoparticles: Classes, Properties, Synthesis Mechanisms, Characterization, and Applications. *Chemical Reviews* **2012,** *112* (4), 2373-2433.

2. El-Toni, A. M.; Habila, M. A.; Labis, J. P.; Alothman, Z. A.; Alhoshan, M.; Elzatahry, A. A.; Zhang, F., Design, synthesis and applications of core–shell, hollow core, and nanorattle multifunctional nanostructures. *Nanoscale* **2016,** *8* (5), 2510-2531.

3. Kumar, K. S.; Kumar, V. B.; Paik, P., Recent Advancement in Functional Core-Shell Nanoparticles of Polymers: Synthesis, Physical Properties, and Applications in Medical Biotechnology. *Journal of Nanoparticles* **2013,** *2013*, 24.

4. Gawande, M. B.; Goswami, A.; Asefa, T.; Guo, H.; Biradar, A. V.; Peng, D.-L.; Zboril, R.; Varma, R. S., Core–shell nanoparticles: synthesis and applications in catalysis and electrocatalysis. *Chemical Society Reviews* **2015,** *44* (21), 7540-7590.

5. Liu, S.; Regulacio, M. D.; Tee, S. Y.; Khin, Y. W.; Teng, C. P.; Koh, L. D.; Guan, G.; Han, M.-Y., Preparation, Functionality, and Application of Metal Oxide-coated Noble Metal Nanoparticles. *The Chemical Record* **2016,** *16* (4), 1965-1990.

6. Grzelczak, M.; Pérez-Juste, J.; Mulvaney, P.; Liz-Marzán, L. M., Shape control in gold nanoparticle synthesis. *Chemical Society Reviews* **2008,** *37* (9), 1783-1791.

7. Jain, P. K.; Huang, X.; El-Sayed, I. H.; El-Sayed, M. A., Review of Some Interesting Surface Plasmon Resonance-enhanced Properties of Noble Metal Nanoparticles and Their Applications to Biosystems. *Plasmonics* **2007,** *2* (3), 107-118.

8. Rycenga, M.; Cobley, C. M.; Zeng, J.; Li, W.; Moran, C. H.; Zhang, Q.; Qin, D.; Xia, Y., Controlling the Synthesis and Assembly of Silver Nanostructures for Plasmonic Applications. *Chemical Reviews* **2011,** *111* (6), 3669-3712.

9. Genç, A.; Patarroyo, J.; Sancho-Parramon, J.; Bastús Neus, G.; Puntes, V.; Arbiol, J., Hollow metal nanostructures for enhanced plasmonics: synthesis, local plasmonic properties and applications. In *Nanophotonics*, 2017; Vol. 6, p 193.

10. Chatterjee, K.; Sarkar, S.; Jagajjanani Rao, K.; Paria, S., Core/shell nanoparticles in biomedical applications. *Advances in Colloid and Interface Science* **2014,** *209*, 8-39.

11. Zhao, T.; Nguyen, N.-T.; Xie, Y.; Sun, X.; Li, Q.; Li, X., Inorganic Nanocrystals Functionalized Mesoporous Silica Nanoparticles: Fabrication and Enhanced Bio-applications. *Frontiers in Chemistry* **2017,** *5* (118).

12. Chen, G.; Ågren, H.; Ohulchanskyy, T. Y.; Prasad, P. N., Light upconverting core–shell nanostructures: nanophotonic control for emerging applications. *Chemical Society Reviews* **2015,** *44* (6), 1680-1713.

13. Zhang, Q.; Lee, I.; Joo, J. B.; Zaera, F.; Yin, Y., Core–Shell Nanostructured Catalysts. *Accounts of Chemical Research* **2013,** *46* (8), 1816-1824.

14. Sharma, R. K.; Yadav, M.; Gawande, M. B., Silica-Coated Magnetic Nano-Particles: Application in Catalysis. In *Ferrites and Ferrates: Chemistry and Applications in Sustainable Energy and Environmental Remediation*, American Chemical Society: 2016; Vol. 1238, pp 1-38.

15. Choi, H.; Lee, J.-P.; Ko, S.-J.; Jung, J.-W.; Park, H.; Yoo, S.; Park, O.; Jeong, J.-R.; Park, S.; Kim, J. Y., Multipositional Silica-Coated Silver Nanoparticles for High-Performance Polymer Solar Cells. *Nano Letters* **2013,** *13* (5), 2204-2208.

16. Jang, Y. H.; Jang, Y. J.; Kim, S.; Quan, L. N.; Chung, K.; Kim, D. H., Plasmonic Solar Cells: From Rational Design to Mechanism Overview. *Chemical Reviews* **2016,** *116* (24), 14982-15034.

17. Kumar, P.; Kim, K.-H.; Bansal, V.; Kumar, N.; Bhaskarwar, A. N., Chapter 8 - Core–shell nanostructures as a platform for sensing applications. In *Metal Semiconductor Core-Shell Nanostructures for Energy and Environmental Applications*, Gupta, R. K.; Misra, M., Eds. Elsevier: 2017; pp 179-196.

18. Cha, M. G.; Kim, H.-M.; Kang, Y.-L.; Lee, M.; Kang, H.; Kim, J.; Pham, X.-H.; Kim, T. H.; Hahm, E.; Lee, Y.-S.; Jeong, D. H.; Jun, B.-H., Thin silica shell coated Ag assembled nanostructures for expanding generality of SERS analytes. *PLOS ONE* **2017,** *12* (6), e0178651.

19. Singh, S.; Devi, P.; Singh, D.; Jain, D. V. S.; Singla, M. L., Sensing behavior of silica-coated Au nanoparticles towards nitrobenzene. *Gold Bulletin* **2012,** *45* (2), 75-81.

20. Mocan, T.; Matea, C. T.; Pop, T.; Mosteanu, O.; Buzoianu, A. D.; Puia, C.; Iancu, C.; Mocan, L., Development of nanoparticle-based optical sensors for pathogenic bacterial detection. *Journal of Nanobiotechnology* **2017,** *15* (1), 25.

21. Stöber, W.; Fink, A.; Bohn, E., Controlled growth of monodisperse silica spheres in the micron size range. *Journal of Colloid and Interface Science* **1968,** *26* (1), 62-69.

22. Liu, S.; Zhang, Z.; Han, M., Gram-Scale Synthesis and Biofunctionalization of Silica-Coated Silver Nanoparticles for Fast Colorimetric DNA Detection. *Analytical Chemistry* **2005,** *77* (8), 2595-2600.

23. Liu, F.; Nunzi, J.-M., Phosphorescent organic light emitting diode efficiency enhancement using functionalized silver nanoparticles. *Applied Physics Letters* **2011,** *99* (12), 123302.

24. Liz-Marzán, L. M.; Giersig, M.; Mulvaney, P., Homogeneous silica coating of vitreophobic colloids. *Chemical Communications* **1996,** (6), 731-732.

25. Cheng, D.; Xu, Q.-H., Separation distance dependent fluorescence enhancement of fluorescein isothiocyanate by silver nanoparticles. *Chemical Communications* **2007,** (3), 248-250.

26. Qin, Y.; Ji, X.; Jing, J.; Liu, H.; Wu, H.; Yang, W., Size control over spherical silver nanoparticles by ascorbic acid reduction. *Colloids and Surfaces A: Physicochemical and Engineering Aspects* **2010,** *372* (1–3), 172-176.

27. Ghosh, S. K.; Pal, T., Interparticle Coupling Effect on the Surface Plasmon Resonance of Gold Nanoparticles: From Theory to Applications. *Chemical Reviews* **2007,** *107* (11), 4797-4862.

28. Kobayashi, Y.; Katakami, H.; Mine, E.; Nagao, D.; Konno, M.; Liz-Marzán, L. M., Silica coating of silver nanoparticles using a modified Stöber method. *Journal of Colloid and Interface Science* **2005,** *283* (2), 392-396.

CHAPTER 3. ADHESION ENHANCEMENTS AND SERS ACTIVITY OF AG AND AG@SiO_2 NANOPARTICLE DECORATED RAGWEED POLLEN MICRO-PARTICLE SENSOR.

3.1 Introduction

Surface-enhanced Raman scattering (SERS) has become a very powerful tool across many scientific disciplines, including but not limited to chemical analysis,[1] single molecule detection,[2] electrochemistry,[3] and in-vivo biological sensing.[4] Localized surface plasmon resonances (LSPR), produced by excitation of metallic nanostructures, result in an amplification of electromagnetic fields on or near to the surface of the nanostructure, with the strongest field enhancements in the gaps between closely interacting metal nanostructures known as "hot spots".[5] SERS occurs when molecules interact with these extraordinarily enhanced electromagnetic fields. The wavelength and intensity of the LSPR depends on the nanoparticle composition, size, and shape of the nanostructure, and thus a large array of SERS substrates have been fabricated and reviewed in the literature.[6] There are two general types of SERS substrates: lithographically fabricated metal nanostructures and synthetically produced colloidal metal nanoparticles (NPs). Lithographically fashioned nano-hole arrays,[7] periodic nanoparticle arrays fabricated with E-beam lithography and template techniques,[8,9] nanostructured gratings,[10] and fabricated nano-pillar arrays,[11] have been used to develop SERS substrates with exquisite control of LSPR characteristics but require complex and expensive instrumentation to fabricate such nanostructures. Colloidal metal NPs can be synthesized in solution and can be formed in a variety of sizes and shapes

to manipulate the LSPR.[6] Although colloidal NPs are easily synthesized they are often disperse in terms of size and shape as compared to their fabricated counterparts, and susceptible to coagulation. Additionally, they're not typically detectable by traditional optical microscopy techniques. Metal NPs have been immobilized on a variety of substrates, including micro-particles and SERS active micro-particle substrates offer a method to extend the nanoparticle LSPR properties to the micro-particle size domain. Polymeric,[12] silica,[13] polystyrene,[14] and magnetic particles[15] have been coated with a variety of metal nanostructures via electroless plating,[16] and electrostatic hetero-coagulation to create SERS active composite particles.[17,18] These types of 3-D SERS substrates offer a high surface area-to-volume ratio and can be dispersed in aqueous solutions making them effective platforms for potential biological or chemical sensing applications. Biological specimens have a transparency window in the near infrared region (NIR) (700-1400 nm) where absorption and auto-fluorescence is minimized.[19] Thus, the LSPR of the SERS substrate must be excitable in the NIR region to be applicable for biological samples.

In situ reduction of Ag provided a route to metallization of the sporopollenin (ragweed and rye pollen) micro-particles, which were used to identify Raman signals from compounds within the pollen exine.[20] In this chapter ragweed (RW) pollen exine were coated with preformed silver nanoparticles (AgNP) and silica coated silver nanoparticles ($Ag@SiO_2$) NPs. The ragweed (RW) pollen exine is a chemically and mechanically robust micro-particle, and due to its "spiky morphology" the RW pollen exhibit substantially higher surface area-to-volume than similarly sized spherical particles,[21,22] and display strong adhesive properties. Additionally, ragweed pollen have been shown to exhibit two-

photon excited fluorescence.[23] Thus, the pollen exine provides an adhesive micro-particle with an intrinsic 2-photon fluorescence signature and a high surface area to volume ratio, which makes it an interesting substrate for the development into a multifunctional composite SERS particulate sensor.

3.2 Results and Discussion

3.2.1 Pollen Surface Functionalization and Characterization

A sequential base/acid treatment was used to remove pollenkitt and proteins from the pollen exine, as well as to remove the pollen's internal cellular contents. The resulting cleaned ragweed (BA-RW) consists only of the pollen exine, which is composed of sporopollenin, a robust crosslinked polymer containing lipid and phenolic groups. To prepare the BA-RW pollen for nanoparticle decoration, (3-aminopropyl)-triethoxysilane (APTES) was used to functionalize the pollen surface to create an amine terminated surface (APTES-RW). SEM images of before and after APTES treatment are shown in Figure 3.1.

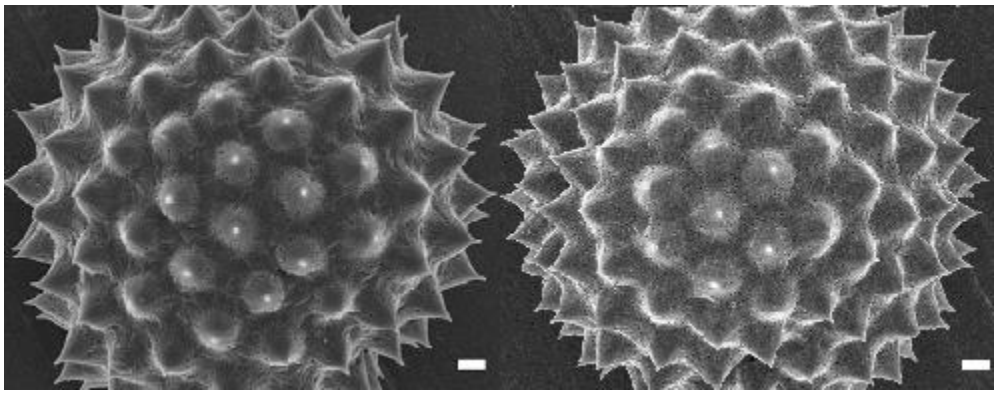

Figure 3.1. SEM images of BA-RW (left), APTES-RW (right). Scale bars 1µm.

Zeta potential measurements of BA-RW, APTES-RW, AgNPs and Ag@SiO2 NPs are shown in Figure 3.2. BA-RW, AgNP, and $Ag@SiO_2$ all exhibit negative surface charge over the pH range investigated, pH 4 to 10. In contrast, APTES-RW showed a transition from negative to positive surface charge at ~ pH 7 with decreasing pH. The positive surface charge of APTES-RW at pH 4 was utilized to electrostatically attach negatively charged AgNPs and $Ag@SiO_2$ NPs to the surface of the pollen.

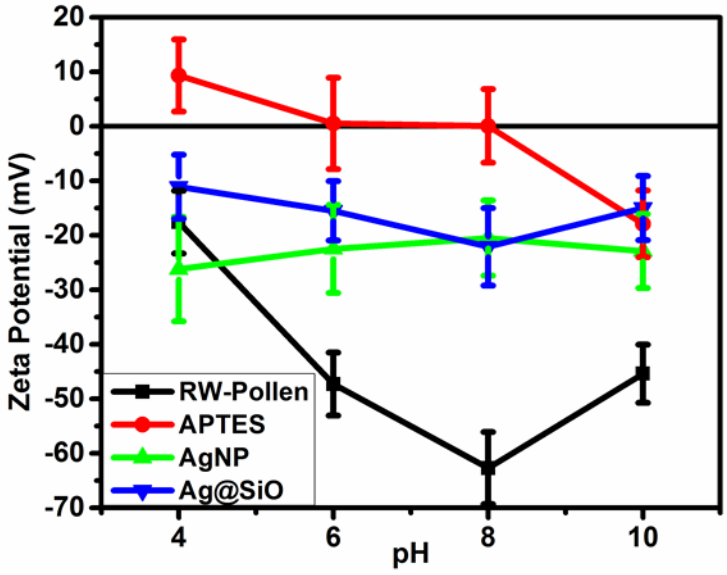

Figure 3.2. Zeta potential measurements of BA-RW, APTES-RW, AgNP, and $Ag@SiO_2$ NP under various pH conditions.

3.2.2 Nanoparticle Coating of Ragweed Pollen

AgNPs were synthesized via the reduction of silver nitrate by ascorbic acid in the presence of trisodium citrate capping agent, see Chapter 1 for more details. In this study AgNPs were 34.1 ± 4.6 nm (averaged over 100 measurements) in diameter, with an absorption maximum of 404 nm shown in Figure 3.3. AgNPs were coated with SiO_2 via a modified Stober method (see Chapter 1).[24] The silica shell is utilized to prevent probe

molecules from selectively binding or adsorbing to the nanoparticle surface, and can be easily functionalized through silane chemistry. This shell, however, must be thin to allow effective transfer of the electromagnetic field from the AgNP core to the probed surface. For this study a 300 µM concentration of TEOS was used to produce a 9.0 ± 1.4 nm thick silica shell. Due to the change in the dielectric environment surrounding the particle, $Ag@SiO_2$ NPs showed a red shifted UV/Vis spectrum compared to the AgNPs shown in Figure 3.3, with an absorption maxima of 425 nm.

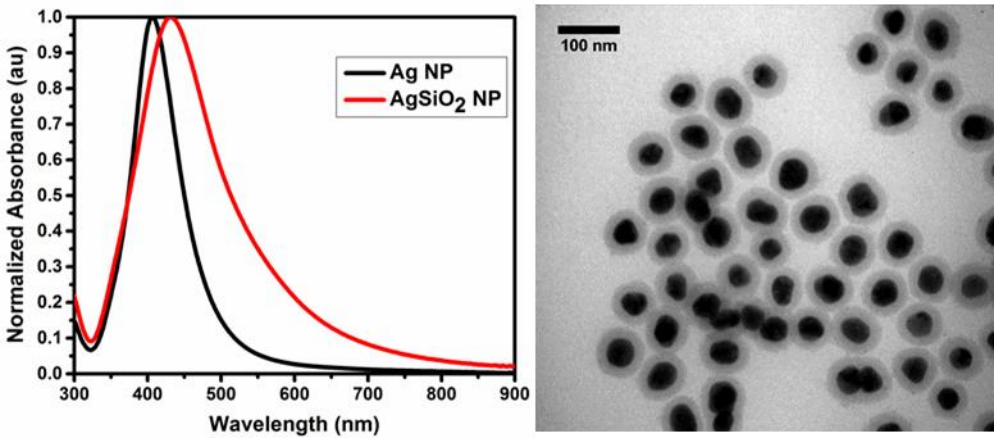

Figure 3.3. UV/Vis spectra of plasmonic absorption of AgNPs and $Ag@SiO_2$ NPs (left), TEM image of $Ag@SiO_2$ NPs (right).

The surface coverage on the APTES-RW was controlled by varying the relative concentrations of the NPs and pollen. The nanoparticle surface coverage was determined by using high-contrast SEM images shown in Figure 3.4. The area of the pollen surface was measured by using ImageJ software. The contrast threshold was adjusted to select the area that was coated by the nanoparticles. The nanoparticle coverage was determined by comparing the NP-coated area to the entire area of the pollen, with averaged measurements derived from 5 different pollens. The NP-RW composites were synthesized by using either

0.7 mL, 1.0 mL or 1.3 mL aliquots of AgNP, which yielded AgNP coverages of 19.7 ± 2.23 %, 53.1 ± 5.54 % and ≈100%. Additionally, for solutions with 1 mL, 3 mL, or 5 mL, aliquots of $AgSiO_2$_NP yielded coverages of 20.6 ± 4.44 %, 53.1 ± 7.22 %, and ≈100%, respectively. For clarity, these samples are referenced as 20%, 55%, and 100% AgNP_RW or $AgSiO_2$_RW.

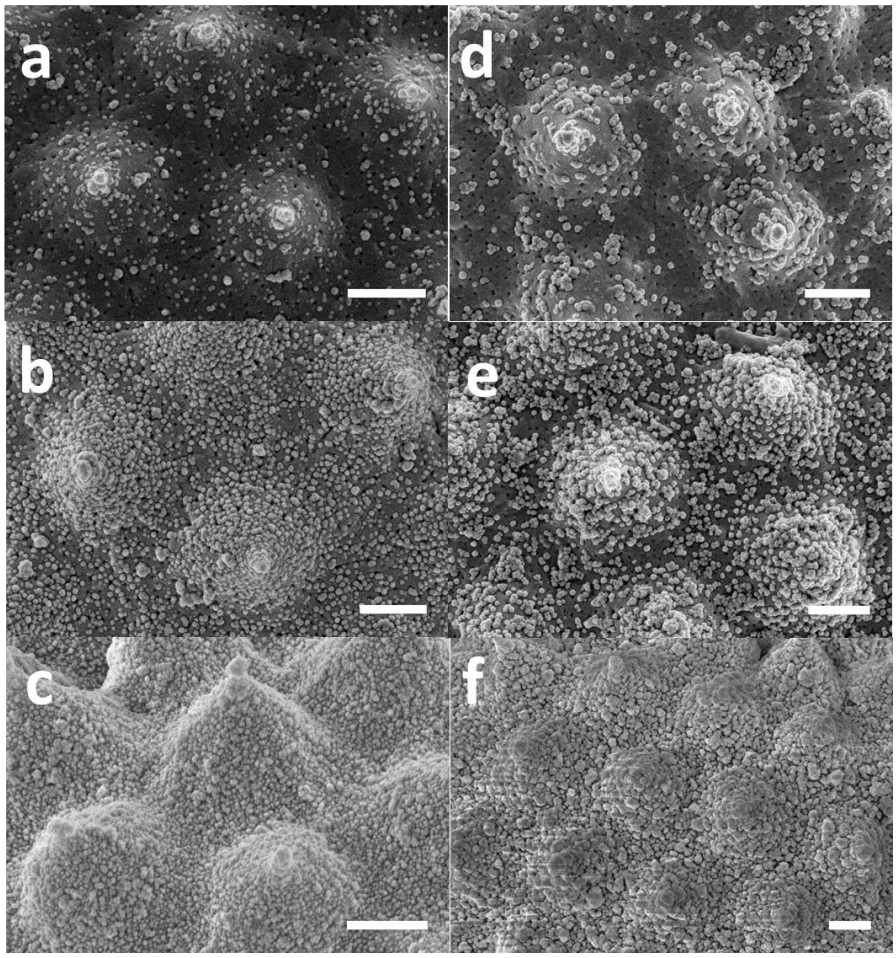

Figure 3.4. SEM images of NP-RW composites with various NP coverages a) 20% AgNP-RW, b) 55% AgNP-RW, c) 100% AgNP-RW, d) 20% Ag@SiO_2 NP-RW, e) 55% Ag@SiO_2 NP-RW, and f) 100% Ag@SiO_2 NP-RW. All Scale bars are 1 micron.

3.2.3 Plasmonic Properties of NP-Pollen Composites

The metallized pollens with AgNP-RW or Ag@SiO_2-RW show a rather strong dependence of the plasmon spectra on the nanoparticle surface density. Nanoparticle aggregation generally leads to interparticle coupling which results in a broadening and red shift in the LSPR.[25] As NP surface density increases the redshift of the plasmon band increase and results in a broadband LSPR activity that extends from ~ 400 nm to beyond 1100 nm (Figure 3.5). The silica coating on the Ag core not only reduces the strength of the LSPR at the surface of the particle but also reduces the interparticle coupling which leads to a reduction in the redshift in the plasmonic resonance of the Ag@SiO_2NP-RW particles as compared to the AgNP-RW (Figure 3.5).

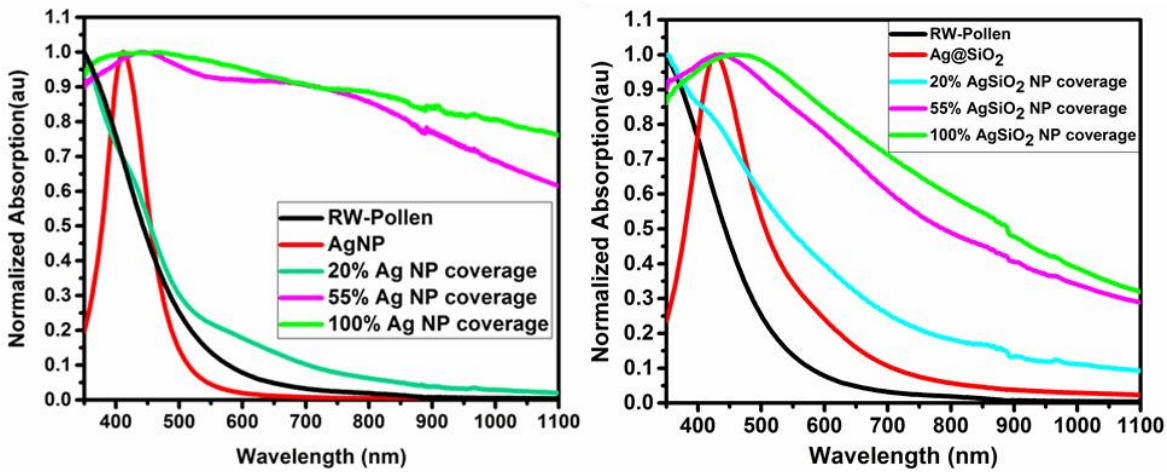

Figure 3.5. Coverage dependence of the LSPR for the AgNP-RW or Ag@SiO_2-RW nanoparticles. Left) Extinction spectra of the AgNP-RW with varying NP coverage; Right) Extinction spectra of the Ag@SiO_2-RW.

3.2.4 Nanoparticle Coated Pollen as a Micro-SERS Platform.

To investigate the potential of NP-RW as microscale SERS substrates, Raman spectra were collected from single particles using a Raman microscope (Figure 3.6). 1, 4-

benzenedithiol (BDT) was used as the probe molecule in this study since it has been well characterized in the literature.[26-27] To evaluate the SERS activity of the AgNP and Ag@SiO_2 NP decorated pollen, the particles were embedded in a solid BDT matrix, BA-RW without NPs were used as a control. Pollen samples were drop cast in a silicone well plate and treated with 20 µL of 0.1 mM BDT solution in EtOH, and the solvent was evaporated on hotplate at 80 ºC to minimize the preferential affinity of the thiol and silver surface. Micro-Raman spectra were collected with an excitation wavelength of 785 nm, with a spot size of 3.14 μm^2, focused directly on the pollen surface. The BA-RW without nanoparticles resulted in no detectable Raman signal. Four characteristic signals of BDT:[26-27] 1555, 1180, 1065, and 729 cm^{-1} were observed in each of the NP-RW spectra. As nanoparticle surface coverage increases from 20% to 100% the SERS signal increased by an order of magnitude (Figure 3.6) due to the increase in strength of the LSPR at the excitation wavelength and the formation of high intensity "hotspots" located in small gaps between nanoparticles. The silica coating on the Ag core not only dampens the strength of the LSPR at the surface of the particle but also reduces the interparticle coupling which leads to a reduction of the LSPR strength at 785 nm and limits the formation of "hotspots", resulting in a peak SERS signal that is ≈50% of their Ag counterparts. Although the enhancement was reduced, the silica coating serves to protect the silver surface from contamination, and provides a surface that can be further functionalized through silane coupling chemistry for the capture or reaction with an analyte of interest.

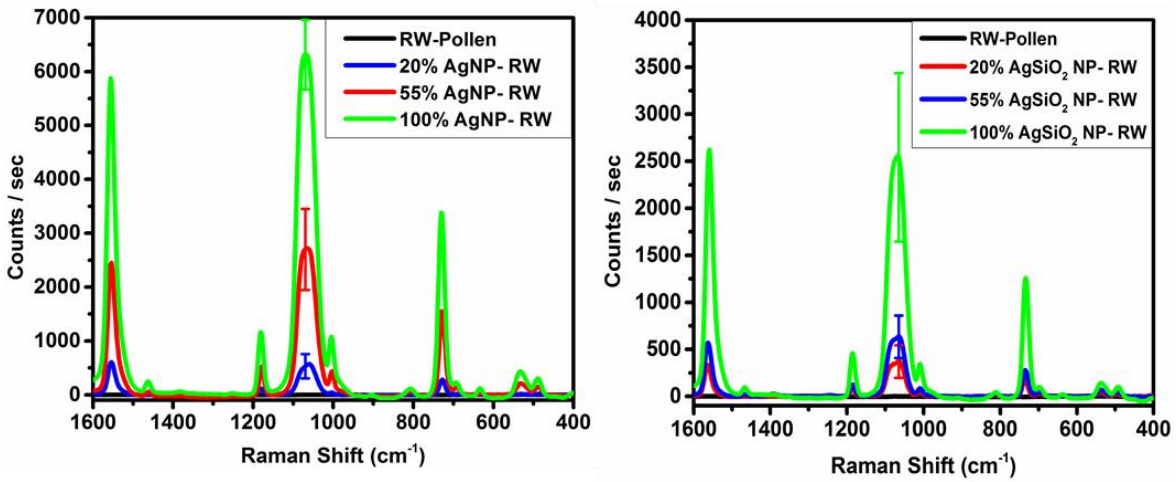

Figure 3.6. Micro-Raman spectra at 785 nm and 1 mW. AgNP-RW (left); Ag@SiO_2 NP-RW (right). The spectra in the figure represent the average of 10 particles.

The peak enhancement factor (EF) of 10^6 was calculated for the 100% AgNP-RW substrate. The normal Raman spectra were collected on a 6μm thin melt processed BDT film and the SERS spectra were collected on a monolayer of BDT on 100% AgNP-RW.

$$EF = \frac{\frac{I_{sers}}{P_{sers}N_{surf}}}{\frac{I_{rs}}{P_{rs}N_{vol}}} = \frac{\frac{I_{sers}}{P_{sers}\mu_m\mu_s A_M}}{\frac{I_{rs}}{P_{rs}N_{vol}}} \quad (6)$$

The enhancement factor was calculated using (Equation 6), where I_{sers}/P_{sers} and I_{rs}/P_{rs} are the intensity and power of the SERS and normal Raman spectra respectively, N_{surf} is the number of adsorbed molecules on the surface of SERS substrate, N_{vol} is the number of molecules in the normal Raman excitation volume, μ_m is the number of nanostructures on the substrate, A_m is the surface area of the nanostructure, and μ_s is the surface density of molecules on the surface.[28] The EF was calculated with an estimated molecular footprint of 0.19 nm^2 and a density of 1 g/cm^3.

To investigate the potential of the NP-RW as bulk SERS substrates, the particles were dispersed in a solid BDT matrix and Raman spectra were collected using a FT-Raman spectrometer. APTES-RW without NPs showed no detectable BDT Raman signal at 10 mW at 1064 nm. The AgNP-RW showed strong SERS activity (Figure 3.7) that is relatively independent of NP coverage. The 75% Ag@SiO_2-RW and 25% Ag@SiO_2-RW show an 80% and 60% reduction in their SERS signal, respectively, compared to their AgNP-RW counterparts. As mentioned previously, the silica shell isolates the NPs from one another resulting in reduced interparticle coupling that lowers the LSPR at 1064 nm. The aggregation of NP that occurs during the coating process makes the NP-RW an effective broadband (785-1064 nm) SERS substrate platform, which can be utilized as a single particle or bulk sensor.

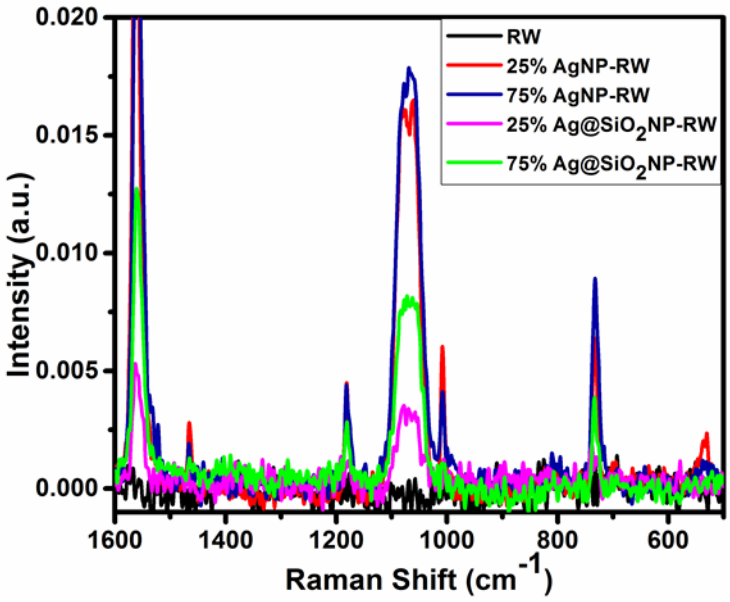

Figure 3.7. FT-Raman spectra at 1064 nm (10 mW), of NP-RW embedded in BDT matrix.

3.2.5 Two-Photon Excited Fluorescence of Nanoparticle Pollens

The two-photon excited fluorescence (excitation wavelength, 790 nm) images of the pollen exine, the 100% AgNP-RW, and the 100% Ag@SiO_2 NP particles are shown in Figure 3.8. The pollen exine produced measureable but weak fluorescence, whereas the 100% AgNP-RW showed comparatively strong two-photon excited fluorescence emission, as expected due to the presence of the aggregated AgNPs. The RW_100% Ag@SiO_2 NP showed diminished two-photon fluorescence relative to their AgNP counterparts, due to the reduced intensity of the hotspots due to the SiO_2 coating of the AgNP. The 2-photon fluorescence provides a secondary mode of detection in addition to the SERS activity.

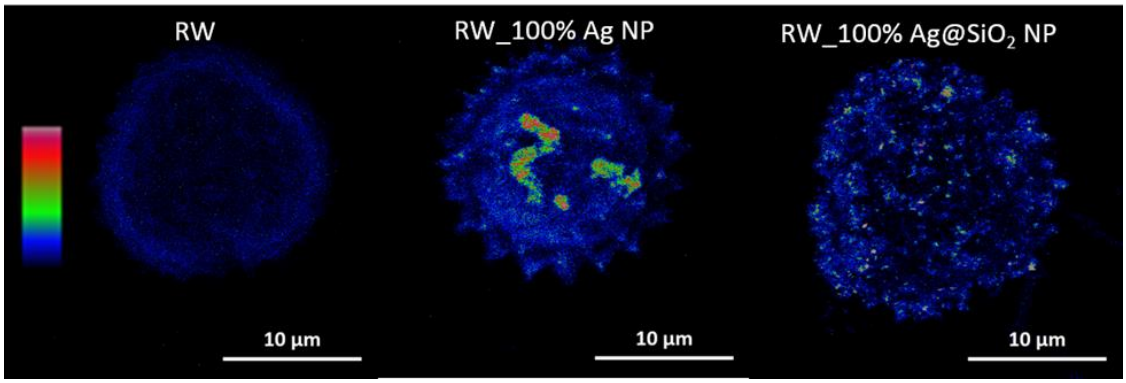

Figure 3.8. Two-photon excited fluorescence images of RW and nanoparticle coated RW pollens.

3.2.6 Adhesion Enhancements of Nanoparticle Pollens

Two different substrates were used to examine the effect of surface chemistry on the adhesion forces of each pollen particle. Polystyrene (PS) was chosen as a model hydrophobic polymer substrate, with water static contact angle $\theta_w \approx 104^o$, while piranha-etched silicon (Si) was used as a model inorganic, hydrophilic, and protic surface with $\theta_w \approx 14^o$. Both substrate surfaces are relatively smooth with both the mean (R_a) and root-mean-square (*rms*) surface roughness of ~0.3 and 2.0 nm for Si and PS respectively, which

were obtained from topography scans of three randomly-chosen 10 μm × 10 μm areas on each substrate surface by using atomic force microscopy.

Contact mode AFM force measurements were used to evaluate the short-range adhesion of six different NP-RW with varied NP surface coverage to the Si and PS substrates. The average values of the adhesion forces for each particle and substrate combination are shown in Figure 3.9. Note that each average value was obtained from 40 measurements consisting of 10 analyses for each of four similar particle/cantilever probes. Since the scale of pollen particle surface micro-topography is relatively larger than the surface roughness of Si and PS substrates (0.3 and 2.0 nm respectively), the effect of these small differences in roughness are likely to be negligible. For cleaned ragweed pollen particles (BA-RW), it was demonstrated previously that the adhesion forces on Si and PS substrates were governed by van der Waals (VDW) interactions.[21] Thus, no appreciable differences were observed in the adhesion forces of BA-RW on Si and PS surfaces. In contrast, for AgNP-RW or Ag@SiO_2NP-RW, the adhesion forces were dependent on substrate composition, and the force was stronger on Si than PS. Furthermore, an appreciable enhancement of the adhesion force was observed with increasing NP surface coverage for AgNP-RW and Ag@SiO_2 NP-RW. The average adhesion force values for 100% AgNP-RW and Ag@SiO_2NP-RW were 25% higher on PS and 100% higher on Si, as compared to BA-RW.

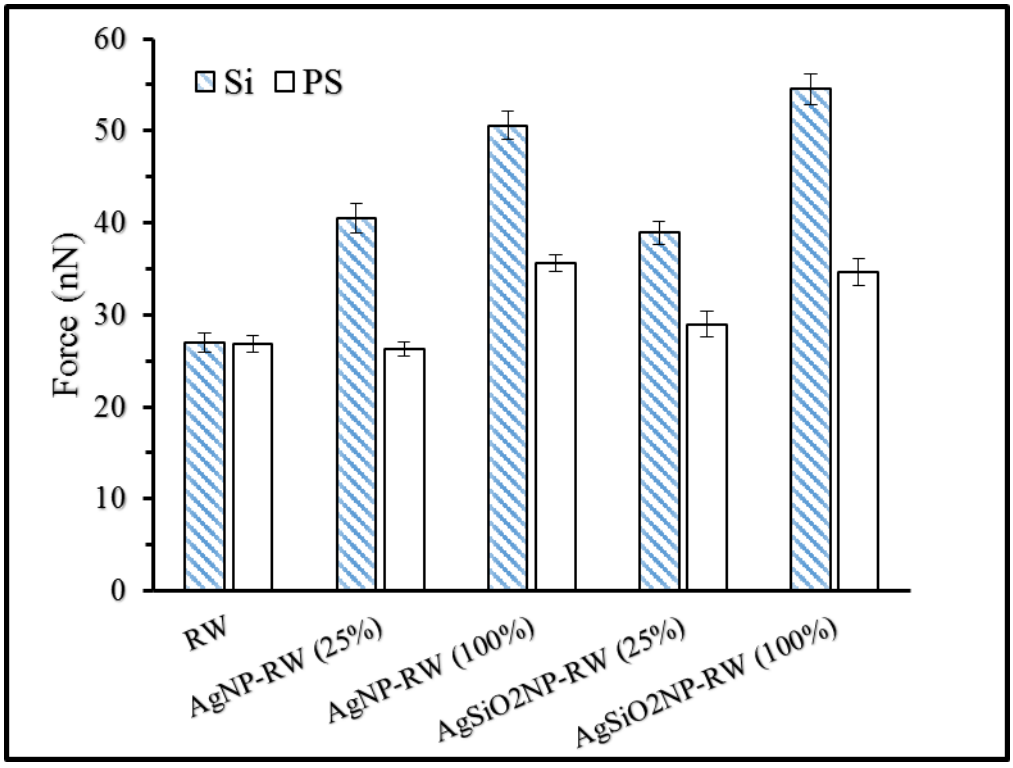

Figure 3.9. Adhesion data for various NP coated pollens on silicon and polystyrene. NP coverage given in parenthesis.

Typically, the adhesion forces of particles on a substrate can be controlled and tuned by the surface morphology and chemistry, feature size and coating materials. In this study, the short-range adhesion on the PS substrate is expected to be governed by the VDW force. Therefore, the dependence of VDW based-adhesion on the pollen ornamentations should be approximated well by the Hamaker equation (Equation 2) of the sphere-plane model:[29]

$$F_{VDW} = \frac{A_{123}R}{6D^2} \tag{7}$$

where, A_{132} is the non-retarded Hamaker constant of material 1 and 2 interacting across a medium 3 (air), R is the contact radius, and D is the cutoff separation distance for the VDW

interaction (≈0.165 nm). With the assumption that $A_{33} = 0$, A_{132} can be approximated with Equation 3.

$$A_{123} = \sqrt{A_{11}A_{22}} \tag{8}$$

Thus, A_{132} values for ragweed pollen particles coated with AgNPs and Ag@SiO_2NPs on both Si and PS substrates (Table 3) were calculated from Equation 2 using Hamaker constants of Ag, SiO_2 and PS available in the literature (40×10^{-20}, 6.3×10^{-20}, and 6.5×10^{-20} J, respectively).[29] Approximate A_{132} values for BA-RW on the Si and PS substrates were calculated from appropriate A_{11} and A_{22} values available in the literature.[21,29] Therefore, according to Equation 1 using the measured average values of adhesion force, along with the calculated A_{132} constants, the predicted values of contact radii for each pollen particle with varied coatings on the PS surface were calculated (Table 3) to be ~52 nm (BA-RW), ~27-36 nm (AgNP-RW), ~74-89 nm (Ag@SiO_2 NP-RW), respectively. For the BA-RW, the calculated contact radius (52 ± 1 nm), similar to the average spine tip radius (52 ± 5 nm) obtained from SEM analysis; that is consistent with a previous report that the VDW-based adhesion force for this pollen particle was a single spine tip contact to a given substrate.[21] However, the calculated contact radii for the AgNP-RW (~27-35 nm), and Ag@SiO_2NP-RW (~74-89 nm) were significantly smaller than the average spine tip radii of these particles (80 ± 17 and 100 ± 20 nm for AgNP-RW, and Ag@SiO_2 NP-RW, respectively) measured by SEM analyses. Instead, the calculated contact radii for these pollen particles were in good agreement with the average NP crystallite size (35-40 nm for AgNP, and 45-50 nm for Ag@SiO_2 NP) of these particles obtained from TEM analyses. These results indicated that VDW-based adhesion forces of

the pollen with NP coatings were consistent with the contact between one or two NPs located at the end of spine tips with the substrates.

Table 3. Average Measured Values of Adhesion Force (F_{tot}, in nN), Calculated Hamaker Constants (A_{132}, × 10^{-20} J), Calculated Contact Radii (R, in nm), Calculated VDW Force (F_{vdw}, in nN), and Calculated non-VDW Force (F_{nvdw}, in nN).

		RW	AgNP-RW (25%)	AgNP-RW (100%)	Ag@SiO_2 NP-RW (25%)	Ag@SiO_2 NP-RW (100%)
PS	A_{132}	8.4	16	16	6.4	6.4
	F_{tot}	27 ± 1	26 ± 1	35 ± 1	29 ± 1	35 ± 2
	R	52	27	35	74	89
Si	A_{132}	8.5	16	16	6.3	6.3
	F_{tot}	27 ± 1	40 ± 2	51 ± 2	39 ± 1	55 ± 2
	F_{vdw}	27 ± 1	27 ± 2	34 ± 2	28 ± 1	34 ± 2
	F_{nvdw}	0	13 ± 2	17 ± 2	11 ± 1	21 ± 2

Comparing the adhesion forces of NP-RW particles on Si and PS substrates, it is clear that the hydrophilic Si surface exhibited appreciably stronger adhesion to NP-RW. This is attributed to the additional plausible non-VDW interactions (F_{nvdw}), for example, the hydrogen bonding interactions between the oxygen and hydroxyl functional groups of the Si substrate and NP surfaces. Since both substrates are relatively flat and smooth, the contact radii R of those particles on the Si substrate are considered as the same as those on PS substrate. Then, the VDW-based adhesion force, F_{vdw}, for those pollen particles on the Si surface can be back calculated by using (Equation 2) with the calculated A_{132} constants and radii R, as listed in **(**Table 3**)**. Furthermore, the non-VDW forces were obtained by $F_{nvdw} = F_{tot} - F_{vdw}$, where F_{tot} is the experimentally measured force as shown in (Table 3),

this F_{nvdw} is also dependent on both the contact radii R and properties of the NP materials. Pollen particles with higher coverage of AgNP and Ag@SiO_2NP exhibited higher adhesion forces for both VDW and non-VDW interactions on Si substrates as compared to PS. The adhesion forces of pollen with similar coverages of AgNP and Ag@SiO_2NP were comparable, even though the latter showed much higher contact radii (27-35 *vs* 74-89 nm). This is attributed to the much higher Hamaker constant of AgNP compared to Ag@SiO_2 NP (40×10^{-20} and 6.3×10^{-20} J, respectively).

3.3 Conclusion

In this chapter we have demonstrated the ability to coat RW-pollen exine with nanoparticles with precise control over the nanoparticle average surface coverage. Negatively charged nanoparticles were immobilized on the surface through electrostatic attraction to create an adhesive SERS substrate. Strong Raman signals have been realized from AgNP and Ag@SiO_2NP coated pollens dispersed in a BDT matrix, with broadband NIR (785-1064 nm) LSPR response. In addition to SERS activity, the adhesive NP-pollen micro-particles display tunable VDW and non-VDW forces (i.e. hydrogen bonding). The adhesion forces were found to exhibit short-range (<5 nm) VDW-based and non-VDW adhesion governed by the NP size and composition at the pollen tip. A maximum of 100% increase of the adhesion force for Ag@SiO_2NP-pollen on a Si substrate was realized. Two-photon excited fluorescence measurements demonstrate the multimodal detection ability of composite particles through both SERS and two-photon confocal microscopy. This work demonstrates the tailoring of the adhesive properties of nanoparticle coated pollen exine structures enabled by the spiky pollen morphology, and the composition of the NP-pollen constructs and the nature of the substrate. These adhesive NP-pollen construct also exhibit

strong SERS activity with broadband NIR (785-1064) LSPR. The development of biologically derived micro-particles with large surface area to volume ratio, strong optical signatures and enhanced adhesion properties can have applications in security features, bio-sensing, and chemical agent detection.

3.4 Experimental Details

3.4.1 Materials

Native defatted ragweed (Ambrosia artemisiifolia, RW) pollen grains (Greer Laboratories), silver nitrate (99.99999% trace metal basis), L-ascorbic acid (≥99.0%), sodium citrate, and toluene, were purchased from Sigma-Aldrich, dimethylamine (DMA, 40%w/w, Alfa Aesar) aqueous solution, (3-aminopropyl)-triethoxysilane (APTES, Gelest Inc.), tetraethoxysilane (TEOS, 99.0+%, Gelest Inc.), potassium hydroxide (6 w/v%, EDM Millipore), orthophosphoric acid (85%, EDM Millipore), sulfuric acid (97% purity, BDH Chemicals Ltd.), hydrogen peroxide (30 wt %, BDH Chemicals Ltd), polystyrene (MW = 100,000 g/mol, Avocado Research Chemicals), AFM cantilever (FORT-TL, Applied NanoStructures), Si substrates (Silicon, Inc.), silicone well-plates (Gace Bio-Labs) and epoxy resin (Epoxy Marine, Loctite) were used as received. Deionized water (DIW, 18.2 MΩ cm, pH 6.4) was prepared with a Barnstead E-Pure purification system.

3.4.2 Ag Nanoparticle Synthesis

Quasi-spherical silver nanoparticles were synthesized via a previously reported method.[30] In short, 12.5 mL ascorbic acid (4.8 mM), 8.825 mL sodium citrate (1 w/w%), were added to 80 mL DIW. The reaction mixture is adjusted to pH 9.5 with 0.1 M citric

acid and 0.1 M NaOH. The solution was placed in 30°C hot bath, and 1 mL aqueous solution of $AgNO_3$ (0.1 M) was injected into the reaction mixture and stirred at 1200 RPM for 15 min. The contents of the reaction flask were then transferred to an oil bath at 100°C for 30 min without stirring and then placed in ice bath to quench the reaction.

3.4.3 Ag@SiO_2 Nanoparticle Synthesis

The silica coating of Ag nanoparticles was performed using a modified procedure from previous reports.[24,31] 2.0 mL of AgNP, filtered through 0.8 µm Nylon filter to remove large or aggregated nanoparticles, were added to 20 mL of 95/5% ethanol water mixture in a 50 mL centrifuge tube. 600-1200 µL TEOS (10 mM in ethanol) were added and then followed by the addition of 200 µL DMA. The reaction mixture was then shaken with vortex mixer for 2 hrs. Ag@SiO_2 NP were collected using a centrifuge operating at 8000 RPM for 15 minutes. The resultant Ag@SiO_2 NP were washed 3 times each with ethanol and water, and then dispersed in 2 mL of ethanol.

3.4.4 Pollen Preparation

A sequential base/acid treatment was used to remove organic pollen kit from pollen exine.[21] A 10 g batch of defatted RW was added to a 100 mL of potassium hydroxide (6 w/v %) solution for 6 hrs at room temperature. The basic solution was neutralized using HCl, centrifuged and washed with boiling DIW, and boiling ethanol three times, respectively. The pollen was then dried in a convection oven at 60 °C for 2 days. Dried base-treated pollens were then added to 200 mL of orthophosphoric acid at 50 °C for 7 days. The acidic solution was neutralized with NaOH and centrifuged and washed 3 times

each with boiling DIW, boiling acetone, and boiling ethanol. The base/acid treated pollen (BA-RW) were then dried in vacuum oven at 60 °C for 24 hrs.

BA-RW were then treated with APTES. 80 mg of BA-RW were dispersed in 70 mL of anhydrous toluene and sealed in a round bottom flask. 2.0 mL of APTES was added and the mixture was stirred for 24 hrs under nitrogen in a hot bath at 85 °C. The APTES treated pollens (APTES-RW) were then washed 3 times each with toluene, n-hexane, and ethanol, respectively. APTES-RW were then dispersed in 3 mL of ethanol.

3.4.5 NP-Pollen Composites

0.7-5.0 mL of AgNP or Ag@SiO_2 NP were diluted with DIW to a total volume of 5.0 mL. The solution was then adjusted to a pH of 4 using 0.1 M citric acid and NaOH. 10 µL of APTES-RW pollen was added to a NP solution and agitated with a nutating mixer overnight. The NP-RW were then washed 3 times with DIW and stored in DIW. For Raman measurements, pollens were drop-casted into 2 mm diameter silicone wells of a silicone well plate and allowed to dry under ambient conditions. Then, two sequential treatments with 5 µL of BDT (0.1 mM in EtOH) were drop casted and the solvent was evaporated on a hotplate at 80 ^oC.

3.4.6 Adhesion Measurements

The adhesion forces were measured using atomic force microscopy (AFM, Veeco Dimension 3100) under ambient conditions (21^oC, relative humidity 38-40%) using an AFM colloidal probe technique.[32] Tipless rectangular cantilevers with nominal spring constants of 0.6−3.7 N/m (Applied NanoStructures, Inc., Santa Clara, CA) were used.

Single pollen particles were glued to the tipless cantilevers with a small amount of epoxy resin using a procedure described in detail elsewhere.[21] Si substrates were piranha-etched by sulfuric acid/hydrogen peroxide (3:1) mixture at 80 °C for 4 hrs. A PS thin film was blade cast on a Si wafer from a PS solution (10 wt% in toluene). The actual spring constants for the cantilevers with the attached pollen particles were determined directly by the methods of Burnham and Hutter et al.[33,34] A series of 10 force-distance curves were measured for each combination of pollen tip and substrate surface. The measurements were performed on three separate substrate surfaces with randomly chosen areas on each substrate. For each pollen particle sample, four separate AFM tips with a bound pollen were measured with a low applied load 2.5 nN for all force measurements. No obvious damage or deformation of pollen tips was observed by SEM imaging taken after all the force measurements.

3.4.7 Particle Characterization

AgNP and Ag@SiO_2 NP were drop-casted on carbon coated copper TEM grids (Electron Microscopy Science). TEM images were collected on a JEOL 100CX II TEM with a 100 keV accelerating voltage. Zeta potential measurements were obtained with a Malvern Zetasizer Nano-ZS. NP-RW composites were drop-casted on copper tape mounted on a SEM stub, and images were collected with a ZEISS ULTRA 60 FE SEM. Micro-Raman spectra were collected with a Thermo Nicolet Almega XR Dispersive Raman Spectrometer with an excitation wavelength of 785 nm and power of 1.0 mW. A long working distance 50X objective was used to focus the laser on the pollen specimen, and the scattered light was collected using a backscattering geometry. 10 scans were averaged for each spectrum. Bulk-Raman spectra were collected with a Bruker MultiRAM

FT-Spectrometer, equipped with a Nd:YAG laser with a excitation wavelength of 1064 nm and power of 10 mW. Two-photon excited fluorescence images were collected with a Zeiss LSM780 with a 63x oil immersion objective, an excitation wavelength of 790 nm, a power of 0.56 ± 0.1 mW, signal collection over 415-740 nm, gain of 700, X-Y resolution of 26.9 x 26.9 µm (0.05 µm/pixel), and a Z-resolution of 0.8 µm/layer. All samples were dispersed in immersion oil to reduce scattering and sandwiched between two coverslips.

3.5 REFERENCES

1. Kneipp, K.; Kneipp, H.; Itzkan, I.; Dasari, R. R.; Feld, M. S., Ultrasensitive Chemical Analysis by Raman Spectroscopy. *Chemical Reviews* **1999,** *99* (10), 2957-2976.

2. Kneipp, K.; Wang, Y.; Kneipp, H.; Perelman, L. T.; Itzkan, I.; Dasari, R. R.; Feld, M. S., Single Molecule Detection Using Surface-Enhanced Raman Scattering (SERS). *Physical Review Letters* **1997,** *78* (9), 1667-1670.

3. Wu, D.-Y.; Li, J.-F.; Ren, B.; Tian, Z.-Q., Electrochemical surface-enhanced Raman spectroscopy of nanostructures. *Chemical Society Reviews* **2008,** *37* (5), 1025-1041.

4. Qian, X.; Peng, X.-H.; Ansari, D. O.; Yin-Goen, Q.; Chen, G. Z.; Shin, D. M.; Yang, L.; Young, A. N.; Wang, M. D.; Nie, S., In vivo tumor targeting and spectroscopic detection with surface-enhanced Raman nanoparticle tags. *Nat Biotech* **2008,** *26* (1), 83-90.

5. Qin, L.; Zou, S.; Xue, C.; Atkinson, A.; Schatz, G. C.; Mirkin, C. A., Designing, fabricating, and imaging Raman hot spots. *Proceedings of the National Academy of Sciences* **2006,** *103* (36), 13300-13303.

6. Kelly, K. L.; Coronado, E.; Zhao, L. L.; Schatz, G. C., The Optical Properties of Metal Nanoparticles: The Influence of Size, Shape, and Dielectric Environment. *The Journal of Physical Chemistry B* **2003,** *107* (3), 668-677.

7. Gordon, R.; Sinton, D.; Kavanagh, K. L.; Brolo, A. G., A New Generation of Sensors Based on Extraordinary Optical Transmission. *Accounts of Chemical Research* **2008,** *41* (8), 1049-1057.

8. Gunnarsson, L.; Bjerneld, E. J.; Xu, H.; Petronis, S.; Kasemo, B.; Käll, M., Interparticle coupling effects in nanofabricated substrates for surface-enhanced Raman scattering. *Applied Physics Letters* **2001,** *78* (6), 802-804.

9. Kuncicky, D. M.; Prevo, B. G.; Velev, O. D., Controlled assembly of SERS substrates templated by colloidal crystal films. *Journal of Materials Chemistry* **2006,** *16* (13), 1207-1211.

10. Tang, J.; Guo, H.; Chen, M.; Yang, J.; Tsoukalas, D.; Zhang, B.; Liu, J.; Xue, C.; Zhang, W., Wrinkled Ag nanostructured gratings towards single molecule detection by ultrahigh surface Raman scattering enhancement. *Sensors and Actuators B: Chemical* **2015,** *218*, 145-151.

11. Jeon, T. Y.; Park, S.-G.; Kim, D.-H.; Kim, S.-H., Standing-Wave-Assisted Creation of Nanopillar Arrays with Vertically Integrated Nanogaps for SERS-Active Substrates. *Advanced Functional Materials* **2015,** *25* (29), 4681-4688.

12. Köhler, J. M.; März, A.; Popp, J.; Knauer, A.; Kraus, I.; Faerber, J.; Serra, C., Polyacrylamid/Silver Composite Particles Produced via Microfluidic Photopolymerization for Single Particle-Based SERS Microsensorics. *Analytical Chemistry* **2013,** *85* (1), 313-318.

13. Deng, Z.; Chen, M.; Wu, L., Novel Method to Fabricate SiO2/Ag Composite Spheres and Their Catalytic, Surface-Enhanced Raman Scattering Properties. *The Journal of Physical Chemistry C* **2007,** *111* (31), 11692-11698.

14. Guo, I. W.; Pekcevik, I. C.; Wang, M. C. P.; Pilapil, B. K.; Gates, B. D., Colloidal core-shell materials with 'spiky' surfaces assembled from gold nanorods. *Chemical Communications* **2014,** *50* (60), 8157-8160.

15. Mosier-Boss, P. A.; Lieberman, S. H., Surface-Enhanced Raman Spectroscopy Substrate Composed of Chemically Modified Gold Colloid Particles Immobilized on Magnetic Microparticles. *Analytical Chemistry* **2005,** *77* (4), 1031-1037.

16. Zhang, J.; Liu, J.; Wang, S.; Zhan, P.; Wang, Z.; Ming, N., Facile Methods to Coat Polystyrene and Silica Colloids with Metal. *Advanced Functional Materials* **2004,** *14* (11), 1089-1096.

17. Shi, W.; Sahoo, Y.; Swihart, M. T.; Prasad, P. N., Gold Nanoshells on Polystyrene Cores for Control of Surface Plasmon Resonance. *Langmuir* **2005,** *21* (4), 1610-1617.

18. Lee, J.-H.; Mahmoud, M. A.; Sitterle, V.; Sitterle, J.; Meredith, J. C., Facile Preparation of Highly-Scattering Metal Nanoparticle-Coated Polymer Microbeads and Their Surface Plasmon Resonance. *Journal of the American Chemical Society* **2009,** *131* (14), 5048-5049.

19. Smith, A. M.; Mancini, M. C.; Nie, S., Bioimaging: Second window for in vivo imaging. *Nat Nano* **2009,** *4* (11), 710-711.

20. Joseph, V.; Schulte, F.; Rooch, H.; Feldmann, I.; Dorfel, I.; Osterle, W.; Panne, U.; Kneipp, J., Surface-enhanced Raman scattering with silver nanostructures generated in situ

in a sporopollenin biopolymer matrix. *Chemical Communications* **2011,** *47* (11), 3236-3238.

21. Lin, H.; Gomez, I.; Meredith, J. C., Pollenkitt Wetting Mechanism Enables Species-Specific Tunable Pollen Adhesion. *Langmuir* **2013,** *29* (9), 3012-3023.

22. Lin, H.; Lizarraga, L.; Bottomley, L. A.; Carson Meredith, J., Effect of water absorption on pollen adhesion. *Journal of Colloid and Interface Science* **2015,** *442*, 133-139.

23. Kiselev, D.; Bonacina, L.; Wolf, J.-P., Individual bioaerosol particle discrimination by multi-photon excited fluorescence. *Opt. Express* **2011,** *19* (24), 24516-24521.

24. Kobayashi, Y.; Katakami, H.; Mine, E.; Nagao, D.; Konno, M.; Liz-Marzán, L. M., Silica coating of silver nanoparticles using a modified Stöber method. *Journal of Colloid and Interface Science* **2005,** *283* (2), 392-396.

25. Ghosh, S. K.; Pal, T., Interparticle Coupling Effect on the Surface Plasmon Resonance of Gold Nanoparticles: From Theory to Applications. *Chemical Reviews* **2007,** *107* (11), 4797-4862.

26. Cho, S. H.; Han, H. S.; Jang, D.-J.; Kim, K.; Kim, M. S., Raman Spectroscopic Study of 1,4-Benzenedithiol Adsorbed on Silver. *The Journal of Physical Chemistry* **1995,** *99* (26), 10594-10599.

27. Joo, S. W.; Han, S. W.; Kim, K., Adsorption of 1,4-Benzenedithiol on Gold and Silver Surfaces: Surface-Enhanced Raman Scattering Study. *Journal of Colloid and Interface Science* **2001,** *240* (2), 391-399.

28. Le Ru, E. C.; Blackie, E.; Meyer, M.; Etchegoin, P. G., Surface Enhanced Raman Scattering Enhancement Factors: A Comprehensive Study. *The Journal of Physical Chemistry C* **2007,** *111* (37), 13794-13803.

29. Israelachvili, *Intermolecular and Surface Forces*. Acadamic Press: London, 1992.

30. Qin, Y.; Ji, X.; Jing, J.; Liu, H.; Wu, H.; Yang, W., Size control over spherical silver nanoparticles by ascorbic acid reduction. *Colloids and Surfaces A: Physicochemical and Engineering Aspects* **2010,** *372* (1–3), 172-176.

31. Liu, S.; Zhang, Z.; Han, M., Gram-Scale Synthesis and Biofunctionalization of Silica-Coated Silver Nanoparticles for Fast Colorimetric DNA Detection. *Analytical Chemistry* **2005,** *77* (8), 2595-2600.

32. Ducker, W. A.; Senden, T. J.; Pashley, R. M., Direct measurement of colloidal forces using an atomic force microscope. *Nature* **1991,** *353* (6341), 239-241.

33. Burnham, N. A.; Chen, X.; Hodges, C. S.; Matei, G. A.; Thoreson, E. J.; Roberts, C. J.; Davies, M. C.; Tendler, S. J. B., Comparison of calibration methods for atomic-force microscopy cantilevers. *Nanotechnology* **2003,** *14* (1), 1.

34. Hutter, J. L.; Bechhoefer, J., Calibration of atomic-force microscope tips. *Review of Scientific Instruments* **1993,** *64* (7), 1868-1873.

CHAPTER 4. PLASMONIC SILVER AND SILICA COATED SILVER NANOPARTICLE DOPED P3HT:PCBM PHOTOVOLTAICS

4.1 Introduction

Plasmonic metal nanoparticles have been incorporated into OPV devices to increase absorption and efficiency, a detailed review of plasmonic OPVs can be found in section 1.4. Several different variables have been studied such as shape,[1] plasmon frequency,[2] location in device,[3] material,[4] or device geometry[5] among others. In addition to the using colloidal metal NP other more complex lithographic structure have been produced,[6] 2-D "fishnet" structures,[7] hole arrays,[8] and others.[9] These advanced techniques can create a near infinite variety of structures and can be used to precisely tailor the resulting plasmonic resonance. These techniques are extremely expensive in terms of equipment and time required compared to colloidal metal nanoparticles. Additionally, they are not scalable for roll-to-roll processing required for implementation in OPV applications.

Often in these plasmonic OPV studies, the focus is on utilizing a particular nano-material, optimizing its incorporation in OPV device, and maximizing the J-V characteristics of the device. Considerably less effort has been placed on understanding of the interactions occurring within the material. It has been demonstrated that light scattering and field enhancements can cause increases in light absorption in PSCs,[10] there has been some reports attributing the effects of nanoparticle addition to electrical enhancements.[11-12] It is clear that these type of optical enhancements can be achieved, but I also believe that

not all J_{SC} increases ascribed to the optical effects have been unquestionably elucidated. In this work, plasmonic enhancements are investigated through electrical characterization, and the plasmonic devices are also probed with transient absorption spectroscopy. With transient absorption spectroscopy, the exciton and polaron absorption and decay dynamics are probed directly to further understand their interaction with metal nanoparticles.

4.2 Results and Discussion

4.2.1 Synthesis and Functionalization of Silica Coated Nanoparticles

AgNPs were synthesized via the reduction of silver nitrate by ascorbic acid in the presence of trisodium citrate capping agent, see Section 2.2.1 for more details. The AgNPs used in this study were synthesized at a pH of 9.5, the resultant particles are 32.3 ± 5.3 nm (averaged over 100 measurements) in diameter, with an absorption maximum of 430 nm shown in Figure 4.1. AgNPs were coated with SiO_2 via a modified Stober method developed in Chapter 2.[13] The silica shell provides electrical insulation to prevent exciton and charge carrier quenching in composite OPV devices.[14-15] This shell, however, must be thin to allow effective transfer of the electromagnetic field from the AgNP core to polymer matrix.[16-17] Here, 700 µl of TEOS was used to produce a 5.34 ± 0.5 nm thick silica shell. Due to the change in the dielectric environment surrounding the particle, Ag@SiO_2 NPs showed a red shifted UV/Vis spectrum compared to the AgNPs shown in Figure 4.1, with an absorption maximum of 440 nm.

The incorporation of $AgSiO_2$ NPs into the P3HT:PCBM photoactive layer requires a well dispersed colloid in a chlorinated solvent. Due to the lack of electrostatic interactions in organic media, it is difficult to synthesis metal NPs in organics larger than 20 nm.[18-19]

Additionally, attempts to phase transfer larger nanoparticles often result in aggregation and reproducibility concerns.[20-21] The ease of functionalization and phase transfer is one of Ag@SiO_2 NP most attractive features. Phase transfer of the $AgSiO_2$ NP can be achieved via surface functionalization with hydrophobic moieties. Alkoxy-silanes can be grafted to hydroxyl group on the nanoparticle surface at elevated temperatures, in toluene,[22] or though base catalyzed hydrolysis and condensation.[23] To minimize silica overgrowth and maintain $AgSiO_2$ NP morphology, the surface grafting technique was utilized to achieve monolayer functionalization with octyl-triethoxysilane. After functionalization and washing, the octyl-$AgSiO_2$ NP were dispersed in DCB for incorporation in polymer blends. The LSPR absorption of octyl-$AgSiO_2$ (Figure 4.1) show a red shift in absorption due to the change of refractive index upon transfer to DCB from EtOH. Conformation of successful functionalization can be seen in the IR spectra, shown in Figure 4.2, where the characteristic Si-O-Si peak (1000-1100 cm^{-1}) can be seen in both spectra and the C-C stretches (1400-1600 cm^{-1}) and C-H (≈2900 cm^{-1}) from the octyl group functionalization are evident.

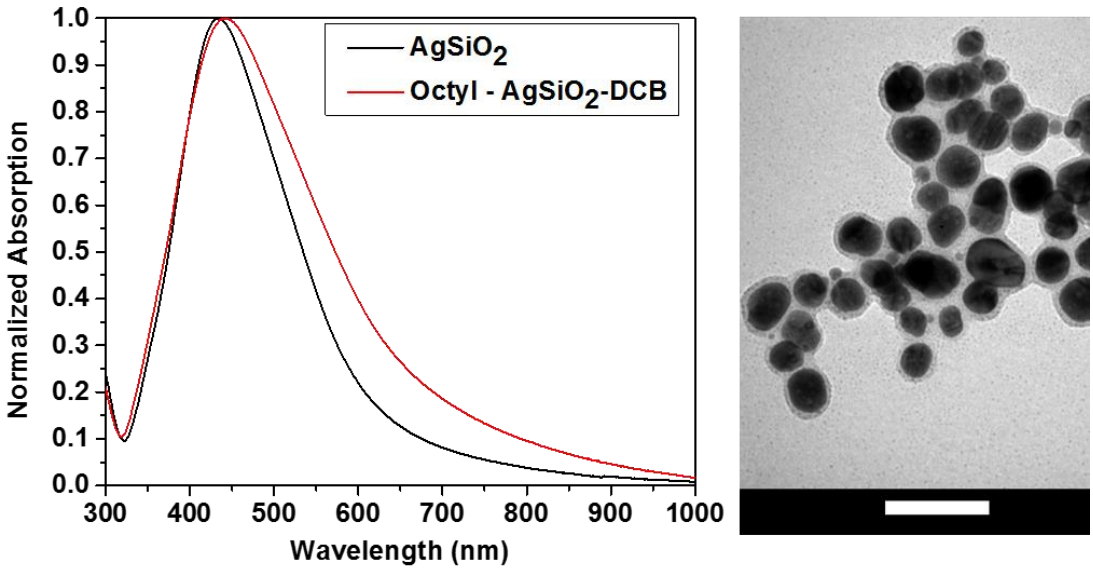

Figure 4.1. UV/Vis absorption of Ag and $AgSiO_2$ NP LSPR. (left) TEM image of $AgSiO_2$ NP after octyl functionalization. Scale bar 100 nm.

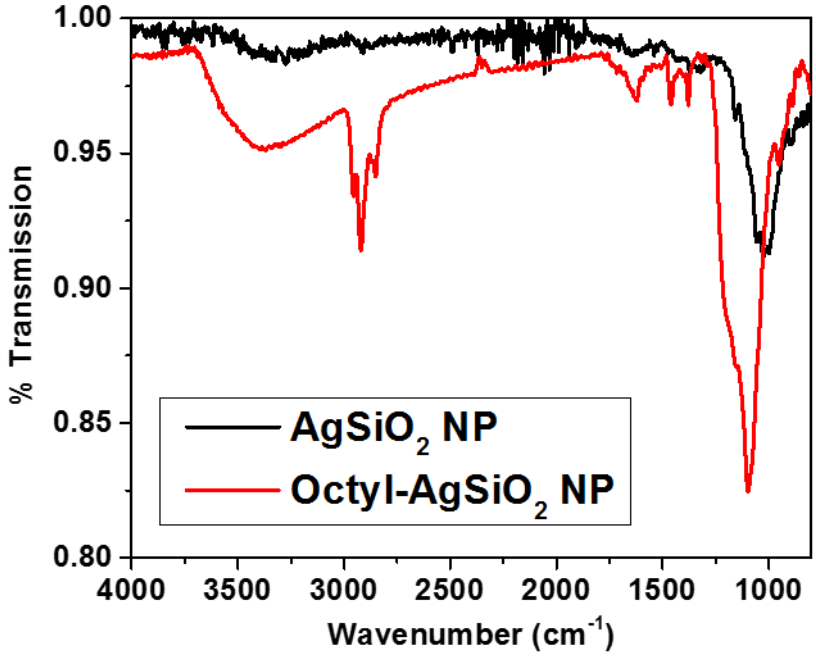

Figure 4.2. NIR transmission spectra of $AgSiO_2$ before and after octyl functionalization.

4.2.2 Synthesis of Organic Ligand Silver Nanoparticles

To fully investigate the silica shell insulation effects of $AgSiO_2$ NP doped OPVs, uncoated AgNPs are a necessary control. AgNPs were synthesized via a previously reported method,[24] where oleylamine is utilized as both a reducing agent and capping ligand. The size of the AgNPs can be tuned from 8-32 nm by simply adjusting the solvent and reaction time. In attempt to match the size of the $Ag@SiO_2$ NP, DCB was chosen as the solvent with an 8 hr reaction time, after three rounds of precipitation the particles were dispersed in DCB. The resultant 28.1 ± 2.15 nm AgNPs and the corresponding LSPR absorption spectra are shown in Figure 4.3.

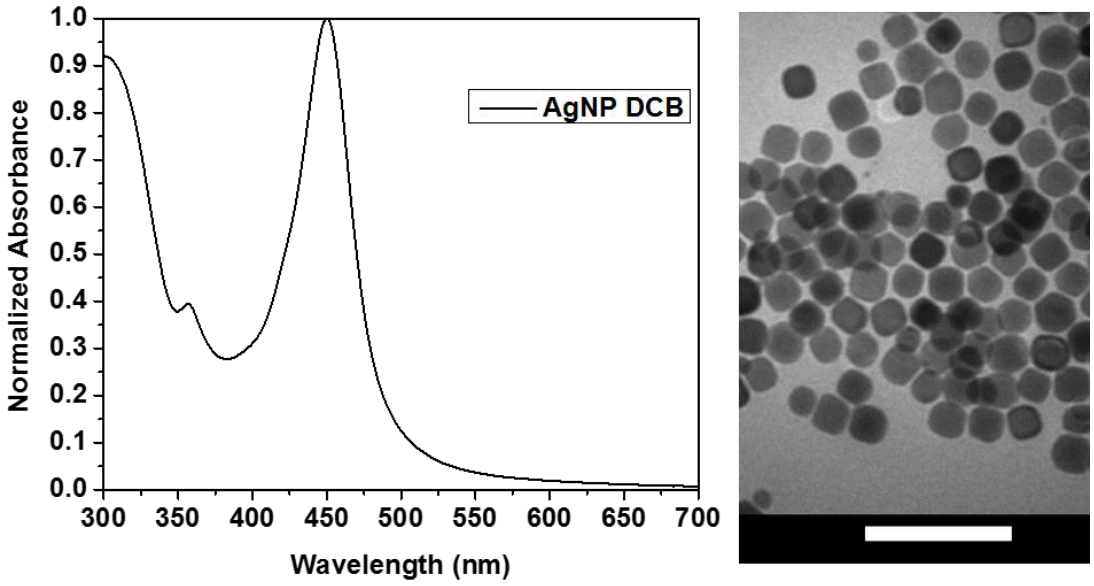

Figure 4.3. UV/Vis absorption spectra of AgNP LSPR (left), and TEM images of AgNP synthesized and dispersed in DCB.

4.2.3 Characterization of NP-Doped OPV Devices

4.2.3.1 J-V Characterization of Octyl-$AgSiO_2$ Doped PSCs

To investigate the effect of plasmonic nanoparticle doping of OPVs, inverted PSCs were fabricated with the device geometry of ITO/PEIE/P3HT:PCBM (1:0.8)/MoO_x/Ag,

shown in Figure 4.4. The plasmonic nanoparticles were doped into the active layer, and P3HT:PCBM (1:0.7) without nanoparticles was used as a reference. Octyl functionalized $Ag@SiO_2$ NP dispersed in DCB, were added to P3HT:PCBM solution to systematically increasing the NP/Polymer ratio, while maintaining a constant polymer concentration. These solutions were spun on PEIE modified ITO substrate, devices with 150 nm active layer thickness were obtained and subjected to electrical characterization.

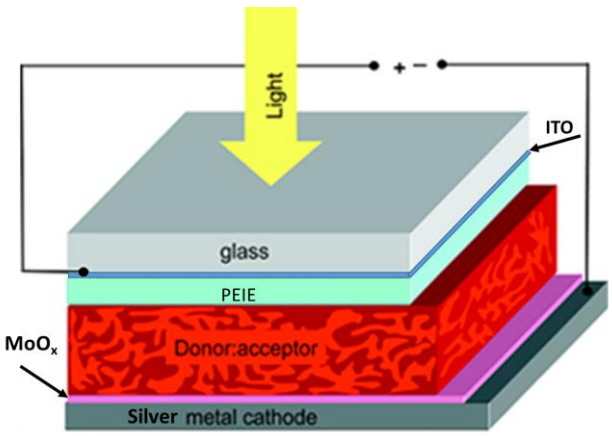

Figure 4.4. Schematic representation of the inverted device geometry used in this study.

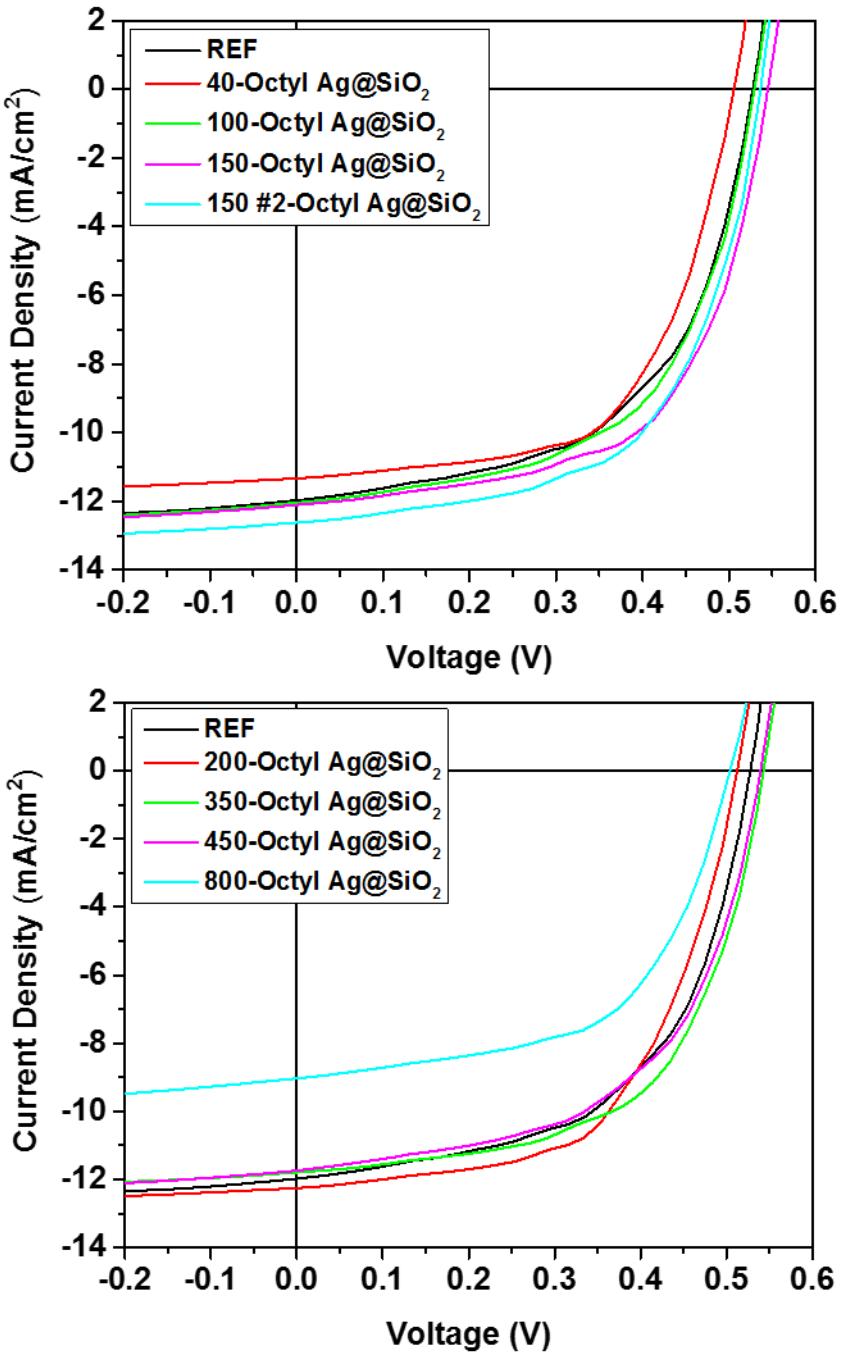

Figure 4.5. J-V characteristics under illumination for NP doped P3HT: PCBM based PSCs. Champion device of each nanoparticle concentration shown.

Figure 4.5 shows the comparison of the J-V characteristics of the champion NP-doped PSCs compared to the P3HT:PCBM reference device. The averaged device

performance parameters are shown in Table 4, where 8 and 16 devices were averaged for the NP-PCSs and reference samples respectively. The average reference devices showed a J_{SC} of 11.48 mA/cm^3, V_{OC} of 0.53 V, *FF* of 55.9, and a *PCE* of 3.38 %, where the champion device showed a PCE of 3.58 %. At low NP concentrations no significant change to the device parameters is evident. The optimal $AgSiO_2$ NP loading of 150 µl resulted in a sharp increase in *FF* to 60.51% (150 #1) and 58.89% (150 #2), as compared to 55.89% for the reference. Octy-150 #1 shows modest increase in J_{SC}, 150 #2 shows an enhancement of J_{SC} to 12.0 mA/cm^2 compared to the 11.4 mA/cm^2 in reference set. This increase in J_{SC} is offset by the slightly lower *FF* resulting in nearly identical *PCE*s, 3.79% (150 #2) and 3.78% (150 #2). Further increases in NP concentration show a gradual decline in the average J_{SC} values. Interestingly, elevated *FF* factor values are seen with loading as high as 450 µl NP loading resulting in equal or higher *PCE* values as compared to the reference devices. At extremely high loading, the *FF* and J_{SC} drop rapidly, likely due to the disruption of the internal morphology of the P3HT: PCBM blend. The addition of 150 µl $AgSiO_2$ NPs resulted in the optimal device performance, where an average *PCE* of 3.79%, with the champion device achieving a *PCE* of 4.01%, corresponding to 12% increase as compared to the reference device.

Table 4. Summary of the averaged device performance of P3HT:PCBM solar cells doped with various concentrations of Octyl-$AgSiO_2$ NPs (51µg/ml). 8 devices averaged for NP samples. 16 devices averaged for reference samples. Champion device in parenthesis.

Octyl $AgSiO_2$ (µl)	J_{SC} (mA/cm^2)	V_{OC} (V)	*FF* (%)	*PCE* (%)
REF	11.5 ± 0.4	0.53 ± 0.01	56.0 ± 0.8	3.4 ± 0.1 (3.6)
40	11.1 ± 0.2	0.52 ± 0.0	57.4 ± 0.7	3.3 ± 0.1 (3.4)
100	11.6 ± 0.4	0.53 ± 0.01	55.6 ± 0.9	3.5 ± 0.1 (3.6)

150 #1	11.6 ± 0.2	0.54 ± 0.01	60.5 ± 1.8	3.8 ± 0.1 (4.0)
150 #2	12.0 ± 0.4	0.54 ± 0.00	58.9 ± 1.0	3.8 ± 0.1 (4.0)
200	11.5 ± 0.6	0.52 ± 0.00	57.6 ± 1.2	3.4 ± 0.2 (3.7)
350	11.3 ± 0.6	0.54 ± 0.00	59.5 ± 1.2	3.6 ± 0.2 (3.8)
450	11.0 ± 0.6	0.54 ± 0.01	56.9 ± 2.4	3.3 ± 0.2 (3.5)
800	8.5 ± 0.5	0.50 ± 0.01	53.6 ± 3.6	2.3 ± 0.3 (2.6)

4.2.3.2 J-V Characterization of AgNP Doped PSCs

To investigate the effectiveness of the silica shell's ability to mitigate charge carrier losses to quenching at the metal surface, AgNP were doped into the active layer similarly to the $AgSiO_2$ NP. Figure 4.6, show the average J-V characteristics of AgNP-doped PSCs, where 8 device were averaged for each NP concentration and P3HT:PCBM reference. The summary of the averaged photovoltaic parameters can be found in Table 5. The device performance remains unaffected by the lowest dose of AgNP (75 µl), with the addition of 150 µl a clear drop in *FF* to 44.01% is observed, likely due to exciton recombination and charge carrier quenching at the metal nanoparticle surface. These effects are more dramatic in the 225 µl samples a reduction in J_{SC} is also observed. Any further increase in AgNP concentration resulted in complete device breakdown, potential due to large NP aggregates shorting the device. It is clear from these results that even at low NP loading, metal assisted losses are disruptive to the performance of the PSCs. It is evident that the ≈ 5 nm silica coating is sufficient to insulate the metal surface from these detrimental effects.

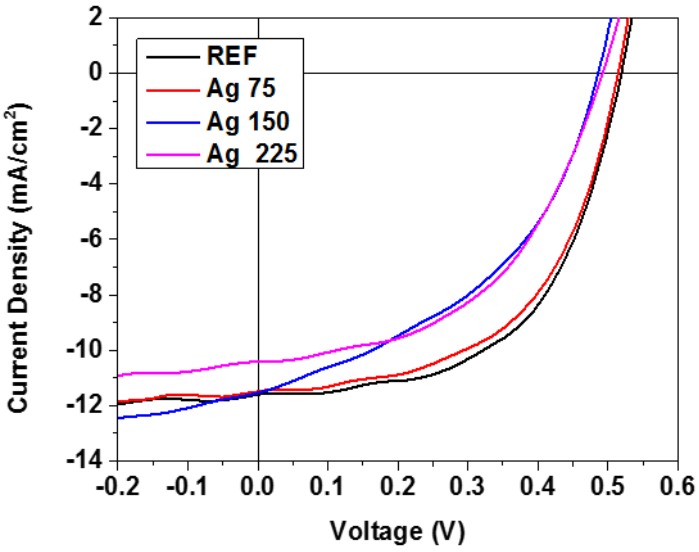

Figure 4.6. J-V characteristics under illumination for AgNP doped P3HT:PCBM based PSCs. The average of 8 devices at each NP concentration shown.

Table 5. Summary of the averaged device performance of P3HT:PCBM solar cells doped with various concentrations of AgNPs (84.5 µg/ml). 8 devices averaged for all samples. Champion device in parenthesis.

Device name	J_{SC} (mA/cm^2)	V_{OC} (V)	*FF* (%)	*PCE* (%)
REF	11.6 ± 0.4	0.52 ± 0.01	55.2 ± 1.2	3.4 ± 0.2 (3.5)
Ag 75	11.5 ± 0.6	0.52 ± 0.00	54.2 ± 0.7	3.2 ± 0.2 (3.5)
Ag 150	11.4 ± 0.4	0.48 ± 0.01	43.6 ± 1.8	2.4 ± 0.2 (2.6)
Ag 225	10.4 ± 0.6	0.48 ± 0.03	49.2 ± 3.5	2.5 ± 0.3 (2.7)

4.2.3.3 UV/VIS Characterization of $AgSiO_2$ NP-doped PSCs

Figure 4.7 shows the linear UV/Vis Spectra of the PSCs discussed in section 4.2.3.1. It has been purposed that addition of plasmonic NPs with increase the optical absorption in the polymer donor material through plasmonic field enhancements and an increased optical path length via light scattering. No clear correlation between the absorption seen in Figure 4.7, and the measured J_{SC} can be extracted. The macroscopic measurement of UV/Vis can suffer from local variations in film thickness, reflectivity, or

scattering within the measurement volume. Simple UV/Vis measurements of optical density do not appear sensitive enough to truly elucidate the optical phenomena relevant to plasmonic enhancements. It is possible that with careful measurement of the scattering and reflectance to determine absorption coefficient might be more informative.

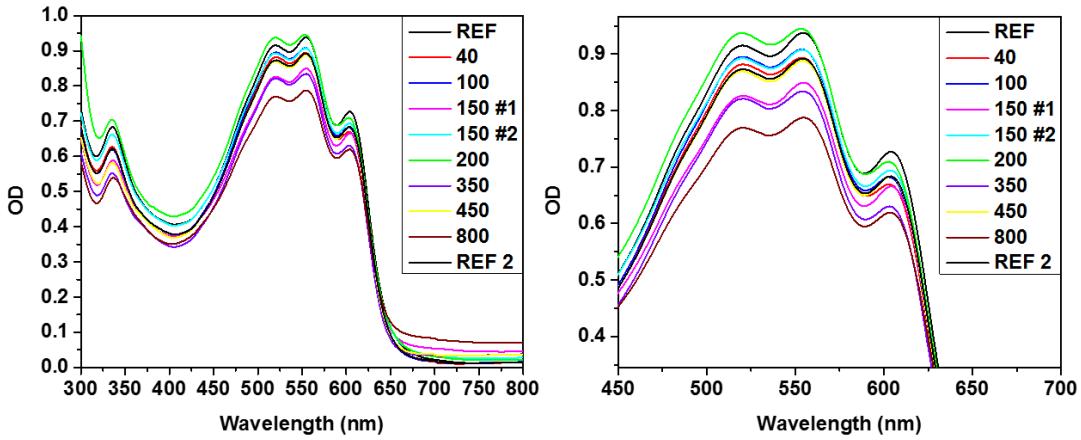

Figure 4.7. UV/Vis spectra of PSCs doped with various concentrations of $AgSiO_2$ NP. Spectra on right zoomed in for clarity.

4.2.3.4 Transient Absorption of $AgSiO_2$ NP PSCs

Transient absorption is discussed in detail in section 1.5.4. In this study transient absorption is used to investigate exciton and charge carrier formation and decay kinetics. By varying the delay between the pump and probe pulses, the excited state absorption can be monitored over time, affording the spectral signature and the decay kinetic of the excited species. Figure 4.8, shows the photo-induced absorption (PIA) spectra of the optimized $AgSiO_2$ NP-doped PSCs. P3HT: PCBM blends have been extensively studied using transient absorption, thus the spectral signatures of the relevant species are well known.[25-27] A broad peak extending from 900-1400 nm is assigned to singlet excitons of P3HT which decays to zero within 100ps. A broad long-lived P3HT polaron band extends from ≈ 650-

1050 nm, which overlaps with both the exciton peak and the stimulated emission peak centered at 700 nm, which coincides with P3HT photoluminescence.[27] Stimulated emission produces a negative signal in transient absorption spectra. Additionally, the onset of the polaron band is further complicated by photo-induced electro-absorption resulting in a stark shift of the absorption onset.[25] The ground state bleach (GSB) is seen as a negative signal in PIA at 500-620 nm similar vibrionic structure seen in P3HT:PCBM film absorption. For this work, 1055 nm is used to monitor the exciton signal, as the sensitivity of the detector used is unreliable past ≈ 1060 nm. The exciton signal is effectively decoupled from the broad polaron peak that extends from ≈ 650-1000 nm. The polaron peak is long lived and remains virtually unchanged throughout the duration of these measurements.

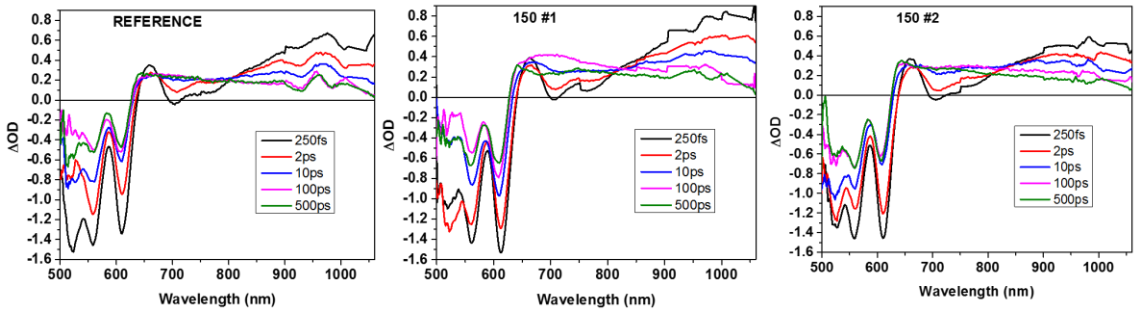

Figure 4.8. Transient spectra of the optimized $AgSiO_2$ NP-doped PSCs. Showing the excited state absorption as an evolution of time. Reference device (left), 150 #1 (middle), 150 #2 (right)

Temporal snapshots of the PIA spectra of the $AgSiO_2$ NP-doped PSCs are shown in Figure 4.9. Just after excitation (250 fs), 150 #1 shows the highest production of excitons relative to the other films of the same thickness. Interestingly, 150 #2 show the lowest instantaneous exciton formation, although it had the highest measure J_{SC} measured in this study. Both 150 #1 and 150 #2 show increased GSB as compared to the reference device.

By 10 ps, it appears that the reference device has nearly decayed to zero in the exciton region, where as both NP devices still show a minor signal at 100 ps. The NP devices show higher population of long lived polarons compared to the reference throughout the duration of the measurement (500 ps), which is indicative of a higher population free charge carriers. The GSB shows a lower number of molecules have returned to the ground state compared to the reference device, which also supports the conclusion of increased carrier population.

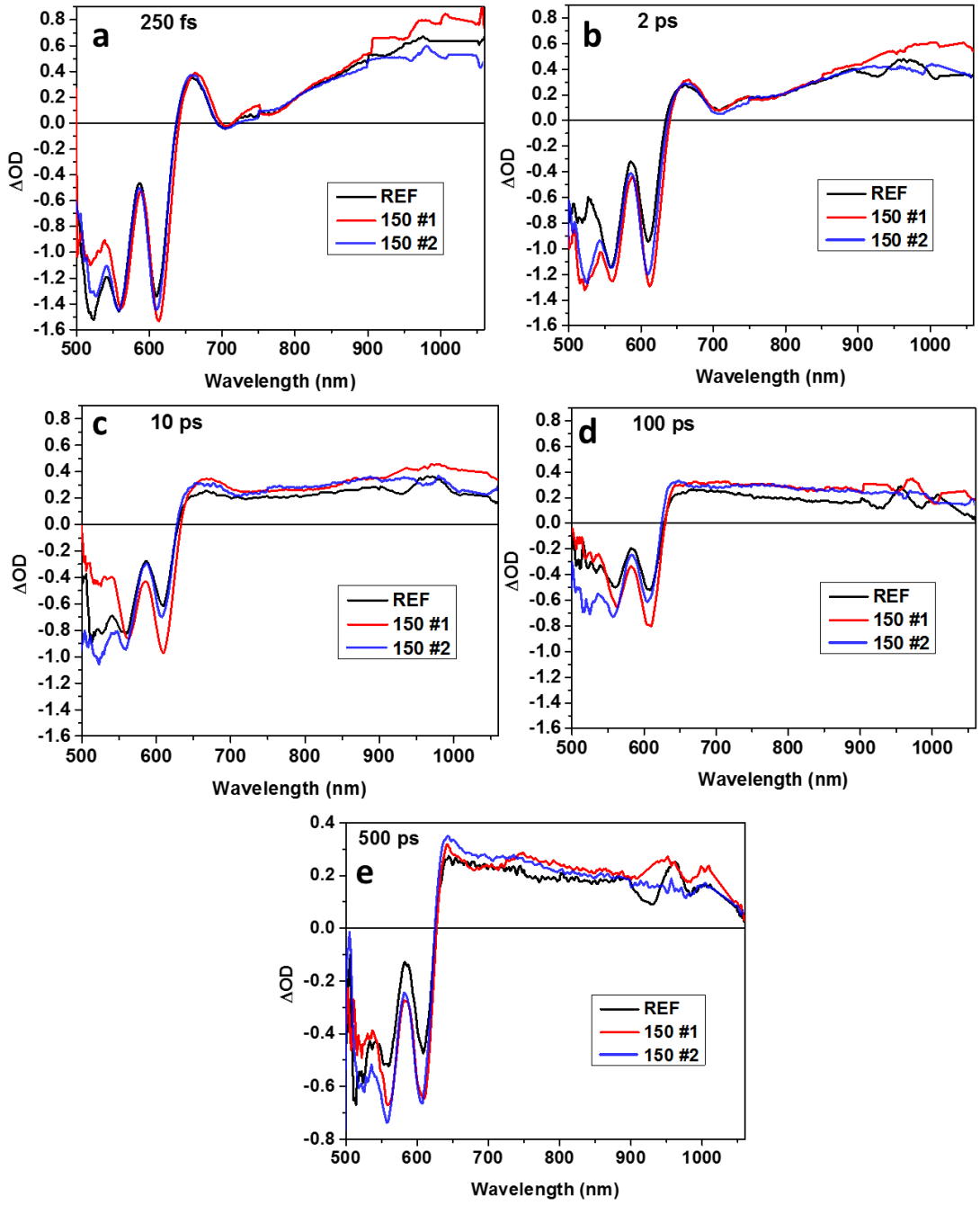

Figure 4.9. Temporal snapshots of the PIA spectra of the optimized PSCs doped with $AgSiO_2$ NPs. a) 250 fs, b) 2 ps, c) 10 ps, d) 100 ps, e) 500 ps.

Figure 4.10 shows the PIA transient decays for the reference device, taken at wavelengths of the relevant processes. The exciton signal at 1050 nm has fully decayed by

100 ps. The long-lived polaron band is shown at 650 nm and 825 nm. The stimulated emission peak at 700 nm recovers to the level of the polaron band within ≈ 20 ps. The signal at 950 nm is a combination of the singlet exciton and polaron peak, in which it decay to the level of the polaron peak on the same time scale as the exciton peak decays to zero.

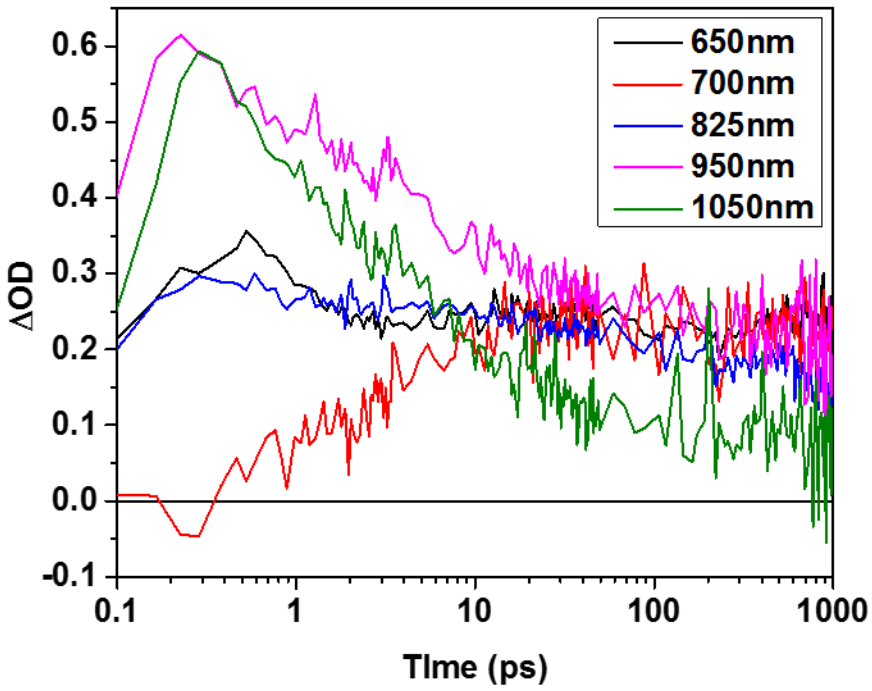

Figure 4.10. Select kinetic traces of the PIA at various wavelengths from the reference device.

Figure 4.11 show the recovery of the GSB at 610 nm and the transient decay of the PIA at 1050 nm. The decay profiles were fitted with a bi-exponential decay function and the fitted decay times are summarized in Table 6. It is clear from Figure 4.11 that the NP samples maintain a higher signal through the time scale of the measurement. The fitted decay times are also significantly longer for the $AgSiO_2$ NP doped samples, which is indicative of reduction in fast recombination processes which would be consistent with the improved FF in these devices.

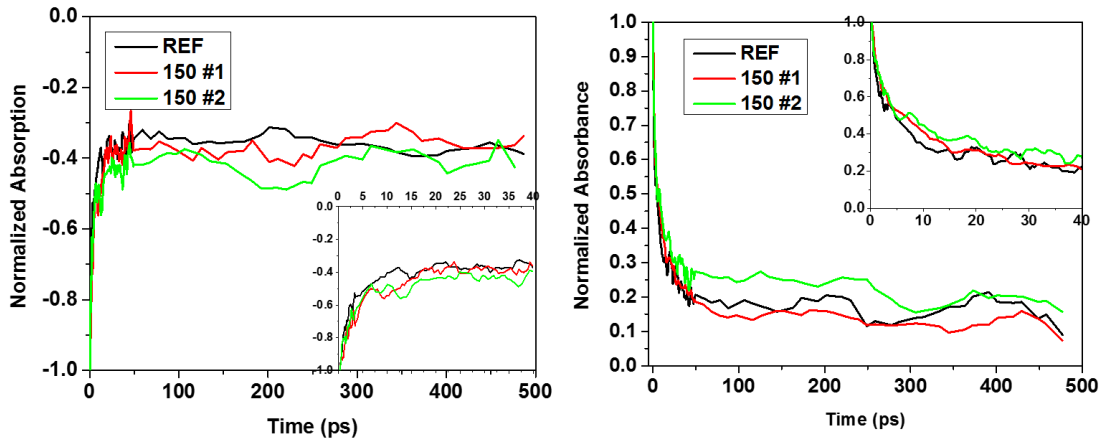

Figure 4.11. Kinetic trace of GSB recovery at 610 nm (left). PIA decay at 1050 nm (right). Insets zoomed in to short time range.

Table 6. Summary of fitted decay times obtain from the reference, 150 #1, and 150 #2. Fitted with a bi-exponential decay equation $y = A1*e^{(-x/t1)} + A2*e^{(-x/t2)} + y0$.

610 nm			
Device	**REF**	**150 #1**	**150 #2**
t1 (ps)	1.11 ± 0.15	1.52 ± 0.35	1.99 ± 0.32
t2 (ps)	6.65 ± 0.75	9.61 ± 1.16	12.9 ± 3.05

1050 nm			
Device	**REF**	**150 #1**	**150 #2**
t1 (ps)	0.87 ± 0.09	1.56 ± 0.086	1.60 ± 0.14
t2 (ps)	14.5 ± 0.81	20.9 ± 0.76	18.6 ± 1.14

4.3 Conclusion

In this chapter the $AgSiO_2$ NP dopant concentration was optimized to achieve enhancement of the NP-PSCs. With an optimal nanoparticle concentration of 150 µl $AgSi_2O$ NPs, an average PCE of 3.79% was achieve in the composite devices as compared to 3.38% for the P3HT:PCBM reference, a 12% enhancement. The champion NP-device had as *PCE* of 4.01% compared to 3.58% for the reference samples. These enhancements

resulted from increases in J_{SC} and *FF*. It was also demonstrated that the silica shell is effective at mitigating metal assisted quenching effects. Linear absorption measurements of the PSCs showed no reliable increase in absorption. To further investigate the origin of these enhancements femtosecond transient absorption spectroscopy was employed. The NP-PSCs demonstrated a higher concentration of polarons at 500 ps after excitation compared to the reference device. Surprisingly though, only one of the two NP-doped PSCs showed an increase in exciton production upon excitation compared to the reference. The NP-devices were found to have longer exciton decay lifetimes, attributed to a reduction in fast recombination processes, which could be related to the improved *FF* or device morphology in the composite devices. This work demonstrates the need for complete electrical and optical characterization of the plasmonic PSCs devices to truly understand enhancements in PSCs. Often, an increase in J_{SC} is attributed to optical absorption enhancement, without proper investigation of the device photo-physics.

4.4 Experimental Methods

4.4.1 Aqueous AgNP Synthesis

Quasi-spherical silver nanoparticles were synthesized via a previously reported method.[28] In short, 12.5 mL ascorbic acid (4.8 mM), 8.825 mL sodium citrate (1 w/w%), were added to 80 mL DIW. The reaction mixture is adjusted to pH 9.5 with 0.1 M citric acid and 0.1 M NaOH. The solution was placed in 30 °C hot bath, and 1 mL aqueous solution of $AgNO_3$ (0.1 M) was injected into the reaction mixture and stirred at 1200 RPM for 15 min. The contents of the reaction flask were then transferred to an oil bath at 100 °C for 30 min without stirring and then placed in ice bath to quench the reaction.

4.4.2 Ag@SiO_2 Nanoparticle Synthesis

The silica coating of Ag nanoparticles was performed using a modified procedure from previous reports.[13,23] 2.0 mL of AgNP, filtered through 0.8 μm Nylon filter to remove large or aggregated nanoparticles, were added to 20 mL of 95/5% ethanol water mixture in a 50 mL centrifuge tube. 600-1200 μL TEOS (10 mM in ethanol) were added and then followed by the addition of 200 μL DMA. The reaction mixture was then shaken with vortex mixer for 2 hrs. Ag@SiO_2 NP were collected using a centrifuge operating at 8000 RPM for 15 minutes. The resultant Ag@SiO_2 NP were washed 3 times each with ethanol and water, and then dispersed in 2 mL of ethanol.

4.4.3 Non-polar AgNP synthesis

These AgNP were synthesized as previously reported.[24] 50.0 mg of $AgC_2H_3O_2$ is dissolved in 2.0 g oleylamine. This solution is quickly injected to 50.0 ml of refluxing dichlorobenzene (DCB). The mixture is refluxed for 8hrs, and then cooled to room temperature. The solvent is then evaporated to 15 ml with either a rotary evaporator or by vacuum distillation. Once volume is reduced to 15 ml and cooled to room temperature. 200 ml of methanol to precipitate the AgNPs. The precipitate is then dissolved in 10 ml of hexane and precipitated with 40ml of methanol two times. The precipitate is then dried in vacuo, and then dissolved in in DCB.

4.4.4 Functionalization of $AgSiO_2$ NP

The 35.0 ml of $AgSiO_2$ NP are collected via centrifuge and dispersed in 50.0 ml toluene. The concentration of octyltriethoxysilane is adjusted to 3.0 mM and refluxed

overnight. The solution is cooled to room temperature and the particles are collected via centrifuged @ 8000 RPM for 12 minutes and washed with toluene four times. The functionalized NP are dispersed in DCB.

4.4.5 NP characterization

AgNP and Ag@SiO_2 NP were drop-casted on carbon coated copper TEM grids (Electron Microscopy Science). TEM images were collected on a JEOL 100CX II TEM with a 100 keV accelerating voltage. UV/VIS measurements were taken with a Shimadzu UV-2401 Dual-Beam UV-Vis Spectrophotometer. AgNPs were drop-cast on KBr powder, the solvent was evaporated, and pelleted for IR spectroscopy taken with Bruker Alpha-T ATR-FTIR Fourier Transform Infrared Spectrometer (FTIR).

4.4.6 Device Fabrication

P3HT:PCBM (1:0.7) dissolved in DCB at 80.0 mg/ml. The solution was heated on a hotplate overnight @ 60 ºC. PEIE was diluted to 0.2 wt/wt % in methoxyethanol and stirred overnight. ITO patterned substrates were sequentially sonicated in detergent, water, acetone, and IPA for 15 minute cycles. The substrates were then dried under a stream of nitrogen. The substrates were treated with O_2 plasma for 3 min. The PEIE solution was filtered with a 0.2 µm syringe filter onto ITO substrate and spun @ 5000 RPM for 60 sec, and then annealed on a hotplate at 110 ºC for 10 min and cooled to room temperature. The polymer solution is cooled to room temperature and filtered through a 0.2 µm syringe filter. To 150 µl of pre-filtered polymer solution was added 150 µl NP solution of various concentrations. The solution was then sonicated for 10 seconds, stirred 5 min, sonicated 10

seconds, and then flooded onto an ITO substrates and spun @ 700 RPM for 60 seconds. The still wet films were then stored in a petri dish for at least 3 hr for solvent annealing.

Devices were thermally annealed on a hotplate inside an Ar filled glovebox. The devices were then loaded into vacuum chamber and pumped down to $1x10^{-5}$ mbar. 10 nm MoO_3 and 160 nm Ag are thermally deposited. The J-V characteristics of all photovoltaic devices were evaluated under AM 1.5 G solar illumination (100 mW/cm^2) using a Keithly 4200 semi-conductor parameter analyzer system with a Newport Thermal Oriel 94021 Solar simulator reference with a silicon collar cell.

4.4.7 Transient Absorption Spectroscopy

Differential Transmission spectroscopy measurements were performed using an ultrafast laser system (Pharos Model PH1-20-0200-02-10, Light Conversion) emitting 1030-nm pulses at 100 KHz, with an output power of 20 W and pulse duration of ~ 220 fs. Experiments were carried out in an integrated transient absorption/time-resolved photoluminescence commercial setup (Light Conversion Hera). Pump wavelengths in the spectral range 360–2600 nm were generated by feeding 10W from the laser output to a commercial optical parametric amplifier (Orpheus, Light Conversion, Lithuania), while 2 W are focused onto a sapphire crystal to obtain a single-filament white-light continuum covering the spectral range ~490−1050 nm for the probe beam. When higher energy probe light was required, a blue white-light continuum was similarly obtained by using the second harmonic of the laser output instead. The probe beam transmitted through the sample is detected by an imaging spectrograph (Shamrock 193i, Andor Technology Ltd., UK) in combination with a multichannel detector (256 pixels, 200–1100-nm wavelength

sensitivity range). Energy densities of 2 μJ/cm^2, most of the measurements were carried out at 215 nJ/cm^2; with atypical spot diameter of 1.9 mm estimated at the 1/e^{2}plane).

4.5 REFERENCES

1. Tseng, W.-H.; Chiu, C.-Y.; Chou, S.-W.; Chen, H.-C.; Tsai, M.-L.; Kuo, Y.-C.; Lien, D.-H.; Tsao, Y.-C.; Huang, K.-Y.; Yeh, C.-T.; He, J.-H.; Wu, C.-I.; Huang, M. H.; Chou, P.-T., Shape-Dependent Light Harvesting of 3D Gold Nanocrystals on Bulk Heterojunction Solar Cells: Plasmonic or Optical Scattering Effect? *The Journal of Physical Chemistry C* **2015,** *119* (14), 7554-7564.

2. Janković, V.; Yang, Y.; You, J.; Dou, L.; Liu, Y.; Cheung, P.; Chang, J. P.; Yang, Y., Active Layer-Incorporated, Spectrally Tuned Au/SiO2 Core/Shell Nanorod-Based Light Trapping for Organic Photovoltaics. *ACS Nano* **2013,** *7* (5), 3815-3822.

3. Choi, H.; Lee, J.-P.; Ko, S.-J.; Jung, J.-W.; Park, H.; Yoo, S.; Park, O.; Jeong, J.-R.; Park, S.; Kim, J. Y., Multipositional Silica-Coated Silver Nanoparticles for High-Performance Polymer Solar Cells. *Nano Letters* **2013,** *13* (5), 2204-2208.

4. Lu, L.; Luo, Z.; Xu, T.; Yu, L., Cooperative Plasmonic Effect of Ag and Au Nanoparticles on Enhancing Performance of Polymer Solar Cells. *Nano Letters* **2013,** *13* (1), 59-64.

5. Wang, J.; Lee, Y.-J.; Chadha, A. S.; Yi, J.; Jespersen, M. L.; Kelley, J. J.; Nguyen, H. M.; Nimmo, M.; Malko, A. V.; Vaia, R. A.; Zhou, W.; Hsu, J. W. P., Effect of Plasmonic Au Nanoparticles on Inverted Organic Solar Cell Performance. *The Journal of Physical Chemistry C* **2013,** *117* (1), 85-91.

6. Wang, C.; Zhang, W.; Zhao, Z.; Wang, Y.; Gao, P.; Luo, Y.; Luo, X., Plasmonic Structures, Materials and Lenses for Optical Lithography beyond the Diffraction Limit: A Review. *Micromachines* **2016,** *7* (7).

7. Jang, J.-W.; Park, B.; Nettikadan, S., Generation of plasmonic Au nanostructures in the visible wavelength using two-dimensional parallel dip-pen nanolithography. *Nanoscale* **2014,** *6* (14), 7912-7916.

8. Srituravanich, W.; Fang, N.; Sun, C.; Luo, Q.; Zhang, X., Plasmonic Nanolithography. *Nano Letters* **2004,** *4* (6), 1085-1088.

9. LIU, H.; TENG, J., PLASMONIC NANOLITHOGRAPHY: TOWARDS NEXT GENERATION NANOPATTERNING. *Journal of Molecular and Engineering Materials* **2013,** *01* (01), 1250005.

10. Park, H. J.; Guo, L. J., Optical enhancement effects of plasmonic nanostructures on organic photovoltaic cells. *Chinese Chemical Letters* **2015,** *26* (4), 419-425.

11. Wu, B.; Wu, X.; Guan, C.; Fai Tai, K.; Yeow, E. K. L.; Jin Fan, H.; Mathews, N.; Sum, T. C., Uncovering loss mechanisms in silver nanoparticle-blended plasmonic organic solar cells. *Nature Communications* **2013,** *4*, 2004.

12. Topp, K.; Borchert, H.; Johnen, F.; Tunc, A. V.; Knipper, M.; von Hauff, E.; Parisi, J.; Al-Shamery, K., Impact of the Incorporation of Au Nanoparticles into Polymer/Fullerene Solar Cells. *The Journal of Physical Chemistry A* **2010,** *114* (11), 3981-3989.

13. Kobayashi, Y.; Katakami, H.; Mine, E.; Nagao, D.; Konno, M.; Liz-Marzán, L. M., Silica coating of silver nanoparticles using a modified Stöber method. *Journal of Colloid and Interface Science* **2005,** *283* (2), 392-396.

14. Lim, E. L.; Yap, C. C.; Mat Teridi, M. A.; Teh, C. H.; Mohd Yusoff, A. R. b.; Hj Jumali, M. H., A review of recent plasmonic nanoparticles incorporated P3HT: PCBM organic thin film solar cells. *Organic Electronics* **2016,** *36* (Supplement C), 12-28.

15. Hanske, C.; Sanz-Ortiz, M. N.; Liz-Marzán, L. M., Silica-Coated Plasmonic Metal Nanoparticles in Action. *Advanced Materials* **2018,** *30* (27), 1707003.

16. Jang, Y. H.; Jang, Y. J.; Kim, S.; Quan, L. N.; Chung, K.; Kim, D. H., Plasmonic Solar Cells: From Rational Design to Mechanism Overview. *Chemical Reviews* **2016,** *116* (24), 14982-15034.

17. Erwin, W. R.; Zarick, H. F.; Talbert, E. M.; Bardhan, R., Light trapping in mesoporous solar cells with plasmonic nanostructures. *Energy & Environmental Science* **2016,** *9* (5), 1577-1601.

18. Crooks, R. M.; Zhao, M.; Sun, L.; Chechik, V.; Yeung, L. K., Dendrimer-Encapsulated Metal Nanoparticles: Synthesis, Characterization, and Applications to Catalysis. *Accounts of Chemical Research* **2001,** *34* (3), 181-190.

19. Martin, M. N.; Basham, J. I.; Chando, P.; Eah, S.-K., Charged Gold Nanoparticles in Non-Polar Solvents: 10-min Synthesis and 2D Self-Assembly. *Langmuir* **2010,** *26* (10), 7410-7417.

20. McMahon, J. M.; Emory, S. R., Phase Transfer of Large Gold Nanoparticles to Organic Solvents with Increased Stability. *Langmuir* **2007,** *23* (3), 1414-1418.

21. Lista, M.; Liu, D. Z.; Mulvaney, P., Phase Transfer of Noble Metal Nanoparticles to Organic Solvents. *Langmuir* **2014,** *30* (8), 1932-1938.

22. Petcu, C.; Purcar, V.; Spătaru, C.-I.; Alexandrescu, E.; Şomoghi, R.; Trică, B.; Nițu, G. S.; Panaitescu, M. D.; Donescu, D.; Jecu, M.-L., The Influence of New Hydrophobic Silica Nanoparticles on the Surface Properties of the Films Obtained from Bilayer Hybrids. *Nanomaterials* **2017,** *7* (2).

23. Liu, S.; Zhang, Z.; Han, M., Gram-Scale Synthesis and Biofunctionalization of Silica-Coated Silver Nanoparticles for Fast Colorimetric DNA Detection. *Analytical Chemistry* **2005,** *77* (8), 2595-2600.

24. Hiramatsu, H.; Osterloh, F. E., A Simple Large-Scale Synthesis of Nearly Monodisperse Gold and Silver Nanoparticles with Adjustable Sizes and with Exchangeable Surfactants. *Chemistry of Materials* **2004,** *16* (13), 2509-2511.

25. Piris, J.; Dykstra, T. E.; Bakulin, A. A.; Loosdrecht, P. H. M. v.; Knulst, W.; Trinh, M. T.; Schins, J. M.; Siebbeles, L. D. A., Photogeneration and Ultrafast Dynamics of Excitons and Charges in P3HT/PCBM Blends. *The Journal of Physical Chemistry C* **2009,** *113* (32), 14500-14506.

26. Kirkpatrick, J.; Keivanidis, P. E.; Bruno, A.; Ma, F.; Haque, S. A.; Yarstev, A.; Sundstrom, V.; Nelson, J., Ultrafast Transient Optical Studies of Charge Pair Generation and Recombination in Poly-3-Hexylthiophene(P3ht):[6,6]Phenyl C61 Butyric Methyl Acid Ester (PCBM) Blend Films. *The Journal of Physical Chemistry B* **2011,** *115* (51), 15174-15180.

27. Hwang, I.-W.; Moses, D.; Heeger, A. J., Photoinduced Carrier Generation in P3HT/PCBM Bulk Heterojunction Materials. *The Journal of Physical Chemistry C* **2008,** *112* (11), 4350-4354.

28. Qin, Y.; Ji, X.; Jing, J.; Liu, H.; Wu, H.; Yang, W., Size control over spherical silver nanoparticles by ascorbic acid reduction. *Colloids and Surfaces A: Physicochemical and Engineering Aspects* **2010,** *372* (1–3), 172-176.

CHAPTER 5. THE ROLE OF NANOPARTICLE SURFACE FUNCTIONALIZATION ON PLASMONIC ORGANIC PHOTOVOLTAICS

5.1 Introduction

The morphology of a bulk heterojunction PSC is one of the most interesting, mysterious, and vital components of the device. The BHJ relies on spontaneous phase separation to form bi-continuous interpenetrating networks. Exciton diffusion length is ≈ 10 nm, so these networks must be on the order of 10-20 nm. From a blended solution, simply relying on self-assembly of the donor and phase segregation between donor acceptor, the reproducibility of these devices is astonishing. The morphology is a vital to devices performance as it affects both charge separation to generate mobile carriers and collection of electrons and holes at the electrodes. Enormous research efforts have been put into understanding and manipulating the morphology. Thermal annealing of these devices have shown to increase crystallinity and thus performance.[1-2] Slow solvent annealing has been shown to improve morphology.[3] A variety of additives have been studied to manipulate molecular organization and phase segregation in BHJ.[4-5] Reactive cross-linkers have been used to "freeze" the morphology from molecular motion or large crystal growth.[5] Additionally, a variety of different processing methods have been investigated.[6-7] It has been demonstrated that all of the aforementioned external parameters have an impact on the device morphology, the interactions between the donor and acceptor themselves play a crucial role. The miscibility of the donor and the acceptor shown to affect phase segregation and affect microstructure in these binary blends.[8-11] The depth and

breadth of the research on understanding and control of morphology demonstrate its importance to OPV success.

The incorporation of metal nanoparticles into PSCs turns the binary donor acceptor blend into a ternary system and will undoubtedly have an impact on device morphology. The plasmonic OPV community has grossly overlooked the potential impact of NP doping on microstructure of these devices. Nearly every nanoparticle incorporated into these devices has some type of ligand coating for comparability in organic solvents. Very little attention has been paid to systematically study the effect NP surface functionalization has on the composite devices. Wong, conducted a review examining surface chemistry that was used in various plasmonic OPV reports to try and elucidate some conclusions about advantageous surface functionalization, few direct investigations exist.[12]

It has been shown that NP dopes PSCs can tune the self-organization of the bulk heterojunction.[13] The study conducted here will try and bridge this gap, and investigate the effects of various ligand coatings in NP doped PSCs. The organosilanes shown in Figure 5.1 B&C, have been synthesized, and used to functionalize $AgSiO_2$ NP. Three separate moieties of the donor polymer were chosen to ensure compatibility with the OPV blends, while also providing variation in size and geometry. This chapter will discuss the resultant J-V characteristics, spectroscopy and thermal properties to investigate the effects of the surface functionalization.

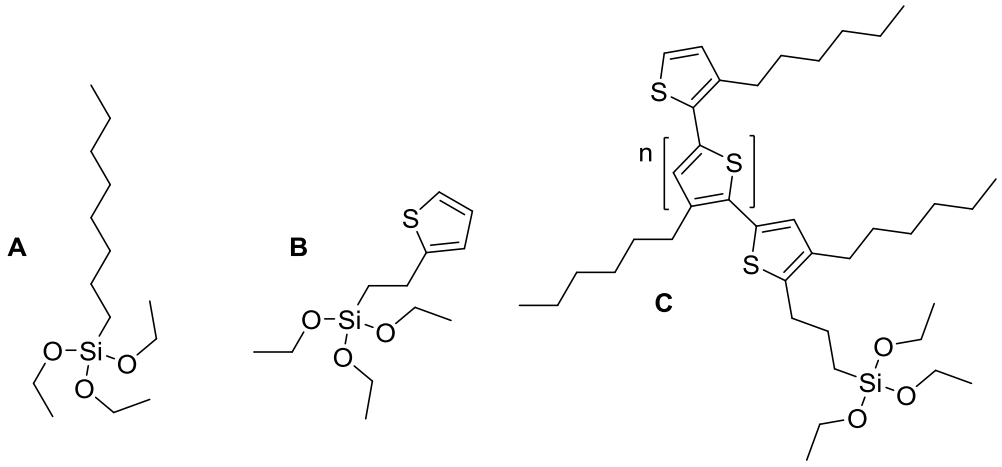

Figure 5.1. The molecular structures of functional silanes used for the surface modification of $AgSiO_2$ NPs.

5.2 Results and Discussion

5.2.1 Synthesis of 2-(3-triethoxysilane)-propylthiophene (B)

The thiophene containing silane (Figure 5.1B) was synthesized according to previous reports.[14-15] Following the reaction pathway shown in Figure 5.2, 2-bromothiophene was reacted with Mg turnings to afford thienylmagnesium bromide Grignard reagent, which was then reacted with allylbromide to afford 2-allylthiophene purified via atmospheric distillation. The allylthiophene was subject to platinum catalyzed Hydrosilyation with triethoxysilane to afford compound B, purified with vacuum distillation, and confirmed via NMR (Appendix A).

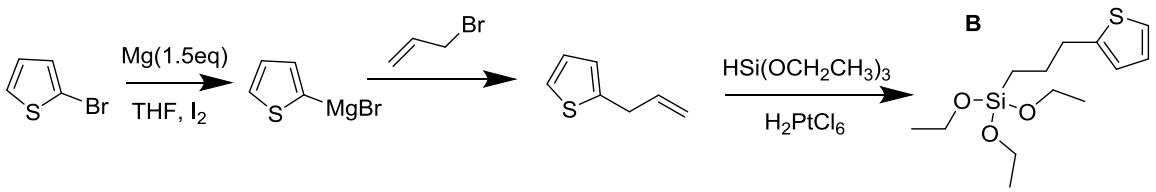

Figure 5.2. Schematic representation of the reaction pathway to achieve Silane B.

5.2.2 Synthesis of P3HT-Silane (C)

P3HT silane (Figure 5.1 C) was synthesized via previously reported methods.[16] 3-hexylthiophene was di-brominated with N-Bromosuccinimide to afford 2,5-dibromo-3-hexylthiophene, which was further purified by distillation. The dibromothiophene was then polymerized by a modified version of the well-known GRIM method.[17] 2,5-dibromo-3-hexylthiophene Grignard reagent is formed with LiCl and tertbutylmagnesiumchloride. Kumada cross coupling polymerization catalyzed by Ni(dppp)Cl_2 is utilized, where the chain length is controlled with amount of catalyst. Finally, while the polymerization is still "living" the reaction is quenched with allylmagnesiumbromide to obtain the allyl terminated polymer. Following Soxhlet extraction the allyl-P3HT undergoes platinum catalyzed Hyrdosilyation with triethoxy-silane, to afford P3HT-silane. Polymer and intermediates verified by NMR found in Appendix A.

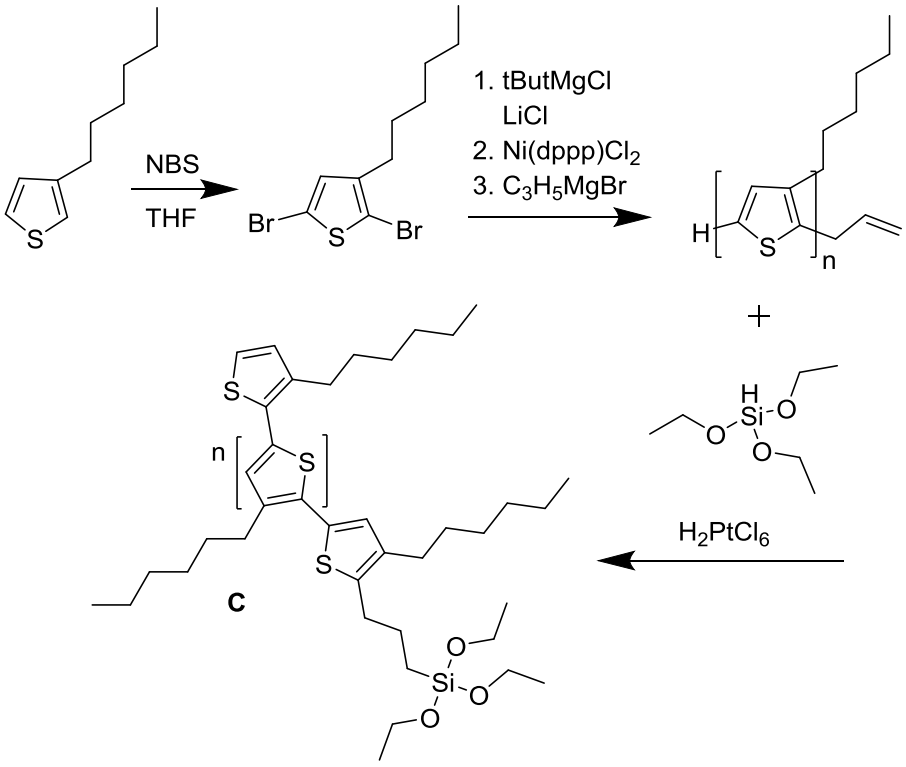

Figure 5.3. Synthetic pathway to achieve P3HT Silane.

The degree of polymerization, allyl functionalization, and silane conversion are estimated from NMR. Figure 5.4 shows the polymer structure and correlating NMR peak assignments. By setting d' and d'' integration equal to 4 protons, the resulting integration of, d, were used as an estimate a chain length of 68 repeat units. Similar comparisons of d' and d" to peaks i, j, h, and k resulted in an 80% average allyl functionalization, of which 90% was converted to silane. Any un-functionalized silane chains will be washed away during the nanoparticle washing and purification. Detailed analysis of the NMR analysis is found in Appendix A.

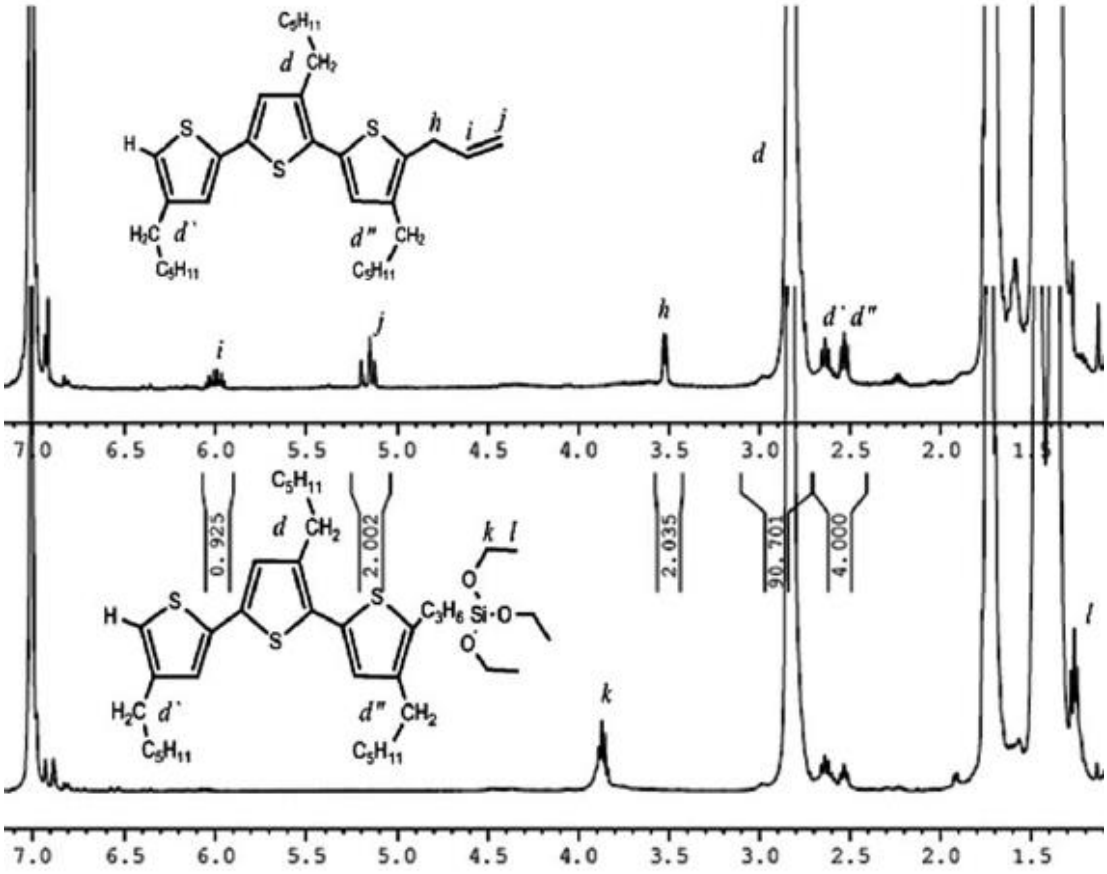

Figure 5.4. NMR spectra with the appropriate peak assignment, used to determine chain length, degree of end group functionalization. Adapted from ref [3].

5.2.3 Characterization of AgSiO2 NP functionalization.

Silica coated silver nanoparticles were synthesized via the method developed in Chapter 2. In short, silver nanoparticles were synthesize via an ascorbic acid reduction of silver ions in the presence of trisodium citrate. The synthesis at a pH of 9.5 resulted in spherical particles with an average diameter of 32.6 ± 4.6 nm. The silver cores with subsequently coated with a thin silica shell via the hydrolysis and condensation of TEOS in an alkaline ethanol/water solution. Here, 700 µl aliquot of TEOS (10mM in EtOH)

resulted in a 4.9 ± 0.9 nm and 5.3 ± 0.7 nm shell for the thiophene and P3HT functionalized NP samples, respectively.

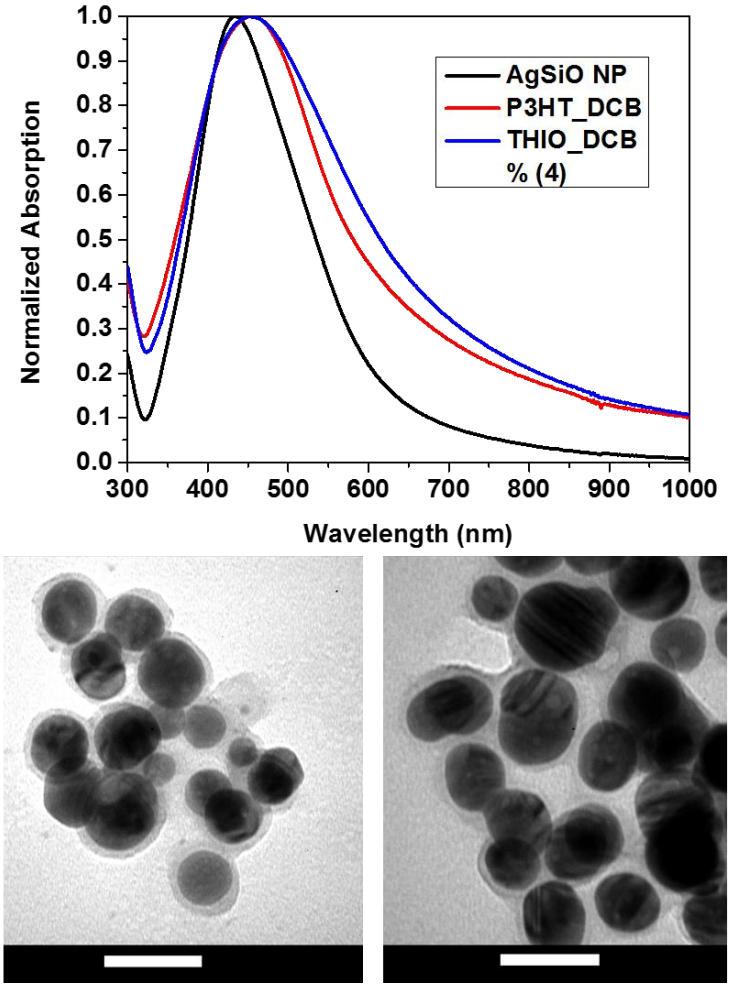

Figure 5.5. UV/Vis absorption spectra of thio-$AgSiO_2$ and p3ht-$AGSiO_2$ NP LSPR (top). TEM images of the resultant functionalized NP. Thio-$AgSiO_2$ NP (left). P3HT-$AgSiO_2$ NP (right). Scale bars 50 nm.

The $AgSiO_2$ NP were functionalized for incorporation into organic solvents with the silane coupling agents described in section 5.2.1. The grafting method described in section 4.2.1 was adopted here as well. The $AgSiO_2$ were collected by centrifuge and dispersed in toluene and refluxed with the relevant silane, where the siloxane exchanges

its ethoxy group by binding to surface hydroxyl with release of EtOH.[18] This removes the need for hydrolysis and condensation, which prevents unwanted growth of the silica network. Infrared spectroscopy was used to verify successful functionalization of the thio-$AgSiO_2$, shown in Figure 5.6, where the strong Si-O-Si peak at 1100 cm^1, and C-H stretching from the propyl-thiophene group. Fluorescence measurements were used to characterize the P3HT-$AgSiO_2$ NP functionalization. After the reaction was complete the NP were washed copiously with toluene and dichlorobenzene until no residual P3HT fluorescence could be seen in the supernatant. The fluorescence of the P3HT-$AgSiO_2$ NP was collected and is shown in Figure 5.7. The functionalized NP fluorescence is commiserate with that of P3HT in solution, and the supernatant show no trace of P3HT.

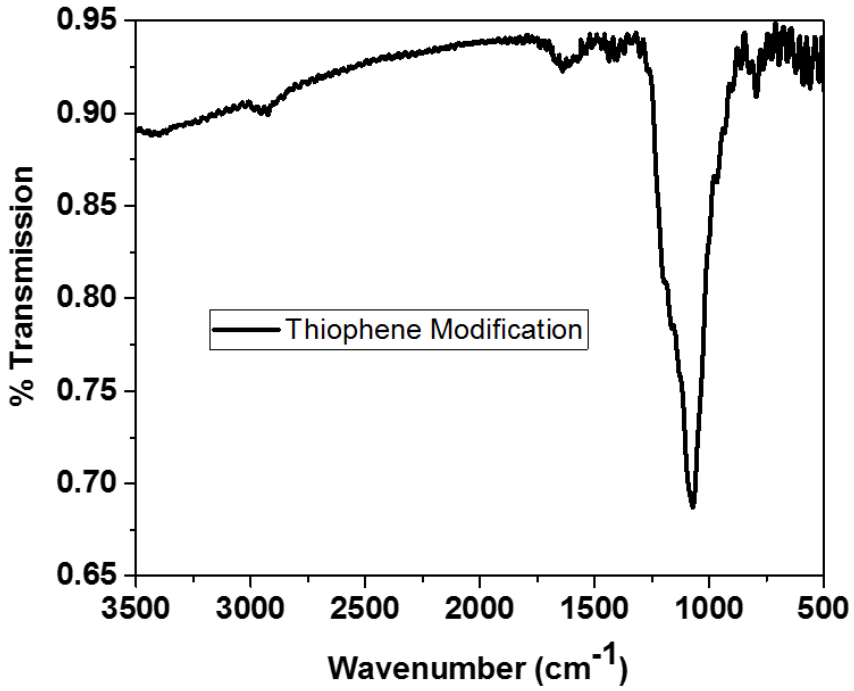

Figure 5.6. IR spectra of functionalized thio-$AgSiO_2$ NP.

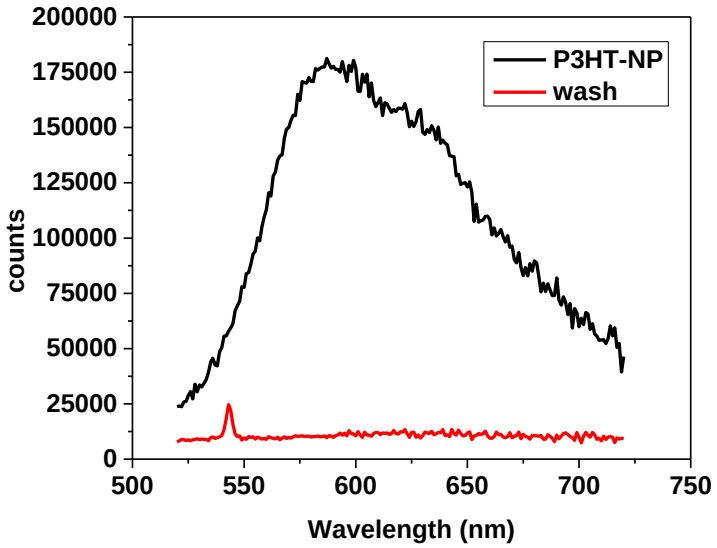

Figure 5.7. Fluorescence spectra of the functionalized p3ht-agSiO$_2$ NP and supernatant after washing.

5.2.4 J-V Characteristics of Thio-AgSiO$_2$ NP-doped PSCs

Plasmonic OPV devices were fabricated in the same geometry as in Chapter 4, and the device architecture can be seen in Figure 4.4. Filtering of the NP solutions is not reliable and can drastically affect the nanoparticle concentration. Thus the P3HT:PCBM (1:0.7) in DCB are prepared at twice the concentration desired for spin-coating, and pre-filtered before the nanoparticle addition. The final polymer concentration after nanoparticle addition is 40 mg/ml which resulted in an active layer thickness of 150 nm. The polymer/nanoparticle solutions deposited on PEIE modified ITO substrate via spin coating. The films are still wet after spin coating due to the high boiling point of DCB, and are slow dried in a petri dish for at least 3 hours, this solvent annealing process has demonstrate to produce an ideal device morphology.[5] The J-V characteristics of PSCs doped with Thio-AgSiO$_2$ NP at various concentrations is shown in Table 7.

Table 7. Summary of the average J-V characteristics of Thio-$AgSiO_2$ NP (103µg/ml) doped PSCs. The champion device in parenthesis. Average of 15 devices for reference, 8 devices for NP-PSCs.

Device name (µl)	J_{SC} (mA/cm^2)	V_{OC} (V)	*FF* (%)	*PCE* (%)
REF	11.5 ± 0.4	0.53 ± 0.01	56.0 ± 0.8	3.4 ± 0.1 (3.6)
Thio-100	11.4 ± 0.6	0.52 ± 0.01	56.4 ± 1.7	3.3 ± 0.2 (3.6)
Thio-150	12.0 ± 0.4	0.54 ± 0.00	59.0 ± 1.9	3.8 ± 0.2 (4.1)
Thio-300	11.7 ± 0.3	0.53 ± 0.01	58.5 ± 1.9	3.6 ± 0.1 (3.8)
Thio-600	11.5 ± 0.3	0.52 ± 0.01	61.6 ± 1.5	3.7 ± 0.1 (3.8)

Figure 5.8 shows the J-V characteristics of the champion devices of each Thio_$AgSiO_2$ NP doped PSC devices. The optimized NP concentration of 150 µl showed an averaged V_{OC} of 0.54 Volts, J_{SC} of 12.02 mA/cm^2, and *PCE* of 3.80%, outperforming the reference in all parameters. Thio-150, Thio-300, and Thio-600 all demonstrate a significant increase in i as compared to the reference, Thio-600 exceedingly so. Only Thio-150 shows any significant enhancements in $J_{SC,}$ which is often characterized as plasmonic enhancement.[19] Three of the devices studied show enhancement of *PCE*, Thio-150 and Thio-300 show increases in both J_{SC} and *FF*, Thio-600 is strictly due to increase *FF*. These results indicate that the morphological impacts of NP doping may be as influential as their optical counterparts.

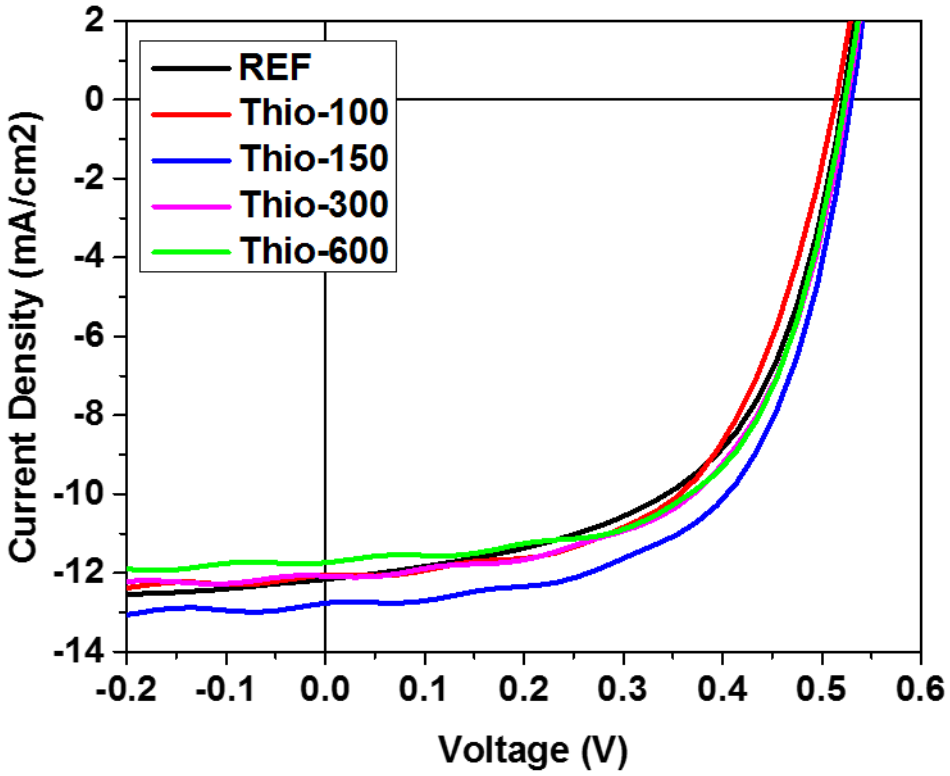

Figure 5.8. J-V Characteristics under illumination for the Thio-AgSiO2 NP doped PSCs. The champion device for concentration shown.

5.2.5 Transient Absorption Spectroscopy

Figure 5.9 shows the transient absorption spectra taken at various time delays. As discussed in section 4.2.3.4, transient absorption is used to monitor the photo-induced species relevant to photovoltaic processes. Excitons absorb in the 900-1400 nm range and decay sub 100 ps time scale, a broad long-live polaron band can be observed from 650-1000 nm and exist longer than the measurement, and the GSB is observed between 500-650 nm. Monitoring the exciton production at 1050 nm, at short times (250 fs, a), surprisingly the reference cell shows a significantly stronger signal than the NP devices. The NP-doped sample show a stronger ground state bleach and a significant increase in the polaron peak at 660 nm relative to the reference, thus its plausible some fraction of excitons

decayed to polarons. By two picoseconds, significant recovery of the GSB is observed, which is consistent with the ultra-fast component of the GSB fitted decay times seen in Table 8. An abnormally large exciton absorption remains at 10 ps for the reference, which is reflected in the fitting parameters. After 100 ps, no significant changes in the spectra are observed. At 500 ps there may be a slight increase in the polaron band at 660 nm, but not conclusive. The fast component of the GSB recovery is very fast the slow component is similar to those obtain for the octyl-$AgSiO_2$ doped systems. The exciton decay times are slightly longer for the Thio-NP as compared to the Octyl-NP, which is beneficial in terms of migration to the interface. A 12% enhancement of the averaged *PCE* and 13% for the champion devices was realized, for the Thio-$AgSiO_2$ doped devices as compared to the P3HT: PCBM control.

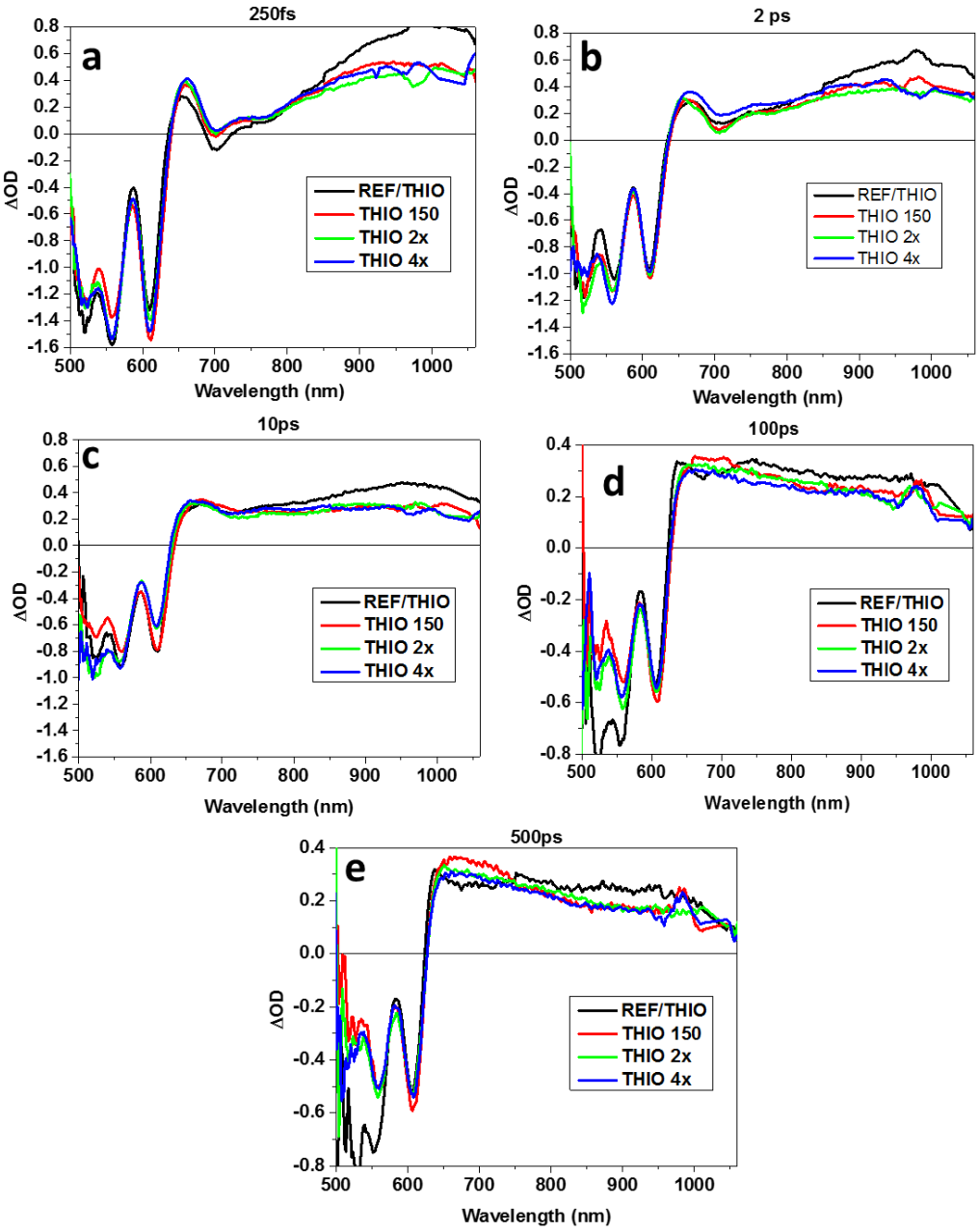

Figure 5.9. PIA spectra of Thio-$AgSiO_2$ - doped PSCs. Spectral snapshots at 250 fs, 2 ps, 10 ps, 100 ps, and 500 ps. Pumped at 490 nm.

Table 8 . Summary of fitted decay times obtain from the Thio-$AgSiO_2$-doped PSCs. Fitted with a bi-exponential decay equation $y = A1*e^{(-x/t1)} + A2*e^{(-x/t2)} + y0$.

610 nm				
Device	**REF**	**Thio-150**	**Thio-300**	**Thio-600**
t1 (ps)	**1.11 ± 0.15**	0.589 ± 0.07	0.742 ± 0.11	0.56 ± 0.05
t2 (ps)	**6.65 ± 0.75**	8.98 ± 0.75	9.26 ± 0.65	7.11 ± .45

1050 nm				
Device	**REF**	**Thio-150**	**Thio-300**	**Thio-600**
t1 (ps)	**0.87 ± 0.09**	2.31 ± .26	1.85 ± .184	3.43 ± 0.34
t2 (ps)	**14.5 ± 0.81**	34.73 ± 2.68	26.8 ± 1.66	31.6 ± 3.65

5.2.6 P3HT-$AgSiO_2$ doped PSCs

If nanoparticle doping is disruptive to OPV device morphology it's hypothesized that functionalization with the donor polymer would minimize those effects. Similarly to previous studies, the P3HT-$AgSiO_2$ NP (75 µg/ml) were doped in various concentrations into P3HT:PCBM blends. Table 9 shows a summary of J-V characteristics of P3HT-$AgSiO_2$ NP doped PSCs devices.

Table 9. Summary of J-V characteristics of P3HT-$AgSiO_2$ NP (75 µg/ml) doped PSCs. 40 mg/ml P3HT:PCBM (1:0.7). 8 devices averaged.

Device Name 40mg/ml	**J_{SC} (mA/cm^2)**	**V_{OC} (V)**	***FF* (%)**	***PCE* (%)**
REF	11.6 ± 0.4	0.52 ± 0.01	55.23 ± 1.3	3.4 ± 0.2 (3.6)
P3HT 150	11.3 ± 0.3	0.52 ± 0.01	54.2 ± 2.6	3.2 ± 0.2 (3.5)
P3HT 150	10.8 ± 0.8	0.51 ± 0.01	53.9 ± 2.3	2.9 ± 0.2 (3.1)
P3HT 2x	10.5 ± 0.5	0.51 ± 0.01	52.9 ± 1.7	2.8 ± 0.2 (3.1)
P3HT 2x	11.0 ± 0.5	0.52 ± 0.00	49.2 ± 1.8	2.8 ± 0.2 (3.1)
P3HT 4x	11.0 ± 0.4	0.52 ± 0.01	59.4 ± 0.9	3.4 ± 0.1 (3.5)

All of the abovementioned P3HT-NP samples underperformed as compared to the reference devices. A troubling trend emerges, whereas the best case scenario is they perform equal to the reference. The deficiencies seen in these devices are in no way systematic, both the J_{SC} and *FF* vary samples to sample, seemingly randomly. After determining the nanoparticle concentration was not the complicating factor, the active layer thickness was increased to 180 nm from 150 nm by increasing the solution concentration from 40 to 45 mg/ml. The J-V characteristics of the thicker samples are summarized in Table 10. Again, a slight decline is seen in the *PCE* of all devices studied, where the changes in J_{SC} and *FF* seem to be random in nature as seen previously. Increasing the solution concentration and film thickness had no impact on the incorporation of P3HT-$AgSiO_2$-NP in PSCs.

Table 10. Summary of J-V characteristics of P3HT-AgSiO2 NP (75 µg/ml) doped PSCs. 45 mg/ml (180 nm thickness) P3HT:PCBM (1:0.7). 8 devices averaged.

Device name	J_{SC} (mA/cm^2)	V_{OC} (V)	*FF* (%)	*PCE* (%)
REF2	12.0 ± 0.5	0.54 ± 0.00	53.4 ± 1.5	3.4 ± 0.2 (3.7)
P3HT 25	11.3 ± 0.6	0.52 ± 0.01	54.0 ± 1.8	3.2 ± 0.2 (3.4)
P3HT 50	11.7 ± 0.6	0.53 ± 0.01	54.2 ± 1.5	3.3 ± 0.1 (3.6)
P3HT 100	11.3 ± 0.5	0.51 ± 0.01	49.4 ± 1.3	2.8 ± 0.1 (3.1)
P3HT 150	12.0 ± 0.6	0.49 ± 0.00	56.0 ± 0.8	3.3 ± 0.1 (3.5)
Device name	**J_{SC} (mA/cm^2)**	**V_{OC} (V)**	***FF* (%)**	***PCE* (%)**
REF	12.3 ± 0.6	0.52 ± 0.01	56.3 ± 2.3	3.6 ± 0.3 (3.8)
P3HT 50	12.2 ± 0.8	0.52 ± 0.00	54.9 ± 0.5	3.5 ± 0.2 (3.7)
P3HT100	11.5 ± 0.7	0.51 ± 0.01	56.0 ± 2.5	3.3 ± 0.4 (3.7)
P3HT150	11.7 ± 0.6	0.52 ± 0.00	58.7 ± 1.0	3.5 ± 0.2 (3.8)

Table 11. Summary of J-V characterization of P3HT-$AgSiO_2$ NP doped PSCs. Cast from 30 mg/ml (110 nm thickness) comparison of (1:1) and (1:0.7) ratios.

Device name 30 mg/ml	J_{SC} **(mA/cm^2)**	V_{OC} **(V)**	***FF*** **(%)**	***PCE*** **(%)**
1:0.7 REF	9.3 ± 0.3	0.54 ± 0.01	64.3 ± 0.6	3.2 ± 0.1 (3.3)
1:1 0 REF	9.3 ± 0.5	0.53 ± 0.01	57.5 ± 1.7	2.8 ± 0.2 (3.1)
1:0.7 150 µl P3HT NP	7.9 ± 0.2	0.53 ± 0.01	61.0 ± 0.7	2.5 ± 0.1 (2.6)
1:1 150 µl P3HT NP	8.5 ± 0.1	0.52 ± 0.01	62.5 ± 1.5	2.8 ± 0.1 (2.9)

Comparing rows one and two in Table 11, when moving from the optimal ratio of 1:0.7 to 1:1 a drastic decrease in *FF* and in turn *PCE*. Looking at row three to row four an increase in *FF* and *PCE* is observed. At low PCBM concentrations the P3HT-$AgSiO_2$ NP are detrimental to device performance, yet at high PCBM concentrations the device is improved. This behavior could be indicative of vitrification, a known challenge in fullerene polymer systems.[20-21] Where the P3HT NP ligands are either trapping PCBM molecules isolating them from charge transport networks, or the NP are increasing the miscibility of P3HT and PCBM affecting the nanoscale morphology. For OPV applications there is a fine balance between the miscibility of the donor acceptor material and the formation of micro-scale interconnected domains to maximize charge transfer and extraction. If large crystalline domains are formed the donor acceptor interface is minimized. When vitrification occurs small isolated amorphous regions form resulting in charge trapping and recombination will dominate.

5.2.7 DSC of P3HT:PCBM Composites

In order to determine the effects of nanoparticle doping on the morphology of P3HT:PCBM, differential scanning calorimeter (DSC) was conducted. DSC is used to study the thermal properties of polymeric materials, such as glass transition temperature, cold crystallization temperature, and the melting temperature. Cold crystallization is the crystalline formation from the amorphous fraction when thermal energy is applied and is the basis for thermal annealing benefits. Octyl-$AgSiO_2$ NP, Thio-$AgSiO_2$ NP and P3HT-$AgSiO_2$ NP were doped in neat P3HT films to ensure the crystallization of P3HT is not disrupted by the addition of nanoparticles. The DSC scans of the P3HT nanoparticle composite materials are shown in Figure 5.10. In the first heating scan, no change in the P3HT melting temperature is observed, indicating no change to the morphology due to NP addition. A small shift in the recrystallization temperature from 188 ºC for the neat P3HT, to 185 ºC for the NP composites.

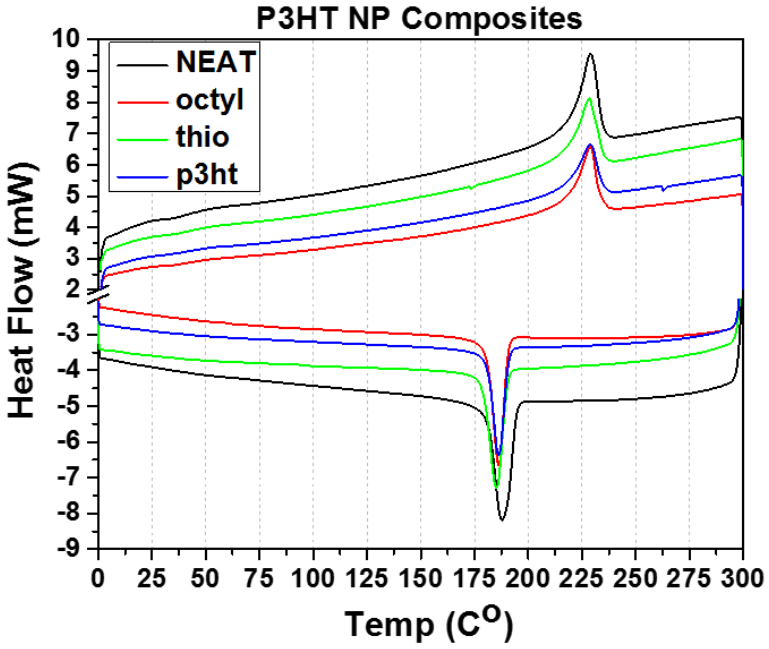

Figure 5.10 DSC scan of P3HT NP composites. First heating and cooling scans. Heating rate 10 ºC/min.

It is clear that NP doping does not impact the crystallization of P3HT, the NP addition could impact the morphology of the P3HT:PCBM. Figure 5.11 shows the first heating and cooling DSC scan of the P3HT:PCBM blend and NP composites with low NP loading. As with the neat P3HT there is a small shift in the recrystallization temperature for the nanoparticle samples. The P3HT:PCBM blend, Octyl-NP, and Thio-NP composites show a melting peak at 224 ºC and the P3HT-NP is 226 ºC, slightly lower than that of neat P3HT (229 ºC) as expected.[22] A small endothermic peak at ≈ 260 ºC is associated to the PCBM. The cold crystallization peak for the P3HT:PCBM and the P3HT-NP sample is ≈ 190 ºC. The Octyl-NP and Thio-NP samples show cold crystallization peak at 175 ºC. This shift to a lower energy for the cold crystallization indicates a more preferential alignment of the chains in the amorphous region induced by the nanoparticles. Figure 5.12 shows the DSC scans where then concentration of nanoparticles was increased by a factor of four. The increase in NP concentration causes two major changes: first, the cold crystallization peak for the octyl-NP and thio-NP is more pronounced and is shifted to an even lower to temperature of 165 ºC. Secondly, the P3HT-NPscan is nearly featureless outside of the melting peak, which indicates that the P3HT-NP act as a vitrifier, which results in a crystalline P3HT regions surrounded by an amorphous material not ideal for charge transport.

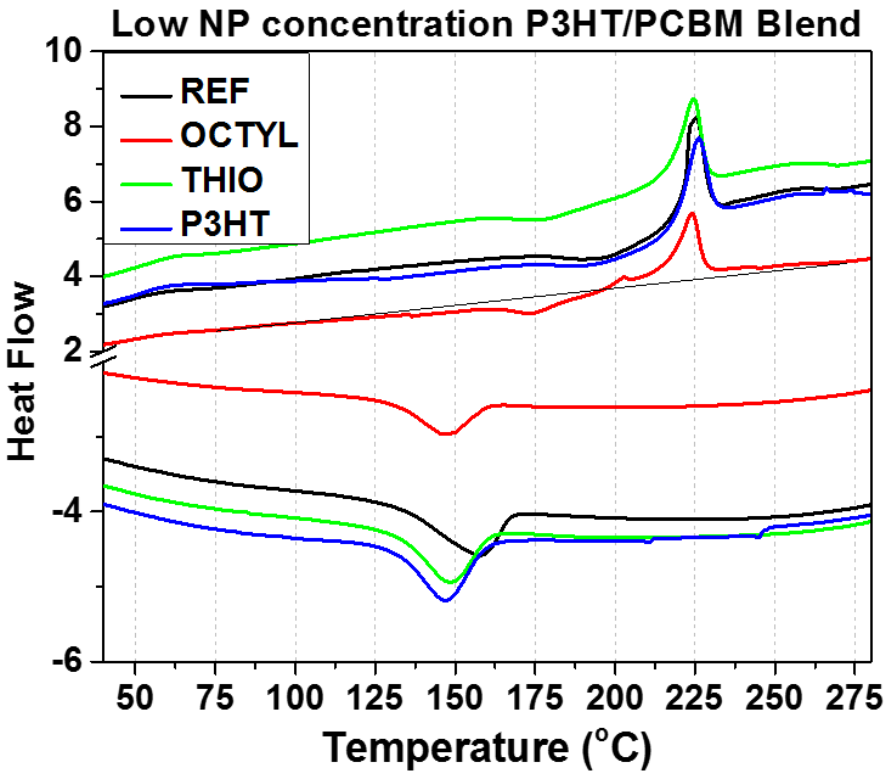

Figure 5.11 DSC scan of P3HT:PCBM:NP composites. (150 µl NP, 150 µl Polymer) First heating and cooling scans. Heating rate 10 °C/min.

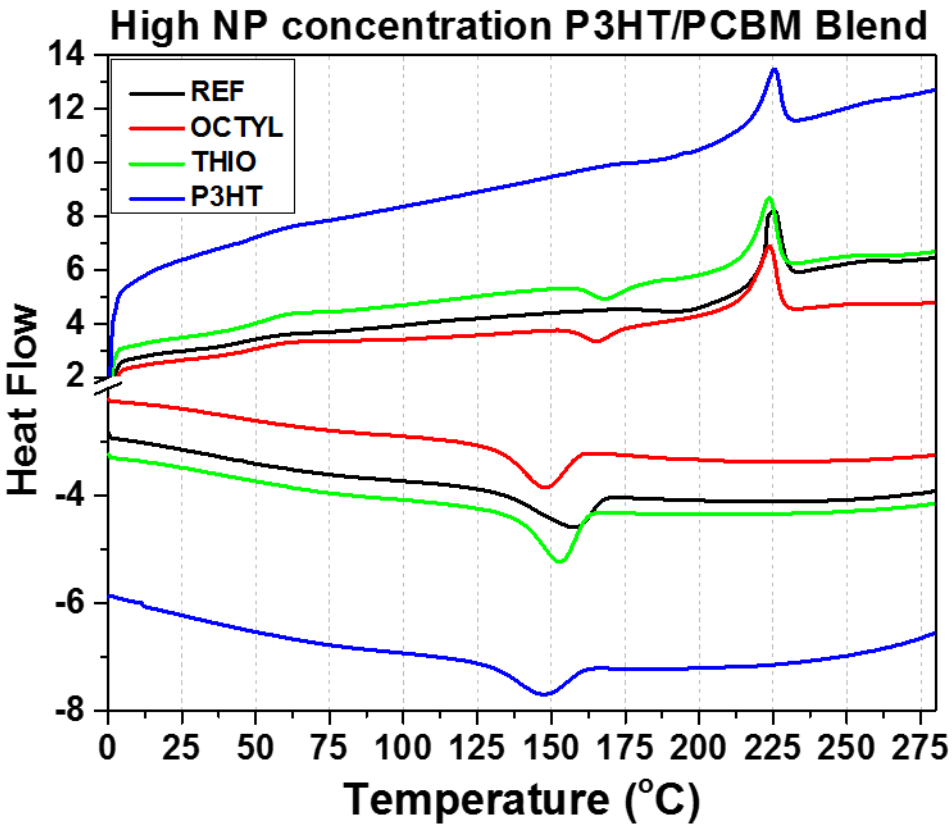

Figure 5.12. DSC scan of P3HT:PCBM:NP composites. (600 µl NP, 150 µl Polymer) First heating and cooling scans. Heating rate 10 °C/min.

5.3 Conclusion

The work in this chapter demonstrates the importance of surface chemistry in plasmonic OPV applications. Silanes containing a P3HT polymer and a single thiophene unit were synthesized and used to functionalize $AgSiO_2$ NP for the incorporation into OPV device. At the optimal concentration, the thio-$AgSiO_2$ NP doped OPVs achieved an averaged PCE of 3.80% compared to the reference averaged PCE of 3.39%, an enhancement of 12%. These enhancements were a result of an increased FF and J_{SC}. Similar

to chapter 4, photo induced absorption measurement, showed no evidence of an increase in absorption coefficient. Additionally, $AgSiO_2$ NP were functionalized with a P3HT containing silane. These particles were also incorporated into P3HT:PCBM OPV device. Attempts to optimize NP concentration, device thickness, and donor acceptor ratio were all unsuccessful in achieving enhancements in OPV performance. DSC measurement of these composite materials show the octyl-$AgSiO_2$ and thio-$AgSiO_2$ NP had a lower and more pronounced cold crystallization temperature indicating improved morphology. As compared to the P3HT-$AgSiO_2$ NPs which caused excessive mixing of the donor-acceptor blend, which leads to poor device morphology. The octyl and thiophene showed nearly identical behavior the P3HT functionalized particles had a negative effect on device performance. This work demonstrates not only that surface functionalization is important it could possibly be used to manipulate device morphology.

5.4 Experimental methods

5.4.1 Synthesis of 2-Allylthiophene

THF for all reactions was dried over sodium benzophenone ketyl

Mg (0.365 g) was loaded in a 2-neck round bottom flask under nitrogen and in an ice bath. A flake of I_2 was added to activate magnesium. 10 ml of THF was added. A few drops 2-bromothoiphene (1.63 g, 10.0 mmol) was added to initiate the reaction. Once reaction begun the remainder was added dropwise. Once the reaction had ceased it was stirred 1hr. Allylbromide (1.21 g, 10 mmol) is added dropwise, and stirred 1 hr. The reaction was quenched with ammonium chloride and extracted with THF and concentrated in vacuo. Crude product was distilled under atmospheric pressure to afford a colorless

liquid (1.09 g, 88%, b.p. 145-150 ºC) ^{1}H NMR (Appendix A) ($CDCl_3$, δ ppm) 3.59 (2H, d), 5.09 (1 H, d), 5.16 (1 H, d), 5.99 (1 H, m), 6.81 (1 H, d), 6.93 (1 H, t), 7.14 (1 H, d)

5.4.2 Synthesis of Silane B

To a round bottom flask containing neat 2-allylthiophene (1.5 g, 12 mmol) and 2 drops Pt^0 catalyst was added triethoxysilane (3.3 ml, 18 mmol). The mixture was stirred for 2 day under nitrogen. The unreacted starting materials remove under reduced pressure. The product was distilled under high vacuum. 1H NMR (Appendix A) ($CDCl_3$, δ ppm) 0.70 (2H, t), 1.23 (9H, t) 1.80 (2H, m), 2.85 (2 H, t), 3.85 (6 H, m), 6.77 (1 H, d), 6.90 (1 H, t), 7.09 (1 H, d).

5.4.3 Synthesis of 2,5-dibromo-3-hexylthiophene

To a round bottom flask at 0°C was added 250 mL of chloroform and 250 mL of glacial acetic acid. To this solution was added 1 (39.19 g, 230 mmol). N-bromo-succinimide (87.21 g, 490 mmol) were added portion-wise with the temperature maintained at 0°C. The reaction was placed under N_2, wrapped in foil, and allowed to come to room temperature and stirred overnight. Water was added to the completed reaction, and the product was extracted with chloroform. The organic phase was collected, washed with 2.0 M KOH, and dried over $MgSO_4$. The solvent was removed under vacuum to afford the crude product which was then purified by column chromatography using heptane as mobile phase. 1H-NMR (Appendix A) (400 MHz; $CDCl_3$): δ 6.78 (s, 1H), 2.51 (t, J = 7.7 Hz, 2H), 1.58-1.50 (m, 2H), 1.36-1.26 (m, 6H), 0.89 (t, J = 6.7 Hz, 3H).

5.4.4 Allyl terminated P3HT

The GRIM method was applied to synthesize the desired polymer in a flamed-dried100-mL round flask bottom under inert atmosphere at room temperature. Initially, 2,5-dibromo-3-hexylthiophene (1.0 g, 3.06 mmol) and freshly distilled THF 10 mL were added into the flask. After mixing for several minutes, tertbutyl magnesium chloride (1.53 ml, 3.06 mmol) and LiCl (130 mg, 3.06 mmol) were then added via a syringe and stirred overnight at room temperature. The reaction mixture was diluted to 50 mL with dried THF, and 1,3-bis(diphenylphosphino)propane nickel-(II) chloride Ni(dppp)Cl2 (15 mg, 0.028 mmol) was added. The polymerization proceeded for 10 min before adding allyl magnesium bromide (1.53 mmol) and then the reaction continued for another 30 min to ensure high end-group functionalization before quenching with methanol. The resulting solid polymer was washed by Soxhlet extraction using ethanol and acetone, and recovered with chloroform. Yield 50%. 1H NMR (Appendix A) ($CDCl_3$, δ (ppm): 6.98 (s, 1H), 6.0 (m, 1H), 5.15 (m, 2 H), 3.52 (d, 2H), 2.8 (t, 2H), 1.7 (q, 2H), 1.3–1.5 (m, 6H), 0.92 (t, 3H).

5.4.5 Synthesis of Silane C

In a flame-dried 50-mL flask, 100 mg of allyl-terminated P3HT (2 equiv.) was mixed with 2 drops Pt^0 catalyst, and 15 mL of THF. The solution mixture was degassed for 15 min to avoid air. Under stirring, 0.3 mL (0.26 g, 100 eq) of triethoxysilane was added dropwise. The mixture was stirred for 30 min at room temperature before its temperature was raised to 55 ºC for 5 hrs. Finally, the polymer was precipitated twice in dry ethanol, filtered under nitrogen, and stored in the glove box to avoid hydrolysis/condensation of the polymer end chain. Yield > 90%. 1H NMR (Appendix A) (400 MHz, $CDCl_3$), δ (ppm): 6.98 (s, 1H), 3.87 (q, 6H), 2.8 (t, 2H), 1.7 (q, 2H), 1.3–1.5 (m, 6H), 1.25 (t, 9H), 0.92 (t, 3H).

5.4.6 Aqueous AgNP Synthesis

Quasi-spherical silver nanoparticles were synthesized via a previously reported method.[23] In short, 12.5 mL ascorbic acid (4.8 mM), 8.825 mL sodium citrate (1 w/w%), were added to 80 mL DIW. The reaction mixture is adjusted to pH 9.5 with 0.1 M citric acid and 0.1 M NaOH. The solution was placed in 30 °C hot bath, and 1 mL aqueous solution of $AgNO_3$ (0.1 M) was injected into the reaction mixture and stirred at 1200 RPM for 15 min. The contents of the reaction flask were then transferred to an oil bath at 100 °C for 30 min without stirring and then placed in ice bath to quench the reaction.

5.4.1 Ag@SiO_2 Nanoparticle Synthesis

The silica coating of Ag nanoparticles was performed using a modified procedure from previous reports.[24,25] 2.0 mL of AgNP, filtered through 0.8 µm Nylon filter to remove large or aggregated nanoparticles, were added to 20 mL of 95/5% ethanol water mixture in a 50 mL centrifuge tube. 600-1200 µL TEOS (10 mM in ethanol) were added and then followed by the addition of 200 µL DMA. The reaction mixture was then shaken with vortex mixer for 2 hrs. Ag@SiO_2 NP were collected using a centrifuge operating at 8000 RPM for 15 min. The resultant Ag@SiO_2 NP were washed 3 times each with ethanol and water, and then dispersed in 2 mL of ethanol.

5.4.2 Non-polar AgNP synthesis

These AgNP were synthesized as previously reported.[26] 50.0 mg of $AgC_2H_3O_2$ is dissolved in 2.0 g oleylamine. This solution is quickly injected to 50.0 ml of refluxing dichlorobenzene (DCB). The mixture is refluxed for 8 hrs, and then cooled to room

temperature. The solvent is then evaporated to 15 ml with either a rotary evaporator or by vacuum distillation. Once volume is reduced to 15 ml and cooled to room temperature. 200 ml of methanol to precipitate the AgNPs. The precipitate is then dissolved in 10 ml of hexane and precipitated with 40 ml of methanol two times. The precipitate is then dried in vacuo, and then dissolved in in DCB.

5.4.3 Functionalization of $AgSiO_2$ NP

The 35.0 ml of $AgSiO_2$ NP are collected via centrifuge and dispersed in 50.0 ml toluene. The concentration of octyltriethoxysilane is adjusted to 3.0 mM and refluxed overnight. The solution is cooled to room temperature and the particles are collected via centrifuged @ 8000 RPM for 12 min and washed with toluene four times. The functionalized NP are dispersed in DCB.

5.4.4 NP characterization

AgNP and $Ag@SiO_2$ NP were drop-casted on carbon coated copper TEM grids (Electron Microscopy Science). TEM images were collected on a JEOL 100CX II TEM with a 100 keV accelerating voltage. UV/VIS measurements were taken with a Shimadzu UV-2401 Dual-Beam UV-Vis Spectrophotometer. AgNPs were drop-cast on KBr powder, the solvent was evaporated, and pelleted for IR spectroscopy taken with Bruker Alpha-T ATR-FTIR Fourier Transform Infrared Spectrometer (FTIR).

5.4.5 Device Fabrication

P3HT: PCBM (1:0.7) dissolved in DCB at 80.0 mg/ml. The solution was heated on a hotplate overnight @ 60 ºC. PEIE was diluted to 0.2 wt/wt % in 2-methoxyethanol and

stirred overnight. ITO patterned substrates were sequentially sonicated in detergent, water, acetone, and IPA for 15 minute cycles. The substrates were then dried under a stream of [27]nitrogen. The substrates were treated with O_2 plasma for 3 min. The PEIE solution was filtered with a 0.2 µm syringe filter onto ITO substrate and spun @ 5000 RPM for 60 sec, and then annealed on a hotplate at 110 ºC for 10 min and cooled to room temperature. The polymer solution is cooled to room temperature and filtered through a 0.2 µm syringe filter. To 150 µl of pre-filtered polymer solution was added 150 µl NP solution of various concentrations. The solution was then sonicated for 10 sec, stirred 5 min, sonicated 10 sec, and then flooded onto an ITO substrates and spun @ 700 RPM for 60 sec. The still wet films were then stored in a petri dish for at least 3 hrs for solvent annealing.

Devices were thermally annealed on a hotplate inside an Ar filled glovebox. The devices were then loaded into vacuum chamber and pumped down to $1x10^{-5}$ mbar. 10 nm MoO_3 and 160 nm Ag are thermally deposited. The J-V characteristics of all photovoltaic devices were evaluated under AM 1.5 G solar illumination (100 mW/cm^2) using a Keithly 4200 semi-conductor parameter analyzer system with a Newport Thermal Oriel 94021 Solar simulator reference with a silicon collar cell.

5.4.6 Transient Absorption Spectroscopy

Differential Transmission spectroscopy measurements were performed using an ultrafast laser system (Pharos Model PH1-20-0200-02-10, Light Conversion) emitting 1030 nm pulses at 100 KHz, with an output power of 20W and pulse duration of ~ 220 fs. Experiments were carried out in an integrated transient absorption/time-resolved photoluminescence commercial setup (Light Conversion Hera). Pump wavelengths in the

spectral range 360–2600 nm were generated by feeding 10W from the laser output to a commercial optical parametric amplifier (Orpheus, Light Conversion, Lithuania), while 2 W are focused onto a sapphire crystal to obtain a single-filament white-light continuum covering the spectral range ~ 490−1050 nm for the probe beam. When higher energy probe light was required, a blue white-light continuum was similarly obtained by using the second harmonic of the laser output instead. The probe beam transmitted through the sample is detected by an imaging spectrograph (Shamrock 193i, Andor Technology Ltd., UK) in combination with a multichannel detector (256 pixels, 200–1100 nm wavelength sensitivity range). Energy densities of 2 μJ/cm^2, with atypical spot diameter of 1.9 mm estimated at the 1/e^2 plane).

5.4.7 DSC Measurements

Solutions prepared as in section 5.4.5, were drop-cast on glass substrate to evaporate. Scraped off substrate and loaded in DSC pan. 1 heating and cooling cycle with heating rate of 10 ºC/min. METTLER TOLEDO Thermal Analysis Premium DSC.

5.5 REFERENCES

1. Gu, Z.; Kanto, T.; Tsuchiya, K.; Shimomura, T.; Ogino, K., Annealing effect on performance and morphology of photovoltaic devices based on poly(3-hexylthiophene)-b-poly(ethylene oxide). *Journal of Polymer Science Part A: Polymer Chemistry* **2011,** *49* (12), 2645-2652.

2. Savikhin, V.; Jagadamma, L. K.; Purvis, L. J.; Robertson, I.; Oosterhout, S. D.; Douglas, C. J.; Samuel, I. D. W.; Toney, M. F., Morphological, Chemical, and Electronic Changes of the Conjugated Polymer PTB7 with Thermal Annealing. *iScience* **2018,** *2*, 182-192.

3. Lan, S.; Yang, H.; Zhang, G.; Wu, X.; Chen, Q.; Chen, L.; Chen, H.; Guo, T., Importance of Solvent Removal Rate on the Morphology and Device Performance of

Organic Photovoltaics with Solvent Annealing. *ACS Applied Materials & Interfaces* **2017,** *9* (24), 20679-20685.

4. Liao, H.-C.; Ho, C.-C.; Chang, C.-Y.; Jao, M.-H.; Darling, S. B.; Su, W.-F., Additives for morphology control in high-efficiency organic solar cells. *Materials Today* **2013,** *16* (9), 326-336.

5. Li, G.; Shrotriya, V.; Huang, J.; Yao, Y.; Moriarty, T.; Emery, K.; Yang, Y., High-efficiency solution processable polymer photovoltaic cells by self-organization of polymer blends. *Nature Materials* **2005,** *4*, 864.

6. Ye, L.; Xiong, Y.; Yao, H.; Gadisa, A.; Zhang, H.; Li, S.; Ghasemi, M.; Balar, N.; Hunt, A.; O'Connor, B. T.; Hou, J.; Ade, H., High Performance Organic Solar Cells Processed by Blade Coating in Air from a Benign Food Additive Solution. *Chemistry of Materials* **2016,** *28* (20), 7451-7458.

7. Hermerschmidt, F.; Papagiorgis, P.; Savva, A.; Christodoulou, C.; Itskos, G.; Choulis, S. A., Inkjet printing processing conditions for bulk-heterojunction solar cells using two high-performing conjugated polymer donors. *Solar Energy Materials and Solar Cells* **2014,** *130*, 474-480.

8. Guilbert, A. A. Y.; Reynolds, L. X.; Bruno, A.; MacLachlan, A.; King, S. P.; Faist, M. A.; Pires, E.; Macdonald, J. E.; Stingelin, N.; Haque, S. A.; Nelson, J., Effect of Multiple Adduct Fullerenes on Microstructure and Phase Behavior of P3HT:Fullerene Blend Films for Organic Solar Cells. *ACS Nano* **2012,** *6* (5), 3868-3875.

9. Müller, C.; Bergqvist, J.; Vandewal, K.; Tvingstedt, K.; Anselmo, A. S.; Magnusson, R.; Alonso, M. I.; Moons, E.; Arwin, H.; Campoy-Quiles, M.; Inganäs, O., Phase behaviour of liquid-crystalline polymer/fullerene organic photovoltaic blends: thermal stability and miscibility. *Journal of Materials Chemistry* **2011,** *21* (29), 10676-10684.

10. Treat, N. D.; Varotto, A.; Takacs, C. J.; Batara, N.; Al-Hashimi, M.; Heeney, M. J.; Heeger, A. J.; Wudl, F.; Hawker, C. J.; Chabinyc, M. L., Polymer-Fullerene Miscibility: A Metric for Screening New Materials for High-Performance Organic Solar Cells. *Journal of the American Chemical Society* **2012,** *134* (38), 15869-15879.

11. Collins, B. A.; Tumbleston, J. R.; Ade, H., Miscibility, Crystallinity, and Phase Development in P3HT/PCBM Solar Cells: Toward an Enlightened Understanding of Device Morphology and Stability. *The Journal of Physical Chemistry Letters* **2011,** *2* (24), 3135-3145.

12. Wong, T. K. S., Effect of embedded nanoparticle surface chemistry on plasmonic organic photovoltaic devices. *Materials for Renewable and Sustainable Energy* **2017,** *6* (1), 4.

13. Liao, H.-C.; Tsao, C.-S.; Lin, T.-H.; Jao, M.-H.; Chuang, C.-M.; Chang, S.-Y.; Huang, Y.-C.; Shao, Y.-T.; Chen, C.-Y.; Su, C.-J.; Jeng, U. S.; Chen, Y.-F.; Su, W.-F.,

Nanoparticle-Tuned Self-Organization of a Bulk Heterojunction Hybrid Solar Cell with Enhanced Performance. *ACS Nano* **2012,** *6* (2), 1657-1666.

14. Zhang, Y.; Wang, C.; Rothberg, L.; Ng, M.-K., Surface-initiated growth of conjugated polymers for functionalization of electronically active nanoporous networks: synthesis, structure and optical properties. *Journal of Materials Chemistry* **2006,** *16* (37), 3721.

15. Yang, W.; Chen, H.; Li, J.; Li, C.; Wu, W.; Jiang, H., Palladium-catalyzed aerobic oxidative double allylic C–H oxygenation of alkenes: a novel and straightforward route to α,β-unsaturated esters. *Chemical Communications* **2015,** *51* (46), 9575-9578.

16. Awada, H.; Medlej, H.; Blanc, S.; Delville, M.-H.; Hiorns, R. C.; Bousquet, A.; Dagron-Lartigau, C.; Billon, L., Versatile functional poly(3-hexylthiophene) for hybrid particles synthesis by the grafting onto technique: Core@shell ZnO nanorods. *Journal of Polymer Science Part A: Polymer Chemistry* **2014,** *52* (1), 30-38.

17. Loewe, R. S.; Khersonsky, S. M.; McCullough, R. D., A Simple Method to Prepare Head-to-Tail Coupled, Regioregular Poly(3-alkylthiophenes) Using Grignard Metathesis. *Advanced Materials* **1999,** *11* (3), 250-253.

18. Rostamzadeh, P.; Mirabedini, S. M.; Esfandeh, M., APS-silane modification of silica nanoparticles: effect of treatment's variables on the grafting content and colloidal stability of the nanoparticles. *Journal of Coatings Technology and Research* **2014,** *11* (4), 651-660.

19. Lu, L.; Luo, Z.; Xu, T.; Yu, L., Cooperative Plasmonic Effect of Ag and Au Nanoparticles on Enhancing Performance of Polymer Solar Cells. *Nano Letters* **2013,** *13* (1), 59-64.

20. Guilbert, A. A. Y.; Zbiri, M.; Dunbar, A. D. F.; Nelson, J., Quantitative Analysis of the Molecular Dynamics of P3HT:PCBM Bulk Heterojunction. *The Journal of Physical Chemistry B* **2017,** *121* (38), 9073-9080.

21. Westacott, P.; Treat, N. D.; Martin, J.; Bannock, J. H.; de Mello, J. C.; Chabinyc, M.; Sieval, A. B.; Michels, J. J.; Stingelin, N., Origin of fullerene-induced vitrification of fullerene:donor polymer photovoltaic blends and its impact on solar cell performance. *Journal of Materials Chemistry A* **2017,** *5* (6), 2689-2700.

22. Zhao, J.; Swinnen, A.; Van Assche, G.; Manca, J.; Vanderzande, D.; Mele, B. V., Phase Diagram of P3HT/PCBM Blends and Its Implication for the Stability of Morphology. *The Journal of Physical Chemistry B* **2009,** *113* (6), 1587-1591.

23. Qin, Y.; Ji, X.; Jing, J.; Liu, H.; Wu, H.; Yang, W., Size control over spherical silver nanoparticles by ascorbic acid reduction. *Colloids and Surfaces A: Physicochemical and Engineering Aspects* **2010,** *372* (1–3), 172-176.

24. Kobayashi, Y.; Katakami, H.; Mine, E.; Nagao, D.; Konno, M.; Liz-Marzán, L. M., Silica coating of silver nanoparticles using a modified Stöber method. *Journal of Colloid and Interface Science* **2005,** *283* (2), 392-396.

25. Liu, S.; Zhang, Z.; Han, M., Gram-Scale Synthesis and Biofunctionalization of Silica-Coated Silver Nanoparticles for Fast Colorimetric DNA Detection. *Analytical Chemistry* **2005,** *77* (8), 2595-2600.

26. Hiramatsu, H.; Osterloh, F. E., A Simple Large-Scale Synthesis of Nearly Monodisperse Gold and Silver Nanoparticles with Adjustable Sizes and with Exchangeable Surfactants. *Chemistry of Materials* **2004,** *16* (13), 2509-2511.

27. Guerrero-Martínez, A.; Pérez-Juste, J.; Liz-Marzán, L. M., Recent Progress on Silica Coating of Nanoparticles and Related Nanomaterials. *Advanced Materials* **2010,** *22* (11), 1182-1195.

CHAPTER 6. SUMMARY AND OUTLOOK

This thesis describes the synthesis, functionalization and application of silica coated silver nanoparticle. Plasmonic metal nanoparticles can be used to concentrate and manipulate light. Due to the oscillations in the conduction electrons under illumination these particles exhibit extremely intense electric fields near their surface. The method developed here represents a significant improvement on the previously reported literature methods.[1-2] The reduction of reaction time and simplification of the reaction conditions proves to be beneficial for quick and reliable production of silica coated silver nanoparticles. The silica shell is useful to passivate the nanoparticle surface to prevent quenching and contamination. Silica can also be easily further functionalized for a variety of applications. The method presented here is expected to become the method of choice going forward.

In chapter 3, the high field strength near the surface of the silica coated silver nanoparticles was exploited to develop a SERS sensing platform. Ragweed pollen particles are an adhesive micro-particle due to their unique morphology, which make them an interesting for development into a SERS substrate. The pollen particles were amine functionalized to render the surface with a positive charge at low pH values. The negative nanoparticle where then electrostatically attached to the pollen surface through simply incubating the pollen in a nanoparticle solution. The nanoparticle pollen composite particles were demonstrated not only broadband SERS activity but also exhibited 2-photon fluorescence. The nanoparticle coating was also shown to double the adhesive properties

of the pollen particles. The result is a biologically derived micro-particle sensor with a large surface area to volume ratio, strong optical signatures with enhanced adhesion properties which can have applications in chemical detection, bio-sensing and security features. The pollen substrate used here was ideal to create an adhesive micro-particle but the method of electrostatic attachment of metal nanoparticles could be extended to other substrate geometries to impart new properties that may be beneficial for a particular SERS application of interest.

Chapters 4 & 5 document the investigation of plasmonic nanoparticle doping in P3HT:PCBM photovoltaic devices. Silica coated silver nanoparticles with differing surface functionalization were doped in the OPV devices to determine what effect, if any, this doping has on the device morphology. The J-V characteristics of these NP doped systems did show enhancement of the power conversion efficiency, which was dependent on the surface functionality of the NP. The NP functionalized with octyl or propyl-thiophene ligands were shown to enhance the power conversion efficiency by 12% as compared to the reference devices which were prepared under the same conditions. The NP particles functionalized with P3HT ligands showed no enhancement to the PCE compared to the reference devices. The hypothesis that these nanoparticles would increase the absorption within the active layer and enhance the device performance was not realized. The linear and transient absorption spectroscopy show no signs of increased absorption. The enhancements to the PCE were a result of an increase in the fill factor and were determined to due to changes in the micro-morphology within the films. The DSC measurements of these composite devices showed a significant differences with respect to the nanoparticle ligands. The P3HT functionalized particles showed characteristics of vitrification of the

binary system which effectively disrupted the bulk heterojunction morphology. The octyl and thiophene functionality showed strong cold crystallization peaks which are indicative of thermally induced crystallization of the P3HT in the amorphous domains which led to increased device performance. Plasmonic optical enhancements were not achieved in this study, but this work is a clear demonstration that more attention needs to be paid to the surface chemistry and morphological effects in plasmonic OPV research. Significant work that has been done in the area of OPV additives to improve device morphology and should be consulted when designing future ligand strategies for plasmonic OPVs. Ideally the NP ligand would optimize the device morphology in concert with plasmonic optical enhancements to achieve optimal device efficiency. Particular attention should be paid to the newly developed ternary blends, which have shown great promise. The application demonstrated here show that with careful selection of the components, plasmonic nanoparticles can be manipulated to achieve a wide range of functional composite materials.

6.1 REFERENCES

1. Kobayashi, Y.; Katakami, H.; Mine, E.; Nagao, D.; Konno, M.; Liz-Marzán, L. M., Silica coating of silver nanoparticles using a modified Stöber method. *Journal of Colloid and Interface Science* **2005,** *283* (2), 392-396.

2. Guerrero-Martínez, A.; Pérez-Juste, J.; Liz-Marzán, L. M., Recent Progress on Silica Coating of Nanoparticles and Related Nanomaterials. *Advanced Materials* **2010,** *22* (11), 1182-1195.

APPENDIX A

A.1 NMR Spectra

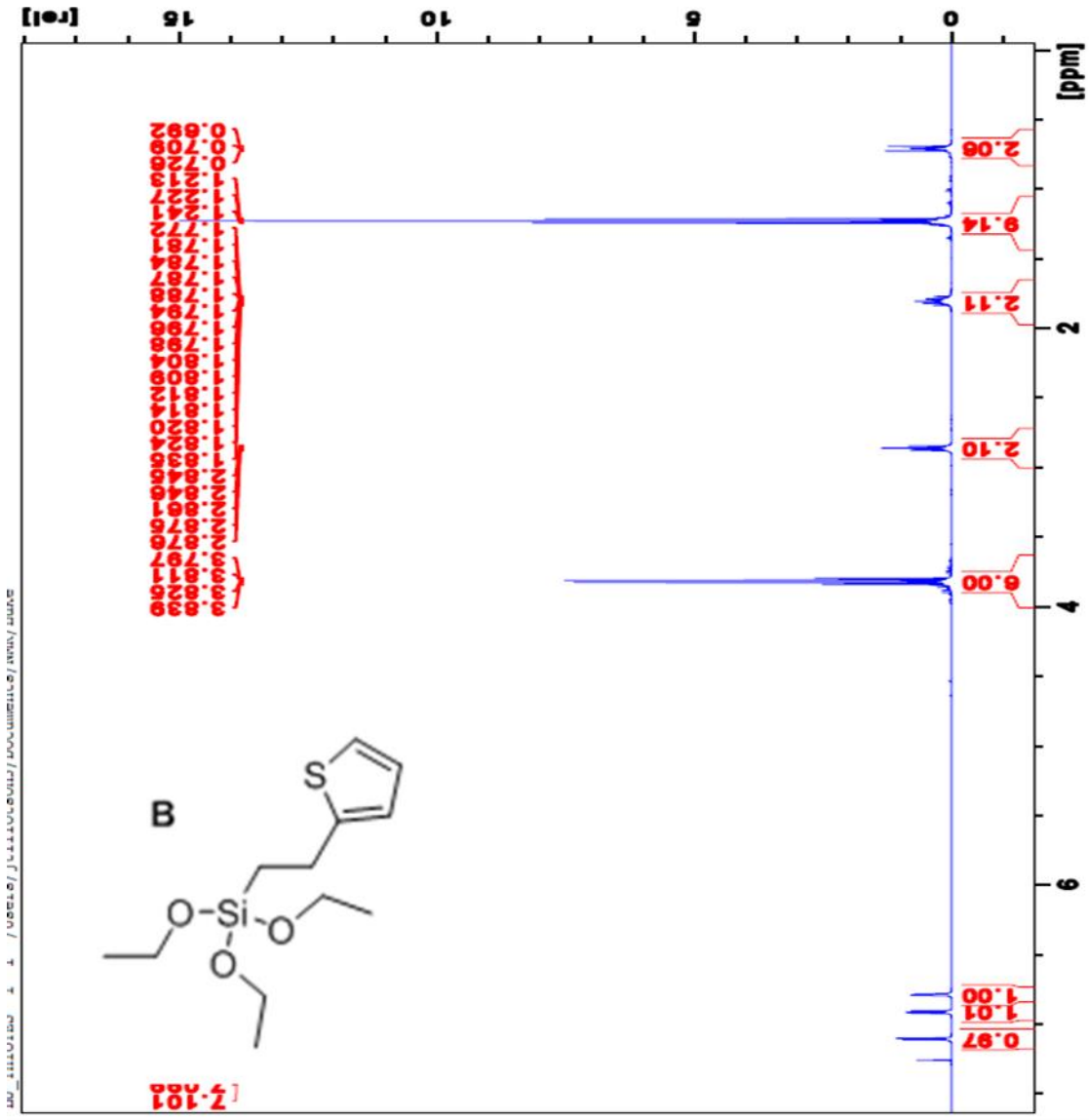

Figure A 1. NMR of 2-(3-triethoxysilyl) propylthiophene.

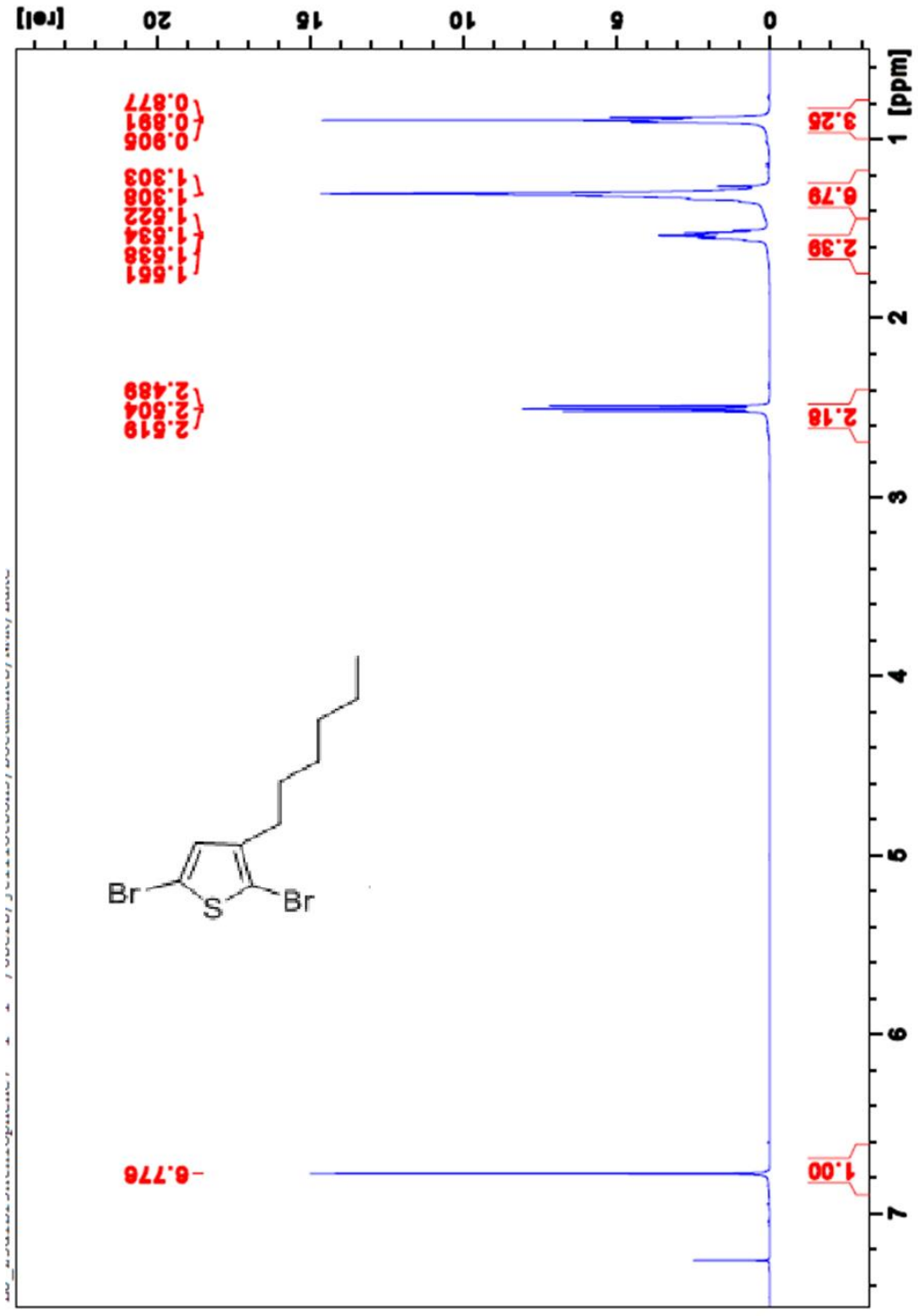

Figure A 2 NMR of 2,5-dibromohexylthiophene.

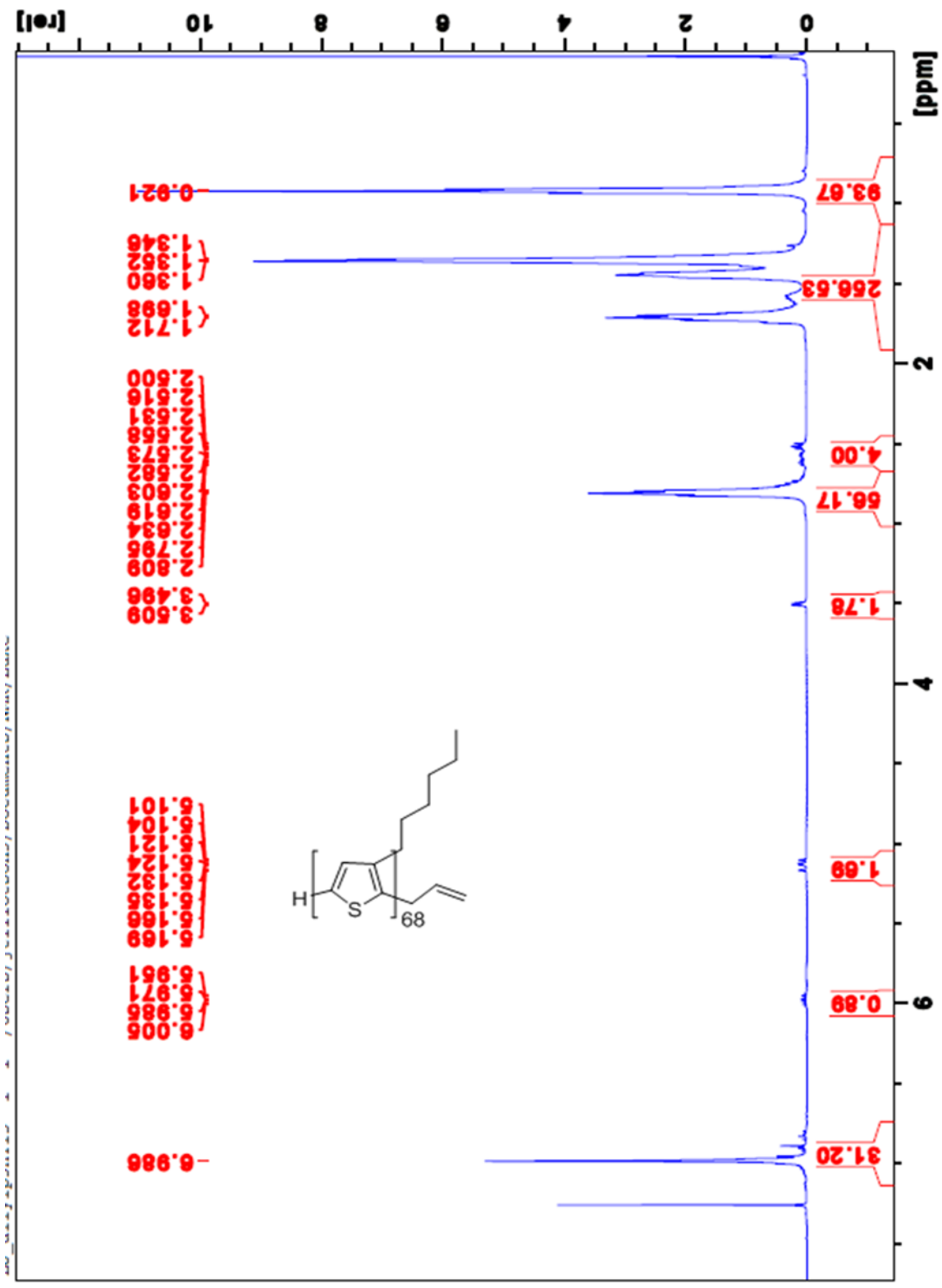

Figure A 3 NMR of allyl-P3HT.

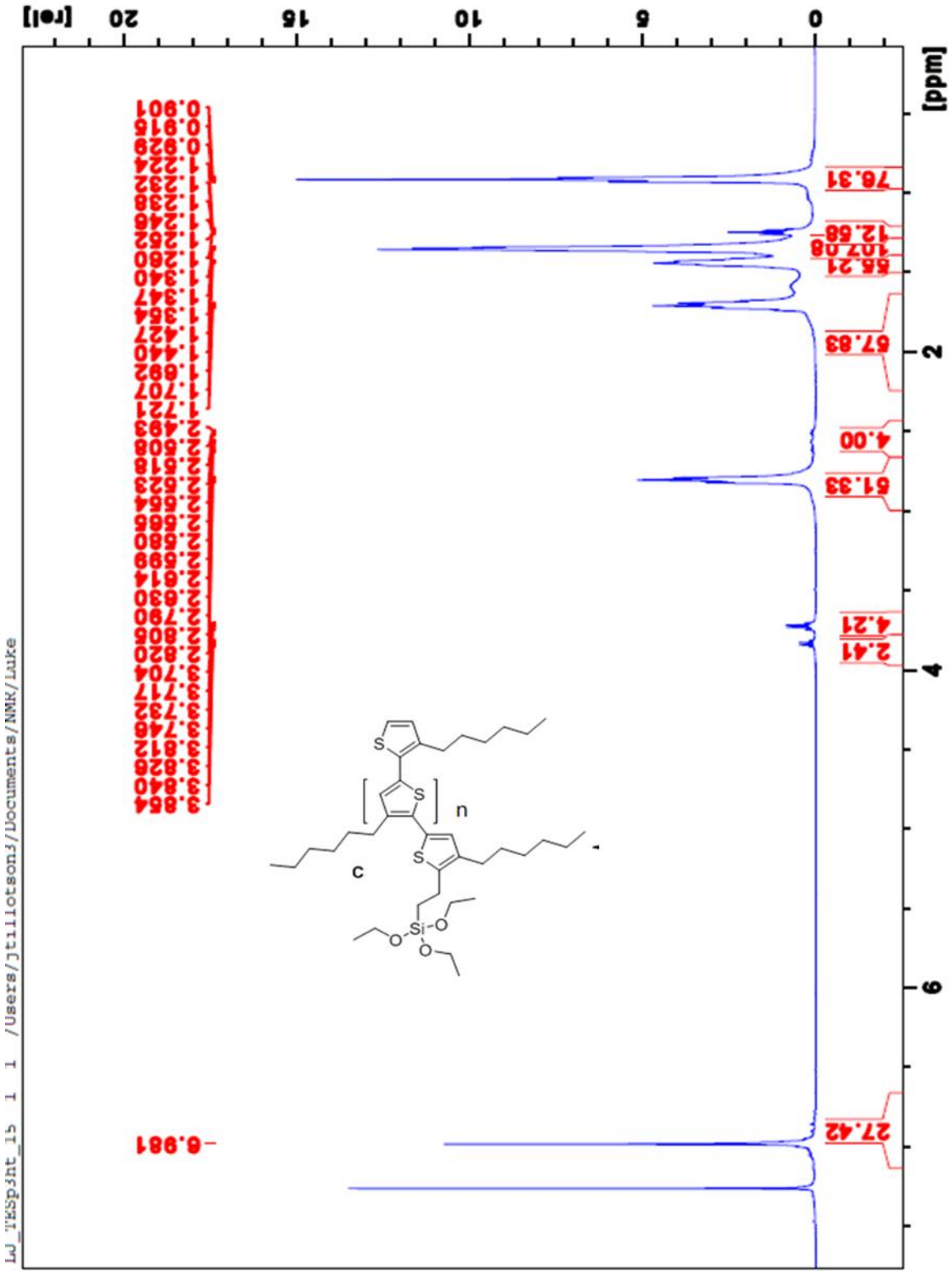

Figure A 4 NMR of P3HT-triethoxysilane.